

**PHOTO-TREATMENT OF PALM OIL MILLS
EFFLUENT (POME) OVER
Cu/TiO₂PHOTOCATALYST**

NG KIM HOONG

**Faculty of Chemical & Natural Resources Engineering
UNIVERSITI MALAYSIA PAHANG**

©NG KIM HOONG (2013)

**PHOTO-TREATMENT OF PALM OIL MILLS
EFFLUENT (POME) OVER Cu/TiO₂
PHOTOCATALYST**

NG KIM HOONG

**Thesis submitted in fulfilment of the requirements
for the award of the degree of
Bachelor of Chemical Engineering**

**Faculty of Chemical & Natural Resources Engineering
UNIVERSITI MALAYSIA PAHANG**

DECEMBER 2013

©NG KIM HOONG (2013)

SUPERVISOR'S DECLARATION

I hereby declare that I have checked this thesis and in my opinion, this thesis is adequate in terms of scope and quality for the award of the degree of Bachelor of Chemical Engineering.

Signature :

Name of main supervisor : DR. CHENG CHIN KUI

Position : SENIOR LECTURER

Date : 18 DECEMBER 2013

STUDENT'S DECLARATION

I declare that this thesis entitled 'Photo-treatment of Palm Oil Mills Effluent (POME) over Cu/TiO₂ Photocatalyst' is the result of my own research except as cited in references. The thesis has not been accepted for any degree and is not concurrently submitted in candidature of any other degree."

Signature :

Name : NG KIM HOONG

Matrix No. : KA10042

Date : 18 DECEMBER 2013

DEDICATION

Special Dedication of This Grateful Feeling to My...

Family and Friends.

For Their Love, Support and Best Wishes.

ACKNOWLEDGEMENT

I wished to express my sincere appreciation to my supervisor, Dr. Cheng Chin Kui for his critics, advices, motivation, friendship and input of ideas, relentless support, guidance and endless encouragement. I also like to express my heartfelt thanks to technical staffs in laboratory Mr. Mohamad Zaki, Mr. Anuar, and Mr. Razak, as helping to make my friends and I stay on the task concerning to the preparation and the thesis progress after all.

I am very thankful to my family and friends for their advice and motivation. Without their endless support and interest, this thesis would not have been same as presented here. I am also indebted to University Malaysia Pahang (UMP) for giving the facilities for my research.

Last but not least, I am grateful to Ministry of Education for the Exploratory Research Grant Scheme RDU120613 for support financially throughout the project.

ABSTRACT

The current work reports the use of titania based photocatalysts for the photo-treatment of palm oil mill effluent collected from Felda Lepar Hilir 3, a local source. Different metal loadings of copper viz. 2wt%, 5wt%, 10wt%, 15wt%, 20wt% and 25wt% were doped onto titania employing wet impregnation method. The synthesized catalysts were subjected to physicochemical characterization. Gas pycnometer density measurements revealed that the actual density of catalysts were lower than theoretical density due to the porous structure as proven by the subsequent liquid N₂ physisorption. In addition, X-ray diffraction pattern showed formation of CuO with crystallite size ranging from 41.8 to 49.1 nm upon calcination. Significantly, liquid N₂ physisorption showed that the BET specific surface area of catalysts prepared decreased with wt% of Cu probably due to pore blockage. Moreover, 5wt% Cu/TiO₂ exhibits the largest pore volume, which is 0.049 cm³/g for both adsorption and desorption volume. In the term of pore size, 20wt% of Cu/TiO₂ has the largest adsorption pore size, which is 23.39 nm while 5wt% of Cu/TiO₂ has the largest desorption pore size, which is 19.83 nm. Based on the UV-irradiated photoreaction results, 20wt% Cu/TiO₂ yielded the highest organic degradability (conversion) among all the synthesized catalysts. Overall, 27.0% conversion was achieved within 1 h of photoreaction. Based on the integral method, it seems that the POME photo-reaction followed the 2nd-order reaction. Moreover, 20 wt% Cu/TiO₂ exhibited the highest specific reaction constant at $2.60 \times 10^{-5} \text{ (ppm.min)}^{-1}$. Besides, an optimum catalyst loading were also discovered in current project. For 20wt% Cu/TiO₂, the optimum catalyst loading is 0.83g/L of POME solution. Finally, a longevity test was conducted and it was found that more than 40% of the organic contaminant was decomposed after 7 h of UV-irradiation. Moreover, CO and CO₂ were detected in the gas products from GC analysis. As conclusion, phototreatment for POME shows positive results in current project and is suitable to replace the existing traditional POME method for better efficiency.

Key words: Copper ; Palm oil mill effluent ; Photocatalysis, Titania-;

ABSTRAK

Projek ini melaporkan tentang penggunaan pemangkin titania untuk teknologi proses penguraian sisa buangan kilang sawit (POME) daripada Felda Lepar Hilir 3. Berbeza peratusan of logam copper seperti 2wt%, 5wt%, 10wt%, 15wt%, 20wt% dan 25wt% telah dicampur ke atas titania melalui wet impregnation method. Pemangkin-pemangkin yang disediakan telah dianalisis melalui pelbagai teknik. Gas pycnometer menyatakan kepadatan pemangkin-pemangkin yang disediakan ini lebih rendah daripada pengiraan disebabkan struktur yang berliang dan ini telah disahkan oleh liquid N₂ physisorption. Selain itu, X-ray diffraction menunjukkan CuO formasi dengan ukuran dari 41.8 sehingga 49.1 nm. Seterusnya, liquid N₂ physisorption menunjukkan kawasan permukaan pemangkin yang disediakan semakin mengurang dengan Cu wt% disebabkan penyumbatan liang. Selain itu, 5wt% Cu/TiO₂ mempunyai isi padu liang yang paling besar iaitu 0.049 cm³/g untuk kedua-dua adsorption dan desorption. Untuk saiz liang, 20wt% Cu/TiO₂ mempunyai adsorption liang saiz yang paling besar iaitu 23.39 nm manakala 5wt% Cu/TiO₂ mempunyai desorption liang saiz yang paling besar iaitu 19.83 nm. Berdasarkan keputusan daripada experiment, 20wt% Cu/TiO₂ paling efektif dalam rawatan POME dan telah mengurangkan organik dalam POME sebanyak 27% dalam 1 jam. Berdasarkan integral method, organik-organik dirawat mengikut reaksi 2nd order. Selain itu, 20wt% Cu/TiO₂ juga menunjukkan kadar reaksi yang paling tinggi, iaitu 2.60×10^{-5} (ppm min)⁻¹. Kandungan pemangkin yang paling optima dalam POME juga dicarikan dalam projek ini, iaitu 0.83g/L. Longevity test telah dijalankan dan 40% organik didapati telah dirawat dalam 7 jam. CO dan CO₂ telah didapati sebagai produk gas daripada experiment ini dengan GC analysis. Akhirnya, teknologi proses penguraian ini menunjukkan keputusan positif dalam prject ini dan sesuai untuk menggantikan cara rawatan yang lama untuk keberkesanan yang lebih baik.

LIST OF EXHIBITION

No	Exhibition	Location
1	Citrex 2013	Universiti Malaysia Pahang, Malaysia
2	Pecipta 2013	KLCC, Malaysia
3	ISCRE 2014	Bangkok, Thailand

TABLE OF CONTENTS

CHAPTER	TITLE	PAGE
	SUPERVISOR'S DECLARATION	II
	STUDENT'S DECLARATION	III
	DEDICATION	IV
	ACKNOWLEDGEMENT	V
	ABSTACT	VI
	ABSTRAK	VII
	LIST OF EXIBITION	VIII
	TABLE OF CONTENTS	IX
	LIST OF FIGURE	XII
	LIST OF TABLE	XV
	LIST OF ABBREVIATIONS	XVI
	LIST OF ABBREVIATIONS	XVII
	LIST OF APPENDICES	XVIII
1	INTRODUCTION	
	1.1 Background	1
	1.2 Problem Statement	3
	1.3 Objective	3
	1.4 Scopes of Study	4
	1.5 Rational and Significance	4
2	LITERATURE REVIEW	
	2.1 Introduction	6
	2.2 Palm Oil Mill Effluent (POME)	7
	2.3 POME Treatments	9
	2.4 Titanium Dioxide (TiO ₂) as Photocatalyst	11
	2.5 Mechanism of Photocatalysis	11
	2.6 Past Photocatalysis Studies	
	2.6.1 Photocatalysis with Different Photocatalysts	13
	2.6.2 The Effects of Different Dopants on TiO ₂ Photocatalyst	20

3	METHODOLOGY	
	3.1 Introduction	27
	3.2 Materials	
	3.2.1 Chemicals	27
	3.2.2 Gases	28
	3.3 Photocatalyst Preparation	28
	3.4 Catalyst Characterization	
	3.4.1 X-ray Fluorescence (XRF)	30
	3.4.2 X-ray Diffraction (XRD)	31
	3.4.3 Gas Pycnometer	33
	3.4.4 Liquid N ₂ Physisorption Analysis	34
	3.4.5 Thermogravimetric Analysis (TGA)	38
	3.5 Photoreaction	
	3.5.1 The Procedures of Photoreaction	39
	3.5.2 Chemical Oxygen Demand (COD)	40
4	RESULTS AND DISCUSSION	
	4.1 Introduction	42
	4.2 Characterization of Catalysts	
	4.2.1 XRF Analysis	42
	4.2.2 XRD Diffraction Pattern	43
	4.2.3 Density of Catalysts	46
	4.2.4 Liquid N ₂ Physisorption	49
	4.2.5 TGA	52
	4.3 Photoreaction	
	4.3.1 Photoreaction with Methylene Blue	54
	4.3.2 Decomposition of POME	56
	4.3.3 Power Law	59
	4.3.4 Optimum Catalyst loading	63
	4.3.5 Longevity Photoreaction	64
	4.4 Gases Products	66
	4.5 Mechanisms of POME decomposition	67

5	CONCLUSIONS AND RECOMMENDATIONS	
	5.1 Conclusions	68
	5.2 Recommendations	70
	REFERENCE	71
	APPENDICES	80

LIST OF FIGURES

FIGURE	TITLE	PAGE
2.1	The mechanisms of photocatalyst (Lasa et al., 2005).	12
2.2	Kinetics curves of conversion of phenol with MnO ₂ as photocatalyst (Zhang et al., 2011).	17
2.3	The graph of removal (%) of organic substances versus photocatalyst concentration (Fenoll et al., 2012).	17
2.4	Concentration of 2,4,6-TCP vs irradiation time under visible-light irradiation ($\lambda > 400$ nm) with the presence of LDH film catalysts with different thickness (Tian et al., 2004).	18
2.5	Photoactivities of four metal oxides in deionized water at various concentration (Lake, 1999).	19
2.6	Azobenzene formation in ethanol on Fe ₂ O ₃ at different aniline concentration under irradiation of UV-light and solar (visible) light (Karunakaran & Senthilvelan, 2006).	20
2.7	Comparison of the decolorization efficiency of Procion red MX-5B by different % wt of Ag/TiO ₂ (Lin & Lee, 2010).	22
2.8	The graph of (C/C ₀) of congo red versus UV irradiation time with various catalyst composition (Farbod & Vala, 2013).	23
2.9	The (C/C ₀) of methyl orange versus visible light irradiation time with different compositions of Fe/TiO ₂ catalyst (Cui et al., 2009).	24
2.10	Photocatalytic discoloration of methylene blue (MB) by TiO ₂ -Cu thin films (Carvalho et al., 2010).	25
2.11	Photocatalytic degradation of Orange II using Cu-Ni, bare TiO ₂ , 10wt% Cu/TiO ₂ calcined at 498 K and 10wt% Ni/TiO ₂ calcined at 498 K photocatalysts and Orange II solution without TiO ₂ (Raiz et al., 2012).	25
2.12	H ₂ production from methanol with different wt% of Cu/TiO ₂ photocatalyst (Wu & Lee, 2004).	26
3.1	A schematic diagram of XRD (A) Collimation (B) Sample (C) Slit (D) Exit Beam Monochromator (E) Detector (X) Source of X-Rays (Source: Cullity, 1978).	33
3.2	Typical N ₂ adsorption-desorption isotherms of mesoporous materials	35

LIST OF FIGURES

FIGURE	TITLE	PAGE
3.3	Typical N ₂ adsorption-desorption isotherms of mesoporous materials.	36
3.4	The setup of photoreaction.	40
4.1	Complete XRD patterns for (a) 2wt% Cu/ TiO ₂ (b) 5wt% Cu/ TiO ₂ (c) 10wt% Cu/ TiO ₂ (d) 15wt% Cu/ TiO ₂ (e) 20wt% Cu/ TiO ₂ (f)25wt% Cu/TiO ₂ .	44
4.2	XRD patterns for catalyst prepared from $2\theta = 35$ to 45° .	45
4.3	The density of 2wt% Cu/ TiO ₂ .	46
4.4	The density value obtained from Equations (4.1) and (4.2).	48
4.5	Comparisons of densities obtained from gas pycnometer and Equations (4.1) and (4.2).	49
4.6	The isotherms for 2wt%, 5wt%, 10wt%, 15wt%, 20wt%, and 25wt% of Cu/TiO ₂ (from top top to bottom).	50
4.7	Derivative weight profile of catalysts prepared	53
4.8	Derivative weight profile of catalysts prepared from T=450 to 550 K.	54
4.9	The calibration curve for methylene blue.	55
4.10	Normalized COD for photoreaction of various wt% of catalysts.	57
4.11	The actual wt% of Cu and conversion of sample for 2wt% to 20wt% of Cu/TiO ₂ .	58
4.12	The conversion and the pore diameter for 20wt% and 25wt% of Cu/TiO ₂ .	59
4.13	Graph for second-order reactions.	61
4.14	Comparison between predicted ($1/C_A$) value and actual ($1/C_A$) value.	61
4.15	Residual plot for decomposition rate of organics in POME.	62
4.16	Graph of conversion versus catalyst loading.	63
4.17	The POME samples for t=0 h (left) and t=7 h (right).	64
4.18	The conversion profile of organics in POME.	65

LIST OF FIGURES

FIGURE	TITLE	PAGE
4.19	Photoreaction setup to collect gases products.	66
4.20	The gas chromatogram of gases produced.	67

LIST OF TABLES

TABLE	TITLE	PAGE
2.1	The general properties of POME (Kamal et al., 2012).	7
2.2	The content of POME (Kamal et al., 2012).	8
2.3	List of POME treatments.	10
2.4	Typical physical and mechanical properties of TiO ₂ (Ceram Research Limited, 2000).	11
2.5	Mechanisms of photocatalysis of TiO ₂ (Turchi & Ollis, 1990).	13
2.6	The summary of past researches on photocatalysis process.	15
2.7	Summary of active metals added to TiO ₂ catalyst.	21
3.1	List of chemicals.	28
3.2	Lists of gases.	28
4.1	Results obtained from XRF test.	42
4.2	Crystalline size of CuO for each catalyst.	45
4.3	The density of 2wt% Cu/ TiO ₂ .	46
4.4	The results obtained from gas pycnometer.	47
4.5	The BET specific surface area for different catalysts	51
4.6	The pore volume for different catalysts.	51
4.7	The pore diameters for different catalysts.	52
4.8	The results obtained from photoreaction of methylene blue..	55
4.9	The results of photoreaction on POME for various catalysts.	56
4.10	The conversions of POME for various catalysts after 1 h of photoreaction.	58
4.11	The specific reaction constants obtained from photoreactions on POME.	62
4.12	Results obtained for longevity photoreaction.	65
4.13	Mechanisms of POME decomposition.	67

LIST OF NOMECLATURES

a	BET effective cross-sectional area
A	apparent absorbance
c	characteristic constant of the adsorbate
C	BET dimensionless constant
C	Concentration
d	Inter plane distance of crystal
D	Crystalline size (Å)
e-	Negative-electron
h+	Positive-hole
k	Rate constant (min ⁻¹)
kSch	Scherrer constant
m	BET mass of solid catalyst
n	Order (interger)
N	Avogrado constant (6.022×10 ²³ mol ⁻¹)
P	BET partial vapor pressure
Pa	BET ambient pressure
Po	BET saturated pressure
ppm	part per million (mg/L)
r	BET correlation coefficient
R	BET gas constant (8.314 E7 ergs/K.mol)
-rA	Photoreaction rate (mg/L.min)
rk	BET Kelvin radius of pore
rp	BET actual pore radius
S	BET specific surface area
T	BET ambient temperature
t	time
Va	BET volume of gas adsorbed at STP
Vads	BET volume of N ₂ adsorbed
Vliq	BET volume of liquid
Vm	BET volume of gas absorbed at STP to monolayer coverage
w	Weight fraction
wt%	Weight percent
X	Conversion
βd	Angular width of half-maximum intensity (degree/°)
γ	BET surface tension of N ₂ (8.85 ergs.cm ² at 77.4 K)
θ	Angle (degree/°)
λ	Wavelength (nm)
ρ	Density

LIST OF ABBREVIATIONS

BET	Brunauer-Emmett-Teller
BJH	Barrett, Joyner and Halenda
BOD	Biochemical oxygen demand
COD	Chemical oxygen demand
DH	Dollimore and Heal
DSC	Differential scanning calorimetry
DTA	Differential thermal analysis
HRT	Hydraulic retention time
LDH	Layered double hydroxide
MB	Methylene blue
POME	Palm oil mills effluent
TGA	Thermogravimetric Analysis
XRD	X-ray Diffraction
XRF	X-ray Fluorescence

LIST OF APPENDICES

APPENDIX	TITLE	PAGE
A	Calculations for Catalyst Preparation	80
B	XRF Results	82
C	XRD Results	87
D	TGA Results	99

CHAPTER 1

INTRODUCTION

1.1 Background

Malaysia has been recognised as one of the largest cooking oil producers in the world (Wu et al., 2010) attributed to its tropical climate and abundance of arable land fit for cash crop cultivation. Nonetheless, the growing success of this industry is often overshadowed by massive industrial discharge from its mill. In the year 2008 alone, at least 44 million tonnes of POME was generated in Malaysia (Wu et al., 2010). In a survey carried out by Sime Darby Plantation (2011), on average, one tonne of fresh fruit bunch processed produces about 0.65 tonne of POME. Palm oil mill effluent (POME) contains high concentration of organic matter. The chemical oxygen demand (COD) of POME is typically in the range of 45,000 to 65,000 mg/l whilst 5-days biochemical oxygen demand (BOD) is averaging 18,000 to 48,000 mg/l (Chin et al., 1996). In addition, oil and grease comprised of more than 2,000 mg/l (Chin et al, 1996). Significantly, the COD : N : P ratio is around 750 : 7.3 : 1 (Chin et al, 1996). A more detailed information of POME will be presented in Section 2.2.

To avoid the water bodies being polluted, POME should undergo treatment before discharged into the rivers. Various treatment and disposal methods have been proposed, investigated and commercialized in the past decades to eliminate or reduce POME pollution. The treatment processes include floatation, membrane technology, various aerobic and anaerobic biodegradation and others (Ahmad et al., 2003). However, an ideal treatment process should be cost-effective and most importantly, the process should not leave any hazardous residues or at least reduces the harmful materials to a safe level.

Significantly, for the past two decades, photocatalysis process has been touted as a promising technology and hence widely investigated for application in treating aqueous organic contents (Puzyn & Mostrag-Szlichtyng, 2012). Photocatalysis applies concept of the acceleration of a photoreaction in the presence of a catalyst as well as the UV or visible light irradiation. It is one of the cleanest technologies for the degradation of waste water and any pollutants or contaminant in POME, since most of the contaminants is organic substrate (Fujishima et al., 2000).

The catalyst that is normally used in photocatalysis process is the titanium dioxide(TiO_2)-based material as it possesses low toxicity, low resistance towards corrosion and also a readily-available semiconductor (Amadelli, 2005). According to Fujishima et al. (2000), TiO_2 is an excellent photocatalyst material for environmental purification. The discussion about catalyst, TiO_2 is incorporated in Section 2.4.

The mechanisms of photocatalysis involve the absorption of light-energy (from UV or visible) by photocatalyst. This in turn will trigger the excitation of electrons across the energy gap into the conduction band. In the presence of water, the electron will change into hydroxyl radical which can decompose organic compounds present in the POME. This forms the basic concept that is to be applied in industrial to treat the pollutant in POME (Linsebigler, 1995). The mechanisms of the catalyst is duly highlighted in Section 2.5.

In POME photo-treatment, catalyst plays an important role in assuring the efficiency. A perfect ratio of active metal doped will enhance the performance of the catalyst. Chapter 3 will discuss the method in preparing the catalyst needed for this research, including pre-treating of raw materials, procedure of preparing and the methods to preserve the catalyst. Besides, Chapter 3 will also discuss on the steps to measure the effectiveness of the catalysts.

The results obtained and related discussion are presented in Chapter 4. The POME concentration was analyzed before and after the photo-treatment process employing the techniques described in Chapter 3.

Finally, summary based on the results as well as the recommendation for future works are presented in the Chapter 5.

1.2 Problem Statement

As aforementioned, Malaysia is one of the biggest palm oil producing country in the world. Hence, large scale generation of waste in the form of POME is unavoidable during the extraction of crude palm oil. The effluent contains high biochemical oxygen demand (BOD) liquid waste and chemical oxygen demand (COD) as rightly pointed out by Ahmad et al. (2003). Direct discharge of untreated POME to rivers will cause serious implications to the existing environment. Therefore, it needs to be treated before being released to the waterway.

Among all the treating methods, photocatalysis is chosen in current study due to its efficiency and green pathway. For photocatalysis, the physicochemical properties of catalyst influence the photocatalytic activity. In particular, the percentage of metal loading in catalyst typically influences the catalyst quality. Titania-based photocatalysts have been prepared with various active metal (copper in this study) loadings. To date, there is paucity of information on photocatalyst treatment towards POME. Therefore, the effectiveness of synthesized catalyst forms the pivotal objective the current work.

1.3 Objective

The objective of this study is to undertake systematic analyses into the effects of various photocatalyst formulations towards physicochemical properties and its POME-photodegradation ability.

1.4 Scopes of Study

To meet the objective of the current work, the following scopes of research have been identified:

1. To prepare TiO₂-based photocatalyst with the following composition of active metal using wet co-impregnation method :
 - i) 2 wt%
 - ii) 5 wt%
 - iii) 10 wt%
 - iv) 15 wt%
 - v) 20 wt%
 - vi) 25 wt%
2. To characterize the physicochemical properties of the photocatalysts via:
 - i) X-ray Fluorescence (XRF)
 - ii) X-ray Diffraction (XRD)
 - iii) Density determination
 - iv) Liquid N₂ Physisorption
 - v) Thermogravimetric Analysis (TGA)
3. To conduct photocatalysis of POME with the catalysts prepared to determine the optimum catalyst
4. To analyse the chemical oxygen demand (COD) of POME before and post photoreaction

1.5 Rational and Significance

POME produced during palm oil production is highly polluting if directly discharge into rivers without treatment. Therefore, a good purification or treatment of POME is essential. With better treatment process, the toxicity of the POME will be less harmful to environment or even diminished. Indirectly, this will help to prevent the environment being compromised, as well as maintaining the ecological balance.

This project aims to help in exploring the application potential of photocatalysis process in POME treatment. This will greatly enhance the effectiveness of photocatalysis, not only in treating POME, but also prospectively for other industrial wastewater. This technology has potential to be commercialized for industrial application due to low cost and significantly low energy consumption.

CHAPTER 2

LITERATURE REVIEW

2.1 Introduction

Palm oil industry is one of the leading agricultural industries in Malaysia with an average crude palm oil production of more than 13 million tonne per year (Nour et al., 2011). However, the massive production of this crude palm oil results in even larger amount of palm oil mill effluent (POME), *circa* 44 million tonnes of POME were generated in the year 2008 alone (Wu et al., 2010). Unfortunately, POME is a highly polluting wastewater with high chemical oxygen demand (COD) and biochemical oxygen demand (BOD). Hence, it causes irreversible distress to the water resources if discharge without treatment (Lam & Lee, 2011).

Significantly, common treatment methods employed in Malaysia are ponding system and aerobic digestion (Tay, 1991; Nour et al., 2013). However, both methods have some disadvantages for POME treatment, *i.e.* long retention time for ponding system and high operating cost for aerobic method. Compounded to these, the land scarcities that came along had invigorate the need for the development of new treating technology such as photocatalysis treatment for POME that was introduced in this thesis.

In this chapter, the previous researches related to this topic is critically reviewed in particular research works that report on the effects of different metal loadings towards photoreaction.

2.2 Palm Oil Mill Effluent (POME)

Oil palm is one of the world's most rapidly expanding equatorial crops. Unfortunately, extracting the palm oil via steam-extraction in any existing palm oil mill generates huge amount of palm oil mill effluent (POME). POME is a brownish colloidal suspension with high organic content and moderate temperature (343 to 353 K) as described by Anon (1995). Generally, this waste is hot and acidic in nature and comprised of oil, plant debris, and nutrients. Large palm oil mills typically produce an average of 0.65 tonnes of raw POME for every tonne of fresh fruit bunches processed (Lim et al., 2012). The general properties of POME are listed in Table 2.1. It shows that the COD value of POME is as high as 15 000 to 100 000 mg/L. High COD values indicate high organic contents within the POME.

Table 2.1 The general properties of POME (Kamal et al., 2012).

Physical & Chemical Properties	Unit	Value
Moisture Content	%	93.4
Ash	%	1.06
Total Solid	g	65 – 80
Soluble Fibre	%	SS 1.12
Non Soluble Fibre	%	TS 3.9
COD	mg/L	15 000-100 000

Table 2.2 lists the contents of POME. It shows that POME consists primarily of solid and volatile organic solids at an average concentration of 40 000 mg/L while oil and grease constitute 4000 mg/L. In addition, there are also some metal contents in POME, *viz.* potassium (2270 mg/L), magnesium (615 mg/L), calcium (439 mg/L) and others. Nonetheless, these inorganic metal contents are considerably lower than the aforementioned organic content.

Due to the hazardous contaminants (cf. Tables 2.1 and 2.2), when POME is discharged into waterways, it can pollute water source that serves as vital drinking water for human and animal populations. More alarmingly, it is also extremely harmful to the aquatic ecology by creating highly acidic environments or causing

eutrophication where excessive algal growth occurs on the surface of the water (Lim et al., 2012).

Table 2.2 The content of POME (Kamal et al., 2012).

Parameter	Average	Metal	Average
pH	4.7	Phosphorous	180
Oil and Grease	4000	Potassium	2270
Total Solids	40500	Magnesium	615
Suspended Solids	18000	Calcium	439
Total Volatile Solids	34000	Baron	7.6
Ammonical Nitrogen	35	Iron	46.5
Total Nitrogen	750	Manganese	2
		Copper	0.89
		Zinc	2.3

*All in mg/l except pH

Moreover, POME also is one of the sources of greenhouse gas (GHG) emissions (Lim et al., 2012). It is well known that POME from the mill site is directly released into open-air holding ponds for remediation and eventually greenhouse gases such as CO₂, CH₄ and H₂S will be released to the air unleashing potentially climate-crippling effects.

To alleviate these catastrophe effects, POME can be utilised for producing value-added chemicals in line with cradle-to-rave concept. According to America Palm Oil Council (2003), POME is an excellent substitute for inorganic fertilizer. Upon treatment, the pH of POME can be raised from 4.0 to *circa* 8.0. Moreover, the BOD is also significantly lower whilst at the same time maintaining the plant nutrients. In terms of fertilizer value, 500 litres of treated POME is equivalent to 1.96 kg of urea (America Palm Oil Council, 2003).

Alternatively, as a potential source of renewable energy, hydrogen (H₂) could be extracted from POME. H₂ is considered as a clean energy as no carbon will be emitted when oxidized (Atif et al., 2005), therefore reducing dependency on the dwindling fossil fuel (Lee, 2012).

2.3 POME Treatments

In Malaysia, most of the palm oil mills use anaerobic digestion for the primary treatment (Tay, 1991). According to Ma et al. (1993), more than 85% the POME producers in Malaysia have adopted the ponding system for POME treatment due to its low capital and operating costs. However, this widely employed method has several disadvantages. One of the disadvantages of ponding system is large land area requirement for treatment process (Nour et al., 2011) as a large pond must be built. Besides, long retention time is also needed for organic contents in the POME to degrade to a safe level (Nour et al., 2011). Usually, the estimated retention time is approximately one to two months. From the environment perspective, emissions of biogas (mixture of CH₄ and CO₂) also poses a major problem to the ozone layer (Nour et al., 2013).

Another common treatment method is aerobic method (cf. Table 2.3). This method is very effective in handling wastewater as it needs shorter retention time (Nour et al., 2013). For instance, Karim and Kamil (1989) found that by using the fungal inoculum, the COD of the POME has recorded more than 95% reduction after 10 to 14 days of fermentation. Besides, Oswal et al. (2002) also found that treating POME with *Yarrowia lipolytica* NCIM 3589 to degrade alkanes contents have provided 95% of reduction in COD within two days. In addition, Vijayaraghavan et al. (2007) disclosed that POME treatment using aerobic oxidation based on an activated sludge process was able to remove COD at higher rate in anaerobically-digested POME as compared to diluted raw POME at hydraulic retention time (HRT) of 60 h. According to Doble and Kumar (2005), one of the primary disadvantages of aerobic method is high energy requirement for aeration, consequently the operating cost will be inflated. Besides, it is also not suitable for land applications due to low inactivation rate of pathogen. Other methods are summarized in Table 2.3, together with their retention time and the corresponding COD reduction percentage.

To overcome these problems, photocatalysis process will be a good choice to replace the aforementioned methods. According to Bahnemann (2004), the advantage of photocatalysis in water purification is the complete decomposition of organics. The effectiveness of POME treatment as the main purpose for the treatment is associated

with organic compound degradation. In terms of energy consumption, ultimately the sun is a continuous and readily available power supply for photocatalysis as the activator needed for this process is visible light or UV radiation (Maria et al., 2011.). Hence, the operating costs will be greatly reduced. Based on these reasons, the photocatalysis process is a potentially valuable technology in POME treatment. Thus, the focus of the current work is to explore the potential of photocatalysis process on POME treatment.

Table 2.3 List of POME treatments.

Treatment process	Retention Time (day)	Reduction in COD (%)	Reference
Anaerobic			
Anaerobic suspended growth processes	35	96	Chin & Wong, 1983
Semi-continuous digester	5.6	75	Cail & Barford, 1985
Anaerobic filter	1	99	Borja & Banks, 1995
Anaerobic fluidized bed reactor	0.25	78	Borja & Banks, 1995
Membrane anaerobic system	3.15	92	Fakhru'l-Razi & Noor, 1999
Semi-commercial closed anaerobic digester	17	>95	Yacob et al., 2006
Completely mixed reactors	50	83	Borja et al., 1995
Tank digester	30	98	Edewor, 1986
Tank digester with certain degree of mixing	30	98	Ugoji, 1997
Modified anaerobic baffled reactor	10	95	Faisal & Unno, 2001
Anaerobic digester	15-16	91	Ma & Ong, 1986
Aerobic			
Pressurized activated sludge process	0.42	98	Ho & Tan, 1988
Aerobic treatment with <i>Yarrowia lipolytica</i>	2	97	Oswal et al., 2002
Activated sludge reactor	2.5	10	Vijayaraghavan et al., 2007
Aerobic treatment with <i>Y. lipolytica</i> þ 0.03 g/L FeCl ₃ þ consortium developed from garden soil	6	99	Oswal et al., 2002
Aerobic treatment with mixed culture	7	>95	Karim & Kamil, 1989
Aerobic treatment with 5% inoculum of <i>Trichoderma viride</i> spores	14	>95	Karim & Kamil, 1989

2.4 Titanium Dioxide (TiO₂) as Photocatalyst

Titanium dioxide, also known as titanium (IV) oxide or titania, is the naturally occurring oxide of titanium with a chemical formula of TiO₂. Its photoactivity property was first discovered by two Japanese scientists in 1972 for the photo-splitting of water (Fujishima & Honda, 1972). Since then, numerous works have evolved in studying the fundamental mechanism and enhancement of the photocatalytic efficiency of TiO₂. In recent years, application of TiO₂ to environmental cleanup has been one of the most active researched areas.

Table 2.4 shows the properties of TiO₂ based on the analyses provided by Ceram Research Limited (2000), an international material-based technology company.

Table 2.4 Typical physical and mechanical properties of TiO₂ (Ceram Research Limited, 2000).

Property	Value
Density	4 g.cm ⁻³
Porosity	0%
Modulus of Rupture	140 MPa
Compressive Strength	680 MPa
Poisson's Ratio	0.27
Fracture Toughness	3.2 MPa.m ^{-1/2}
Shear Modulus	90 GPa
Modulus of Elasticity	230 GPa
Microhardness (HV0.5)	880
Resistivity (298 K)	10 ¹² ohm.cm
Resistivity (973 K)	2.5×10 ⁴ ohm.cm
Dielectric Constant (1MHz)	85
Dissipation factor (1MHz)	5×10 ⁻⁴
Dielectric strength	4 kV.mm ⁻¹
Thermal expansion (RT-273 K)	9 × 10 ⁻⁶
Thermal Conductivity (298 K)	11.7 W.m.K ⁻¹

2.5 Mechanisms of Photocatalysis

According to Carey et al. (1976), photocatalysis process is a new promising alternative method to remove organic pollutants in wastewater. The organic pollutants in the wastewater will be degraded upon contact with the dispersed matrix of

irradiated TiO₂ (Lasa et al., 2005). According to Fujishima et al. (2000), TiO₂ is almost an ideal photocatalyst due to its cost-effective, chemical stability and its highly-oxidizing photogenerated holes. Moreover, the photogenerated electrons are reducing enough to produce superoxide from dioxygen. Indeed, the presence of an emitted photon, availability of catalyst surface area and also a strong oxidizing agent (*i.e.* O₂ or H₂O) are prerequisite for effective photo-reaction.

The energy difference between the valence band and the conduction band is known as the 'Band Gap'. To initiate the photocatalytic reaction, the catalyst (TiO₂) must be exposed to the photon with equal or higher energy than the band gap energy of the photocatalyst for electron excitation. This stage is commonly known as the 'photo-excitation' state. The excess energy absorbed will promote the electron to the conduction band of TiO₂ therefore creating the negative-electron (e⁻) and positive-hole (h⁺) pair.

Figure 2.1 illustrates the mechanism of photocatalysis. The positive-hole of TiO₂ breaks the water molecule apart to form H₂ gas and the hydroxyl (OH•) radical. The negative-electron reacts with O₂ molecule to form super oxide anion (O₂⁻). The organic compounds contained in the water will be degraded and decomposed into carbon dioxide (CO₂) and water (H₂O). This cycle continues in the presence of light.

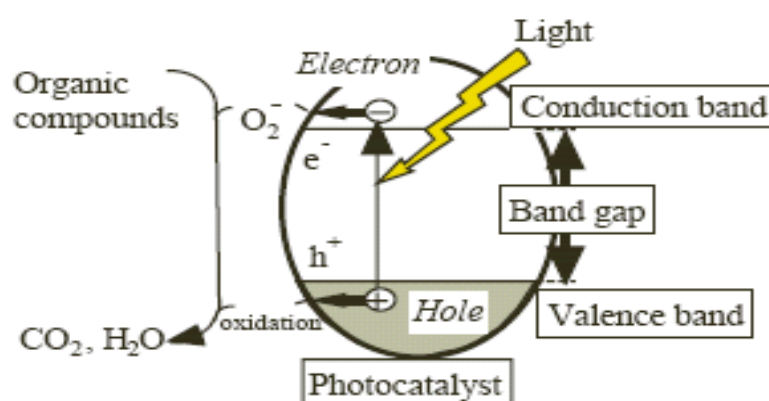


Figure 2.1 The mechanisms of photocatalyst (Lasa et al., 2005).

Table 2.5 shows the simplified mechanisms of photocatalysis of TiO₂ from the research done by Turchi and Ollis (1990).

Table 2.5 Mechanisms of photocatalysis of TiO₂ (Turchi & Ollis, 1990).

Excitation		$\text{TiO}_2 \rightarrow e^- + h^+$
Adsorption	$\text{O}^{2-} + \text{Ti}^{\text{IV}} + \text{H}_2\text{O} \leftrightarrow \text{OH}^- + \text{Ti}^{\text{IV}}\text{-OH}^-$	
	$\text{Ti}^{\text{IV}} + \text{H}_2\text{O} \leftrightarrow \text{Ti}^{\text{IV}}\text{-H}_2\text{O}$	
	$\text{Site} + \text{R}_1 \leftrightarrow \text{R}_{1,\text{ads}}$	
	$\text{OH}\cdot + \text{Ti}^{\text{IV}} \leftrightarrow \text{Ti}^{\text{IV}}\backslash\text{OH}$	
Recombination	$e^- + h^+ \leftrightarrow \text{heat}$	
Trapping	$\text{Ti}^{\text{IV}}\text{-OH}^- + h^+ \leftrightarrow \text{Ti}^{\text{IV}}\backslash\text{OH}$	
	$\text{Ti}^{\text{IV}}\text{-H}_2\text{O} + h^+ \leftrightarrow \text{Ti}^{\text{IV}}\backslash\text{OH} + \text{H}^+$	
	$\text{R}_{1,\text{ads}} + h^+ \leftrightarrow \text{R}_{1,\text{ads}}^+$	
	$\text{Ti}^{\text{IV}} + e^- \leftrightarrow \text{Ti}^{\text{III}}$	
	$\text{Ti}^{\text{III}} + \text{O}_2 \leftrightarrow \text{Ti}^{\text{IV}}\text{-O}_2^-$	
Hydroxyl Attack		
Case I	$\text{Ti}^{\text{IV}}\backslash\text{OH} + \text{R}_{1,\text{ads}} \leftrightarrow \text{Ti}^{\text{IV}} + \text{R}_{2,\text{ads}}$	
Case II	$\text{OH}\cdot + \text{R}_{1,\text{ads}} \leftrightarrow \text{R}_{2,\text{ads}}$	
Case III	$\text{Ti}^{\text{IV}}\backslash\text{OH} + \text{R}_1 \leftrightarrow \text{Ti}^{\text{IV}} + \text{R}_2$	
Case IV	$\text{OH}\cdot + \text{R}_1 \leftrightarrow \text{R}_2$	
Reactions of other radicals		
	$e^- + \text{Ti}^{\text{IV}}\text{-O}_2^- + 2(\text{H}^+) \leftrightarrow \text{Ti}^{\text{IV}}(\text{H}_2\text{O}_2)$	
	$\text{Ti}^{\text{IV}}\text{-O}_2^- + (\text{H}^+) \leftrightarrow \text{Ti}^{\text{IV}}(\text{HO}_2\cdot)$	
	$(\text{H}_2\text{O}_2) + (\text{OH}\cdot) \leftrightarrow (\text{HO}_2\cdot) + (\text{H}_2\text{O})$	

The pair electron-hole formation from the excitation step will lead to the oxidation process in the electron-hole and reduction process by capturing the electron (Lasa et al., 2005). However, there is a possibility of the electron and hole recombination. Efforts are currently underway to study techniques to prevent the recombination in order to increase the efficiency (Lasa et al., 2005).

2.6 Past Photocatalysis Studies

2.6.1 Photocatalysis with Different Photocatalysts

As an environmental application, photocatalysis process is a relatively novel subject with tremendous potential in the future (Al-Rasheed, 2005). A lot of organic matters can be decomposed into inorganic and low-toxicity smaller compound through photocatalysis process (Meng & Juan, 2008). Photocatalysis reaction needs only light,

catalyst as well as water, and the processing cost is lower; hence becoming a new promising method for liquid waste processing. However, different types of catalysts will significantly affect the efficiency. A wide range of semiconductors may be used for photocatalysis, viz. TiO_2 , CdS , SnO_2 , WO_3 , SiO_2 , ZrO_2 , ZnO , Nb_2O_3 , Fe_2O_3 , SrTiO_3 , CeO_2 , Sb_2O_4 , V_2O_5 etc. (de_Richter & Caillol, 2011).

Significantly, voluminous publications of past photocatalysis research works can be found in the open literature. Some of the significantly important past research works are summarized in the Table 2.6.

According to Zhang et al. (2011), manganese (Mn) oxide is very effective in decomposing organic substrate. MnO_2 is a class of active oxides widespread in the environment (Banerjee & Nesbitt, 1999). MnO_2 has been extensively studied as an adsorbent, oxidant, in catalysis and also in rechargeable battery due to its special physicochemical properties, severe defects and nonstoichiometry in the structure (Suib, 2008). This is also echoed by Kwon and co-workers (2009). Besides, Zhang et al. (2011) also found that MnO_2 was very efficient in decomposing phenol when exposed to UV light. Figure 2.2 shows the results obtained from the research, which have indicated an approximately 92% of phenol decomposition over 12 h.

In another independent work, Liao et al. (2004) claimed that TiO_2 is a better photocatalyst candidate due to its high activities, lower prices and possessed chemical and photo-corrosion tolerant properties. Significantly, sulphuric acid-treated TiO_2 showed improvement in degradation ratio of methyl orange, up to 71.9%. In contrast, Fenoll et al. (2012) disagreed that TiO_2 is a good photocatalyst when it came to decomposition of simazine, prometryn, terbutryn, atrazine, terbuthylazine, propachlor, s-metolachlor and alachlor. Fenoll and his fellow co-workers (2012) tested the ability of TiO_2 and ZnO as photocatalyst on decomposing the aforementioned organics under irradiation of UV light. The results obtained are shown in Figure 2.3.

Table 2.6 The summary of past researches on photocatalysis process.

Photocatalyst	Activator	Substrate	Results	Reference
Manganese oxides	UV-light	Phenol	92% of the substrate decomposed.	Zhang et al. ,2011
TiO ₂	UV-light	methyl orange	71.9% of methyl orange degraded.	Liao et al., 2004
Cu–Cr layered double hydroxide (LDH)	Visible light	2,4,6-Trichlorophenol	Less than 10% of 2,4,6-Trichlorophenol present after 200 minutes	Tian et al., 2012
TiO ₂	UV-light	Simazine ,prometryn, terbutryn, atrazine, terbuthylazine, propachlor, s-metolachlor and alachlor	TiO ₂ only able to decompose part of these organic substances effectively.	Fonell et al., 2004
ZnO	UV-light	Simazine ,prometryn, terbutryn, atrazine, terbuthylazine, propachlor, s-metolachlor and alachlor	ZnO able to decompose most of these organic substances effectively.	Fonell et al., 2005
ZnO	UV-light	4-nitrochlorobenzene	98% of 4-nitrochlorobenzene removed over 100 minutes	Yu et al., 2005
CeO ₂	UV-light	Methylene blue	Almost 100% methylene blue is converted over 100 minutes.	Qian et al., 2010
CeO ₂	UV-light	Toluene	Deactivation of catalyst doesn't occurs.	Hernández-Alonso, 2004

Table 2.6 Continue.

Photocatalyst	Activator	Substrate	Results	Reference
Meso-30 wt% Fe ₂ O ₃ /TiO ₂	Visible light	4-chlorophenol	All the 4-chlorophenol decomposed after 180 minutes of the experiment started.	Palanisamy et al., 2013
Fe ₂ O ₃ -TiO ₂ /ACF	Visible light	Methyl orange	[C/C ₀] ratio of methyl orange dropped to 0.32 after exposing under sun for 4 hours.	Zhang & Lei, 2008
Fe ₂ O ₃ and ZrO ₂ /Al ₂ O ₃ (9.1, 31.5, 54.1 wt% respectively)	UV-light	Phenol	93% phenol removed after 120 minutes.	Liu et al., 2012
Fe ₂ O ₃ /SnO ₂	Visible light	Acid blue 62	98.0% acid blue 62 can be degraded in 60 min under illumination of the visible light	Xia et al., 2008
Pd-MoO ₃ /SiO ₂	UV-light	Ethane	The selectivity of ethanal as high as 63.5% compared to 0% without the presence of catalyst.	Wang et al., 2007
CeO ₂ , γ-Fe ₂ O ₃ , TiO ₂ and ZnO	UV-light	Coumarin	TiO ₂ decomposed the most coumarin compared to other photocatalysts.	Bennett & Keller, 2011
Fe ₂ O ₃	UV-light/Visible light	Aniline	Fe ₂ O ₃ is more sensitive to UV-light. More aniline converted under irradiation of UV-light.	Karunakaran & Senthilvelan, 2006

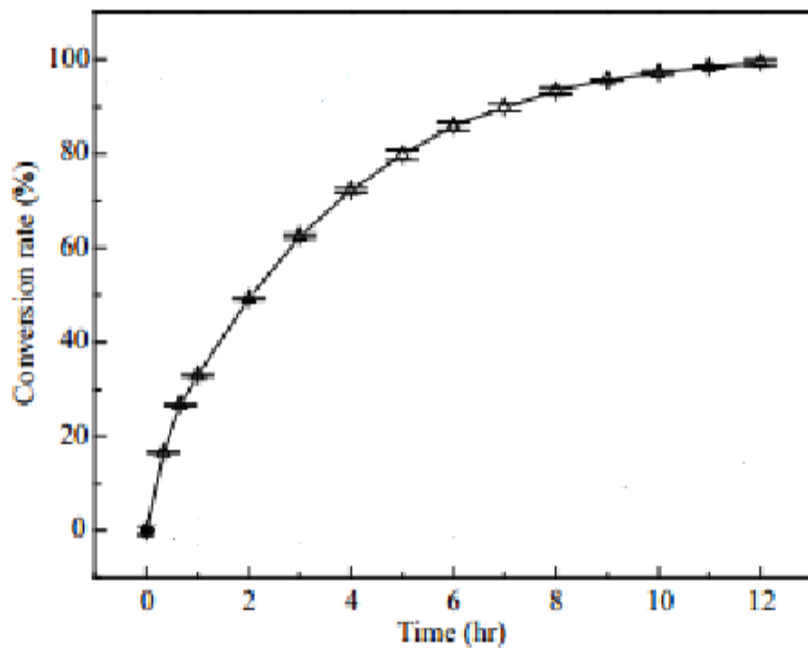


Figure 2.2 Kinetics curves of conversion of phenol with MnO₂ as photocatalyst (Zhang et al., 2011).

Figure 2.3 shows the comparison on the efficiency of ZnO and TiO₂ as photocatalyst on decomposition of various organic substances. Apparently, ZnO performed better in decomposing these organic substances.

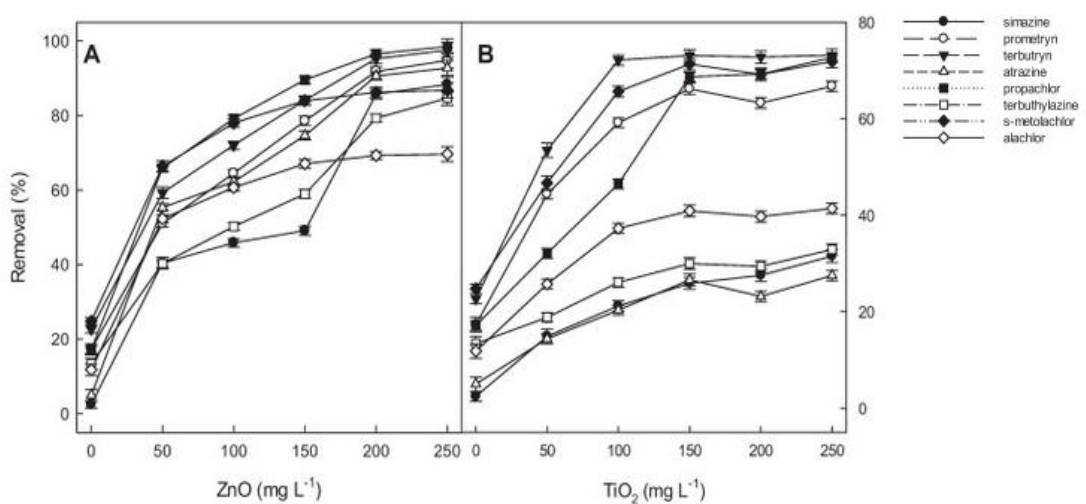


Figure 2.3 The graph of removal (%) of organic substances versus photocatalyst concentration (Fenoll et al., 2012).

Besides the work accomplished by Fenoll et al., Yu et al. (2005) also agreed that ZnO is a good photocatalyst. High purity nano-ZnO was employed to remove 4-

nitrochlorobenzene from the product and the results showed that the removal rate of 4-nitrochlorobenzene can reach 98% when the illumination time was 100 min. It has also increased with the illumination time.

Another research conducted by Tian et al. (2004) presented the potential in Cu–Cr layered double hydroxide (LDH) films to become the photocatalyst. According to Tian et al. (2004), LDH can be used as photocatalysts for the degradation of organic pollutants under visible-light irradiation. Over 90% of 2,4,6-trichlorophenol (2,4,6-TCP) was decomposed by the 16.5 μm LDH films (Tian et al., 2004). Figure 2.4 shows the results of decomposition of 2,4,6-TCP with different thickness of LDH film. The catalyst with thickness of 16.5 μm has effectively decomposed 2,4,6-TCP. More than 90% of the 2,4,6-TCP has photo-decomposed after 200 min.

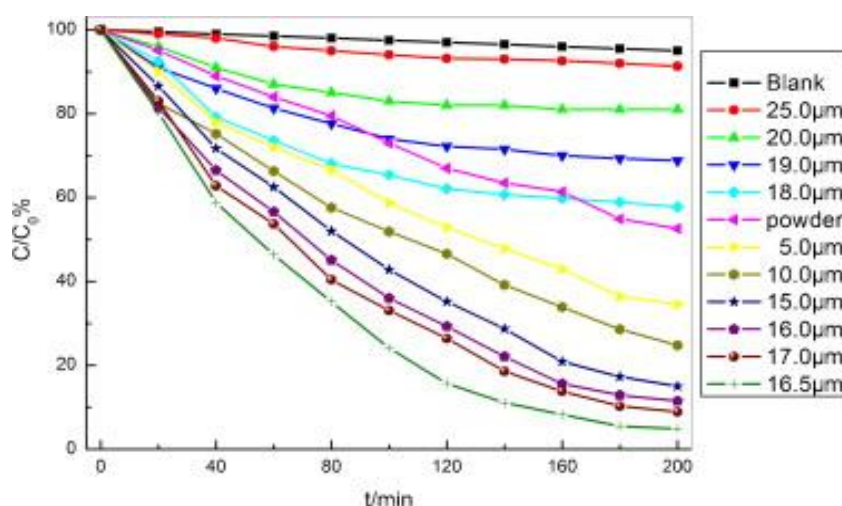


Figure 2.4 Concentration of 2,4,6-TCP vs irradiation time under visible-light irradiation ($\lambda > 400$ nm) with the presence of LDH film catalysts with different thickness (Tian et al., 2004).

Similarly, cerium dioxide (CeO_2) nanoparticles also exhibit good performance in photocatalytic activities (Qian et al., 2012). This can be proven from the degradation of methylene blue under solar energy irradiation. The photocatalytic activity of the CeO_2 was evaluated by photodegradation of methylene blue in aqueous solution under daylight irradiation. Almost all the methylene blue decomposed after 100 min exposure to the daylight (Qian et al., 2012). This was confirmed by Hernández-Alonso (2004) in their subsequent work that used CeO_2 to degrade toluene under the irradiation of UV-light. Their results showed complete removal of toluene. Unlike

TiO₂, CeO₂ would not deactivate during the photocatalytic removal of toluene and other aromatic compounds.

A comparison of photoactivity of CeO₂, γ -Fe₂O₃, TiO₂ and ZnO was carried out by Bennett and Keller (2011). The probe of their research was coumarin. Coumarin is a colorless crystalline organic chemical compound in the benzopyrone chemical class (Lake, 1999). The photoactivities of four nanoscale metal oxides were investigated, at various concentrations. Figure 2.5 shows the results.

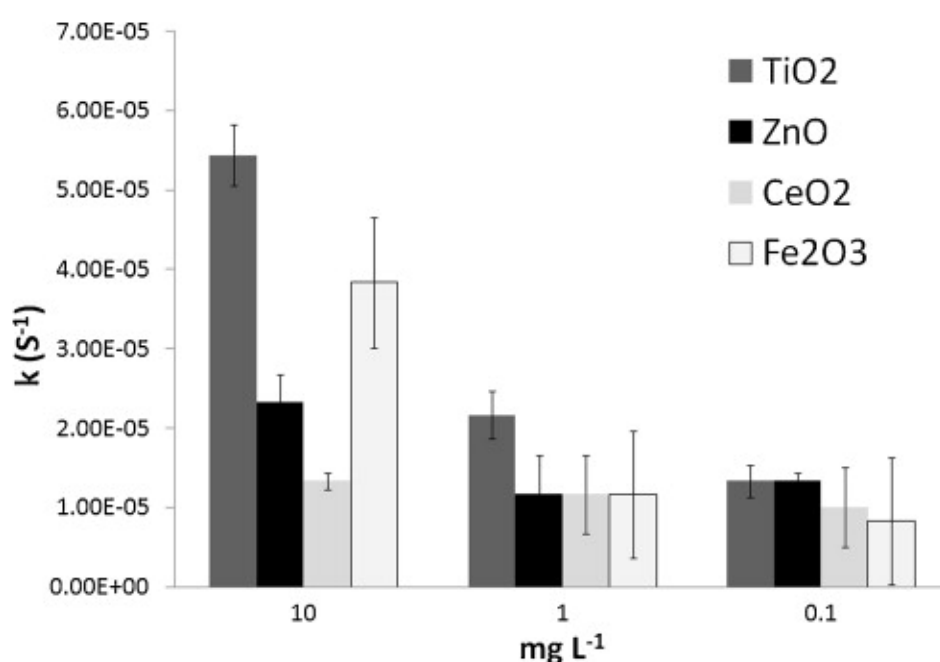


Figure 2.5 Photoactivities of four metal oxides in deionized water at various concentration (Lake, 1999).

Apparently, TiO₂ with catalyst loading of 0.01 g/L was the better photocatalyst in deionized water. It is also most effective photocatalyst for degradation of coumarin.

Fe₂O₃ exhibits sustainable catalytic activity when photocatalyzes the oxidation of aniline in ethanol to azobenzene (Karunakaran & Senthilvelan, 2006). Karunakaran and Senthilvelan (2006) claimed that Fe₂O₃ was able to be activated by both visible light and UV-light. A series of experiments were conducted to find out the effectiveness of UV and visible lights on the formation rate of azobenzene with different initial concentration of aniline in ethanol. The catalyst weight was circa 1.0 g. The results are shown in the Figure 2.6. Basically, both UV-light and visible light

were able to activate the photooxidation process; however Fe_2O_3 was more sensitive to UV-light as more azobenzene was formed under UV irradiation.

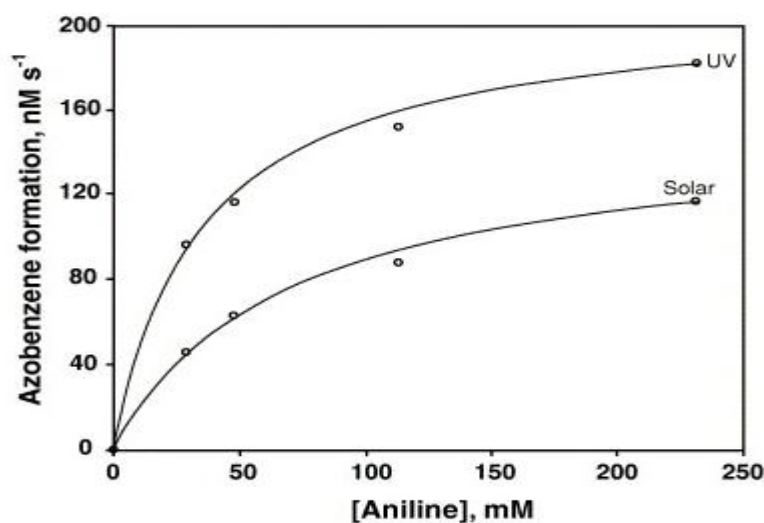


Figure 2.6 Azobenzene formation in ethanol on Fe_2O_3 at different aniline concentration under irradiation of UV-light and solar (visible) light (Karunakaran & Senthilvelan, 2006).

2.6.2 The Effects of Different Dopants on TiO_2 Photocatalyst

This section will discuss on the effect on dopants on the photo-reactivity of TiO_2 photocatalyst. Since TiO_2 is commonly used as photocatalyst, numerous publications on TiO_2 research works can be easily found in the open literature. Some of the more important past research works are summarized in the Table 2.7.

In photocatalysis, the addition of metals to a semiconductor (catalyst) can enhance the yield of a particular product or the rate of the photocatalytic by changing the semiconductor surface properties (Linsebigler et al., 1995). The metal modifies the photocatalytic properties of the semiconductor by changing the distribution of electrons.

Metal content in photocatalyst redistribute the electric charges and causing the formation of double layer. The transfer of mobile charge carriers between the

semiconductor and the metal at surface produces a space charge layer (Linsebigler et al., 1995).

Table 2.7 Summary of active metals added to TiO₂ catalyst.

Active Metal	Substrate	Results	Reference
Ag	Procion red MX-5B	50 wt% Ag/TiO ₂ increased the photo-reactivity significantly.	Lin and Lee,2010.
Gd	Congo red	Gd-doped TiO ₂ generally decolorized congo red in faster rate compare to undoped TiO ₂ .	Farbod & Vala, 2013
Pt	<i>o</i> -cresol	Over 80% of <i>o</i> -cresol oxidized after 400 minutes.	Chen et al., 2007
Fe	Methyl orange	The catalyst is more likely to be activated by visible light after the dopping of Fe.	Cui et al., 2009
Ag	Alcohol	H ₂ production from alcohol increased	Linsebigler et al., 1995
Pt	Alcohol	More effective than Ag/TiO ₂ in H ₂ production from alcohol	Linsebigler et al., 1995
Cu	Methyl blue	Cu effectively enhanced the photoreactivity of TiO ₂	Carvalho et al., 2010
Ni	Orange II	Enhance the photoreactivity of TiO ₂ from 21% to 46.7% of Orange II degradation	Raiz et al, 2012
Cu	Orange II	Enhance the photoreactivity of TiO ₂ from 21% to 54.9% of Orange II degradation	Raiz et al, 2012
Cu	Methanol	The production of H ₂ increased significantly with 1.2wt% Cu doped TiO ₂	Wu & Lee, 2004

The enhancement in reactivity was first observed for the photoconversion of H₂O to H₂ and O₂ by adding the platinum (Pt) in TiO₂ system (Sato & White, 1980). The addition of Pt to the TiO₂ surface enhanced the performance of photocatalytic reactions evolving gas, especially hydrogen (Sato & White, 1980). The electronic modification of the semiconductor surface via metal deposition can also be observed with other noble metals. The addition of silver to the TiO₂ surface increased the

production of H₂ from alcohol (Linsebigler et al., 1995). However, compared to Ag/TiO₂, Pt/TiO₂ would be more effective in H₂ production (Sclafani et al., 1991).

Besides, Ag/TiO₂ was also used in decolorizing Procion red MX-5B. The results showed that Ag/TiO₂ catalyst was able to degrade the MX-5B colour effectively under the irradiation of UV-light while catalyst made up of TiO₂ alone unable to decolorize MX-5B (Lin & Lee, 2010). The results obtained proved that the addition of Ag has significantly improved the performance of the photocatalyst. According to Lin and Lee (2010), when the catalyst was exposed to UV-light, TiO₂ from Ag/TiO₂ demonstrated photocatalytic activity and the Ag carrier further showed an electron-scavenging ability to mitigate the electron-hole pair recombination and eventually improved the photocatalytic efficacy.

Figure 2.7 shows the results obtained from the research work by Lin and Lee (2010) for the decolorization of MX-5B with different compositions of Ag/TiO₂ catalyst. It was further found that 50 wt% Ag/TiO₂ has decomposed 80% of Procion red MX-5B within 120 min.

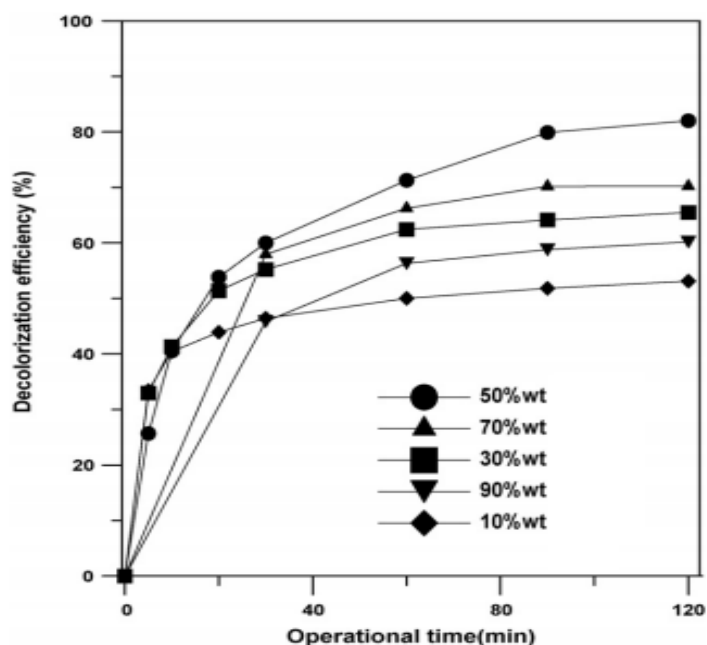


Figure 2.7 Comparison of the decolorization efficiency of Procion red MX-5B by different %wt of Ag/TiO₂ (Lin & Lee, 2010).

The catalyst that was modified by Gadolinium (Gd) doping was also able to enhance the photocatalytic performance. According to Farbod and Vala (2013), the adsorption capacity of the modified catalyst was increased compared to the unmodified one. A set of experiments were conducted with different weight percentage of Gd doped in TiO₂ catalyst to determine the most effective catalyst. The results are illustrated in the Figure 2.8.

The substrate of the experiment was congo red. The (C/C₀) of the congo red has significantly decreased in the presence of catalyst. Based on the graph, Gd/TiO₂ with 1.8wt% of Gd has decomposed most of the congo red. Almost 100% of congo red decomposed after 120 min of UV radiation.

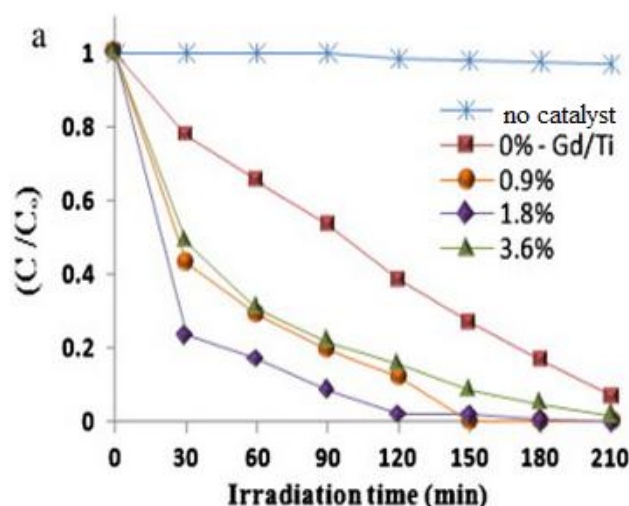


Figure 2.8 The graph of (C/C₀) of congo red versus UV irradiation time with various catalyst composition (Farbod & Vala, 2013).

In the research conducted by Chen et al. (2007), 0.5 wt% Pt was used to modify the TiO₂ catalyst for decomposing the *o*-cresol. The decomposition rate of *o*-cresol under visible light irradiation from a fluorescent lamp was enhanced considerably (Chen et al., 2007) due to the formation of schottky barrier between Pt and TiO₂, therefore preventing the recombination of electric holes and electrons. Compared to undoped TiO₂, the reaction rate of *o*-cresol photodegradation at pH 9 using the 0.50 wt% Pt/TiO₂ was 4.8-fold higher. Ultimately, over 80% of *o*-cresol was degraded after 400 min of photo-reaction.

In addition, iron (Fe) was also another common metal that have been used as the active metal of TiO₂ catalyst. According to Cui et al. (2009), the modification of catalyst with Fe enabled the absorption edge of the TiO₂ based nano-composite red-shifted into the visible region. Under the visible light irradiation, an effective photodegradation of the methyl orange aqueous solution was achieved, revealing the potential applicability of such nano-composite in air and water purifications. The achievements of Fe/TiO₂ catalyst are shown in Figure 2.9.

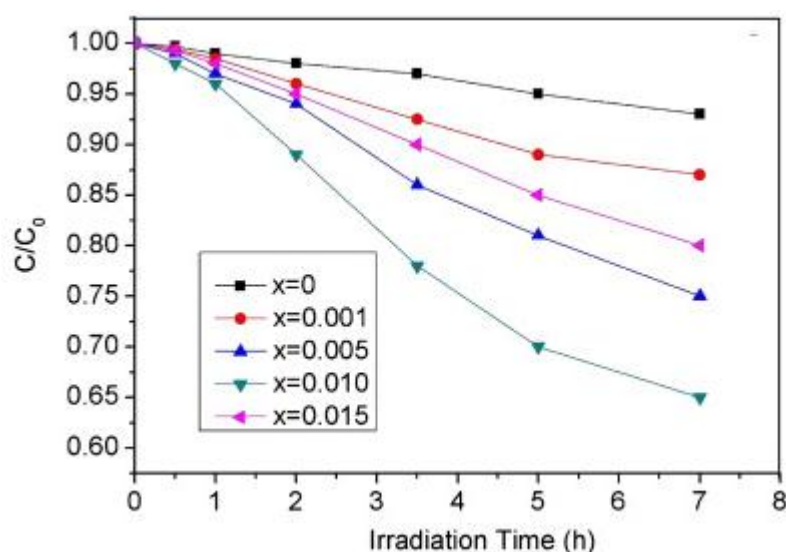


Figure 2.9 The (C/C_0) of methyl orange versus visible light irradiation time with different compositions of Fe/TiO₂ catalyst (Cui et al., 2009).

Another metal dopant that effectively enhance the TiO₂ performance was copper (Cu). Cu was largely utilized as dopant for photocatalyst enhancement due to its relative abundance and low cost (Carvalho et al., 2010). The effects of Cu as dopants of TiO₂ were tested on the decomposition of methyl blue under the irradiation of high-pressure mercury lamp (Carvalho et al., 2010). Prior to the experiment, Cu was annealed to the TiO₂ film at room temperature (RT), 373 K and 673 K. The results obtained are shown in Figure 2.10. Apparently, Cu dopant has greatly increased the photoreactivity of TiO₂. Photocatalyst that was treated at 373 K was able to decompose 90% of the methyl blue within 120 min of reaction in H₂O₂ medium.

Besides, Raiz et al. (2012) also agreed that the doping of Cu into TiO₂ would increase the effectiveness of TiO₂ as photocatalyst. Photoreactivity of bare TiO₂, Ni/TiO₂ and

Cu/TiO₂ is measured by decolorizing Orange II or commonly known as 2-naphthol orange and the results obtained is illustrated in Figure 2.11. From the graph, the doping of Cu or Ni on TiO₂ was able to increase the photoreactivity up to two-folds, in which, Cu dopant enhanced the photoreactivity by increasing the degradation of Orange II from 21% to 54.9% while Ni dopant only increase up to 46.7%. Thus, Cu was a better dopant compared to Ni.

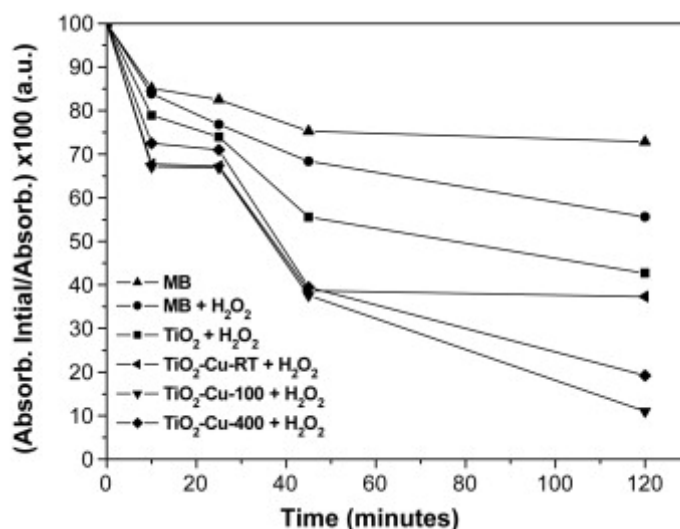


Figure 2.10 Photocatalytic discoloration of methylene blue (MB) by TiO₂-Cu thin films (Carvalho et al., 2010).

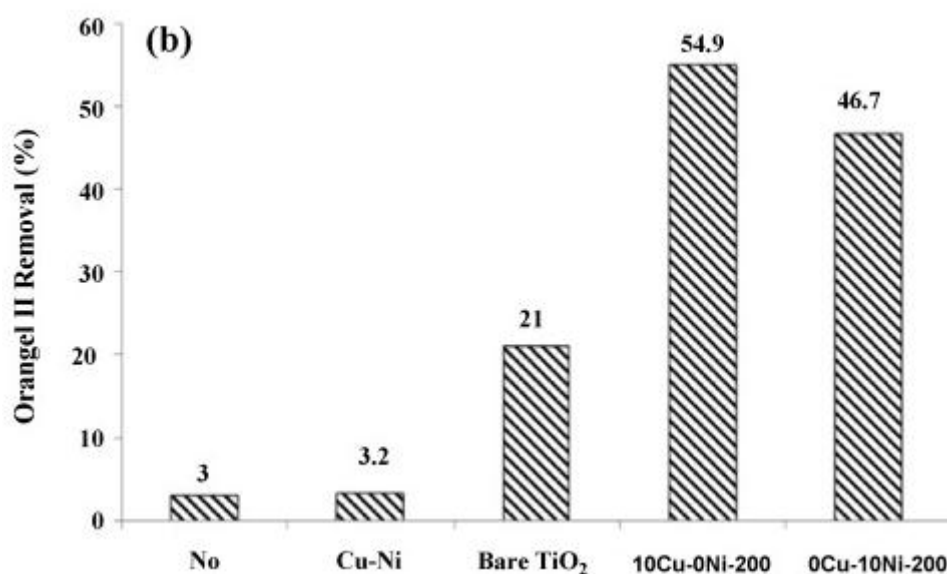


Figure 2.11 Photocatalytic degradation of Orange II using Cu-Ni, bare TiO₂, 10wt% Cu/TiO₂ calcined at 498 K and 10wt% Ni/TiO₂ calcined at 498 K photocatalysts and Orange II solution without TiO₂ (Raiz et al., 2012).

Besides methyl blue and orange II, Cu also led to significant enhancement in photocatalytic activity of TiO₂ for H₂ production from aqueous methanol solution (Wu & Lee, 2004). Different wt% of Cu had been deposited on TiO₂ by incipient-wetness impregnation followed by low-temperature (673 K) calcination process and comparisons of the doped catalysts with bare TiO₂ was made to determine the effectiveness of Cu dopant. After doping, H₂ production from methanol has increased and the optimum wt% of Cu doped was 1.2%. Figure 2.12 shows the results from the research.

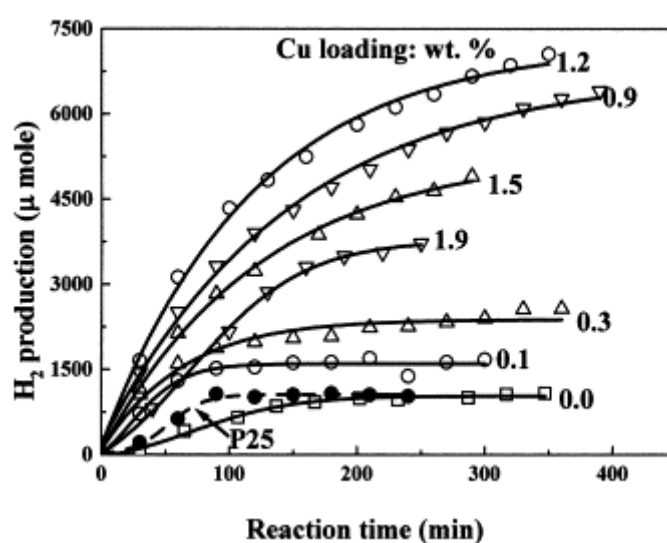


Figure 2.12 H₂ production from methanol with different wt% of Cu/TiO₂ photocatalyst (Wu & Lee, 2004).

CHAPTER 3

METHODOLOGY

3.1 Introduction

In this chapter, details on the photocatalyst, Cu/TiO₂ preparation method will be described followed by the characterization of the photocatalyst. The characterization techniques include X-ray fluorescence (XRF) for elemental studies, X-ray diffraction (XRD) for crystalline structure scanning, density determination by gas pycnometer, liquid nitrogen physisorption for BET surface area, pore volume and pore size distribution measurements, and thermogravimetric analysis (TGA) for catalyst's thermal stability and fraction of volatile components contained. Other than that, the density of the catalysts were also determined by using gas pycnometer machine. Moreover, the theoretical fundamentals and operational procedures of the catalyst characterization instruments will also be discussed in this chapter.

3.2 Materials

3.2.1 Chemicals

The chemicals needed in this study are listed in the Table 3.1. Apart from distilled water, all the chemicals listed in Table 3.1 was procured from the Sigma-Aldrich. The distilled water was readily available from the water purification system available in the laboratory of Universiti Malaysia Pahang (UMP).

Table 3.1 List of chemicals.

Chemical	Purity	Application
Degussa P25 TiO ₂	80% anatase, 20% rutile, BET surface area	catalyst preparation
Cu(NO ₃) ₂ .3H ₂ O	>98%	catalyst preparation
Pottasium bromide – KBr (FTIR grade)	99%	FTIR analysis
Distilled water	-	UMP

3.2.2 Gases

The gases required in the study are listed in Table 3.2. All gases used in this project were supplied by MOX. Table 3.2 also lists the purity of the gases and their application in this study.

Table 3.2 Lists of gases

Gases	Purity	Application
N ₂ /He mixture	N ₂ =30.03%, He=balance	BET analysis
He	> 99.996%	BET analysis
N ₂	> 99.99%	BET analysis

3.3 Photocatalyst Preparation

The physicochemical properties and hence the activity of a photocatalyst strongly depend on the metal content in the catalyst. Since catalyst design are a major part of this work, careful attention was devoted to the preparation of all catalysts including monitoring and controlling related variables especially the concentration of the copper precursor solution as it will decide the loading percentage of the catalyst. Besides the concentration of the precursor, the drying temperature and the calcination temperature of the catalysts are also strictly controlled throughout the catalyst preparation.

Furthermore, the time of stirring after the solutions mixed must be long enough to allow the mixing process accomplished. An analytical balance (4-decimal accuracy) was used for weighing chemicals in all preparations.

The photocatalyst used in the present study is Cu/TiO₂. According to Yoong et al. (2009), the advantage of copper doping onto TiO₂ semiconductor photocatalyst was the enhancement of photocatalytic activity. Hence, the preparation procedure used in this study followed the wet impregnation method described by Yoong et al. (2009). Wet impregnation is a widely used catalyst preparation technique where the precursor material is dissolved in a solvent and mixed with the solid support.

Degussa P25-TiO₂ photocatalyst containing predominantly anatase phase and having a specific surface area of 50 m²/g was sourced from Sigma-Aldrich. The mass ratios of metal dopant precursor, copper nitrate trihydrate, Cu(NO₃)₂.3H₂O (Sigma-Aldrich, >98% purity), and TiO₂ were calculated and weighed accurately and mixed in a 250 ml beaker. Then, 100 ml of deionized water was added to the solid mixture to dissolve the copper precursor, thereafter the obtained slurry was magnetic-stirred for 3 h. Subsequently, the slurry-contained beaker was oven-dried at 393 K for overnight to allow the precursor deposition onto the base material. Finally, the solid formed was air-calcined at 573 K for 30 min. Preparation of different metal loadings also followed the same outlined procedures but different weight ratios of Cu(NO₃)₂.3H₂O and TiO₂.

3.4 Catalyst Characterization

Catalyst characterization provides useful information on the physicochemical properties of the catalyst. The information from various characterization techniques is able to improve the understanding of the physicochemical attributes in relation to the photocatalytic performance. The following subsection describes the fundamental theory and concepts of these characterization techniques used in this work.

3.4.1 X-Ray Fluorescence (XRF)

An X-ray fluorescence (XRF) spectrometer is an x-ray instrument used for routine, relatively non-destructive chemical analyses of rocks, minerals, sediments and fluids. It works on wavelength-dispersive spectroscopic principles that are similar to an electron microprobe (EPMA). The relative ease and low cost of sample preparation, and the stability and ease of use of x-ray spectrometers make this one of the most widely used methods for analysis of major and trace elements in rocks, minerals, and sediment. These applications includes (Fitton, 1997) :

- research in igneous, sedimentary, and metamorphic petrology
- soil surveys
- mining (e.g. measuring the grade of ore)
- cement production
- ceramic and glass manufacturing
- metallurgy (e.g. quality control)
- environmental studies (e.g. analyses of particulate matter on air filters)
- petroleum industry (e.g. sulfur content of crude oils and petroleum products)
- field analysis in geological and environmental studies (using portable, hand-held XRF spectrometers)

Similar with XRD, XRF method depends on fundamental principles that are common to several other instrumental methods involving interactions between electron beams and x-rays with samples. The analysis of major and trace elements in geological materials by x-ray fluorescence is made possible by the behavior of atoms when they interact with radiation. When materials are excited with high-energy, short wavelength radiation (e.g. X-rays), they can become ionized. If the energy of the radiation is sufficient to dislodge a tightly-held inner electron, the atom becomes unstable and an outer electron replaces the missing inner electron. When this happens, energy is released due to the decreased binding energy of the inner electron orbital compared with an outer one. The emitted radiation is of lower energy than the primary incident X-rays and is termed fluorescent radiation. Because the energy of the emitted

photon is characteristic of a transition between specific electron orbitals in a particular element, the resulting fluorescent X-rays can be used to detect the abundances of elements that are present in the sample.

For current work, XRF analysis of the catalysts will be conducted in model of S8 Tiger from Bruker Cooperation by using Quantexpress test method.

3.4.2 X-Ray Diffraction (XRD)

X-ray diffraction (XRD) is a non-destructive analytical technique which is widely used for the identification of structure, crystalline phases, and also sizes of crystallites of natural or synthetic materials. The sample used for this analysis may be powders, solids, films or ribbons and the amount needed is a few milligrams. Nonetheless, greater accuracy is achieved if sample used is up to few grams (Azaroff, 1968). XRD patterns or also known as “fingerprint” varied based on the internal structure of the material and hence the characteristics can be identified.

From this technique, the sample mean crystallite size in the range 3 to 50 nm can be estimated. When crystallite size is smaller than 3 nm, the diffraction lines of X-ray pattern would be diffused or absent. However, if crystallite size is larger than 50 nm, the change in the line shape would not be apparent (Anderson & Pratt, 1985).

In XRD analysis, the sample is ground to powder for the purpose of revealing all possible orientations of the crystal structure to the x-ray beam. When x-ray beam with wavelength, λ is incident on the crystalline structure, diffraction occurs due to interference caused by the nature of the material. The angle at which constructive interference occurred was measured and subsequently the inter planar distances or “d-spacings” between the crystal lattice was identified from Bragg equation (Cullity, 2001). The interplanar spacings depend solely on the dimension of the crystal’s unit cell, on the other hand, the intensities of the diffracted rays function as the placement of the atoms in the unit cell (Klug & Alexander, 1974). Bragg formula is given by Equation (3.1).

$$n\lambda = 2d \sin \varnothing \quad (3.1)$$

where n is the order of reflection (integer), λ is wavelength of x-ray beam (nm), d is inter plane distance of crystal (d-spacing) and \varnothing is angle of incidence (degree).

By assuming the diffraction line shapes are Gaussian, the squares of the contributing width factors are additive. The line width due to particle size broadening can be defined as Equation (3.2).

$$\beta_d^2 = \beta_{obs}^2 + \beta_{inst}^2 \quad (3.2)$$

where β_d is true line width at half maximum intensity (degree), β_{obs} is observed width at half maximum intensity (degree) and β_{inst} is instrumental line width by standard (degree). β_{inst} is obtained from a calibration process using a standard of high quality with a crystalline size greater than 1000 Å. From the results, the mean crystallite size is later calculated by Scherrer equation, Equation (3.3) (Liebhafsky et al., 1972).

$$D = \frac{k_{sch} \lambda}{\beta_d \times \cos \theta} \quad (3.3)$$

where D is the crystalline size (nm), λ is wavelength of X-ray (nm), β_d is angular width at half maximum intensity (radian), θ is Bragg's angle degree and k_{Sch} is Scherrer constant and equals to 0.93 (Warren, 1969).

The schematic of X-ray Diffusion is presented in Figure 3.1. In the current work, XRD measurements were carried out on a Philips X' Pert system using CuK α ($\lambda = 1.542$ Å) at 30 kV and 15 mA. The specimen was initially ground to fine powder (<100 μ m). It was then placed on a glass specimen holder and pressed using a glass slide. Scanning of sample was then performed starting from 20 to 90° at a speed of 1° min⁻¹. Peaks obtained from the analysis were evaluated using The International Centre for Diffraction Data (ICDD) database search match interpretation method to determine the type of phases present.

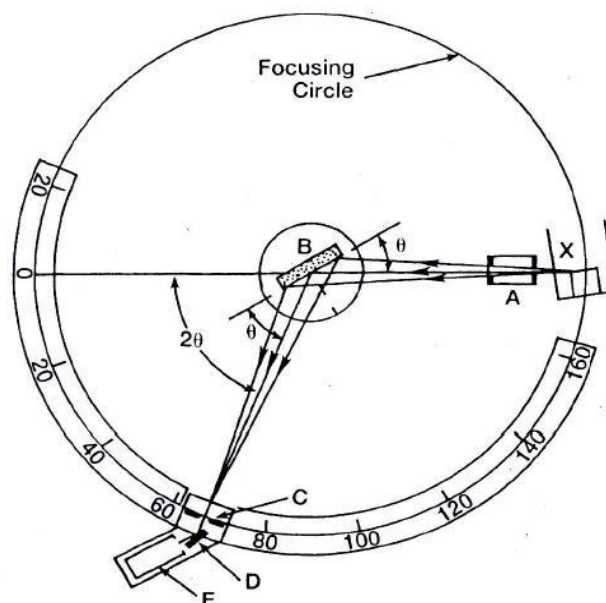


Figure 3.1 A schematic diagram of XRD (A) Collimation (B) Sample (C) Slit (D) Exit Beam Monochromator (E) Detector (X) Source of X-Rays (Cullity, 1978).

3.4.3 Gas Pycnometer

Gas pycnometer is commonly used to measure the density of powders and bulk solids. Gas pycnometer analyse the density, or more accurately the volume of solids by employing some methods of gas displacement and the volume pressure relationship known as Boyle's Law (Shea, 1954).

According to Tamari (2004), gas pycnometry is based on Boyle–Mariotte's law of volume–pressure relationships. This method has been widely used to determine the volume (and thus the density) of rock fragments, soluble powders, light objects and even living beings.

For current study, the density of synthesized catalysts was determined using gas pycnometer of the model AccuPyc II 1340 from Micromeritics. An amount of TiO_2 was weighed and placed into gas pycnometer to analyse the volume, and eventually the density of the catalyst. The test was repeated five times for each catalyst for accuracy.

3.4.4 Liquid N₂ Physisorption Analysis

The most widely used procedure for determination of the surface area of solid materials is the Brunauer-Emmett-Teller (BET) method (Brunauer et al., 1938), which is an extension of the Langmuir's pioneer work (Langmuir, 1916) for monomolecular adsorption. BET equation is derived for multilayer adsorption and based on the relationship between the volume of gas physically adsorbed and the total area of adsorbent, given by:

$$\frac{P}{V(P_s - P)} = \frac{1}{cV_m} + \frac{(c-1)P}{cV_m P_s} \quad (3.4)$$

where P = gas pressure

P_s = saturation pressure of the adsorbate gas

V = volume of gas adsorbed

V_m = volume of gas adsorbed corresponding to monolayer coverage

c = a characteristic constant of the adsorbate

A plot of $P/V(P_s - P)$ against P/P_s provides a linear plot from which V_m and c may be calculated via the slope and intercept respectively. The volume V_m , can then be converted to the number of molecules adsorbed if the cross-sectional area of the adsorbent gas molecule is known. The most commonly used adsorbate is N₂, which has cross-sectional area of 16.2 Å². Therefore, the adsorption of N₂ is carried out at the N₂ boiling point of about 77 K.

The total surface area was determined using multi-point BET method by Thermo Suffer from Thermo Scientific, together with the determination of the pore volume as well as the pore size distribution of the sample.

Porosity of powder and other porous materials may be characterized by liquid N₂ adsorption studies. Two common techniques for describing porosity are the determination of total pore volume and pore size distribution. For the evaluation of the porosity of most solid materials, N₂ at 77 K is the most suitable adsorbate (the material in the adsorbed state). The forces involved in physisorption are the same as

those responsible for the condensations of vapors, which include the London dispersion forces and the short-range intermolecular repulsion (Sing & Rouquerol, 1997).

An understanding of porosity of a solid material can be obtained by the construction of an adsorption isotherm by measuring the quantity of adsorbate on the surface over a wide range of relative pressures at constant temperature (Sing et al., 1985). The adsorption isotherm is obtained point-by-point on the Thermo Suffer by admitting successive known volumes of N_2 to the adsorbent (solid surface) and measuring the equilibrium pressure. Similarly, desorption isotherm can be obtained by measuring the quantities of gas removed from the sample as the relative pressure is lowered.

The total pore volume is derived from the amount of vapour adsorbed at a relative pressure close to unity, by assuming that the pores are then filled with liquid N_2 . If the solid material contains no macropores (pore width > 50 nm), the isotherm will remain nearly horizontal over a range of P/P_o near the unity (Figure 3.2) and the pore volume is well defined.

Nevertheless, the isotherm rises rapidly near P/P_o close to unity for macropores, and in this case it may exhibit an essentially vertical rise (Figure 3.3). Thus, the limiting adsorption may be identified with the total pore volume.

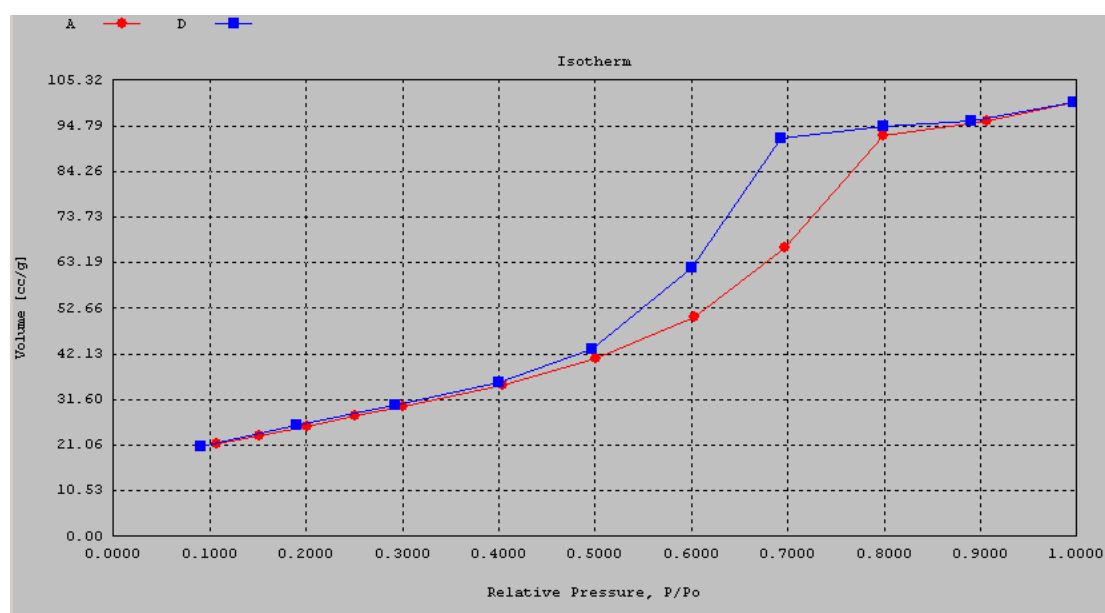


Figure 3.2 Typical N_2 adsorption-desorption isotherms of mesoporous materials.

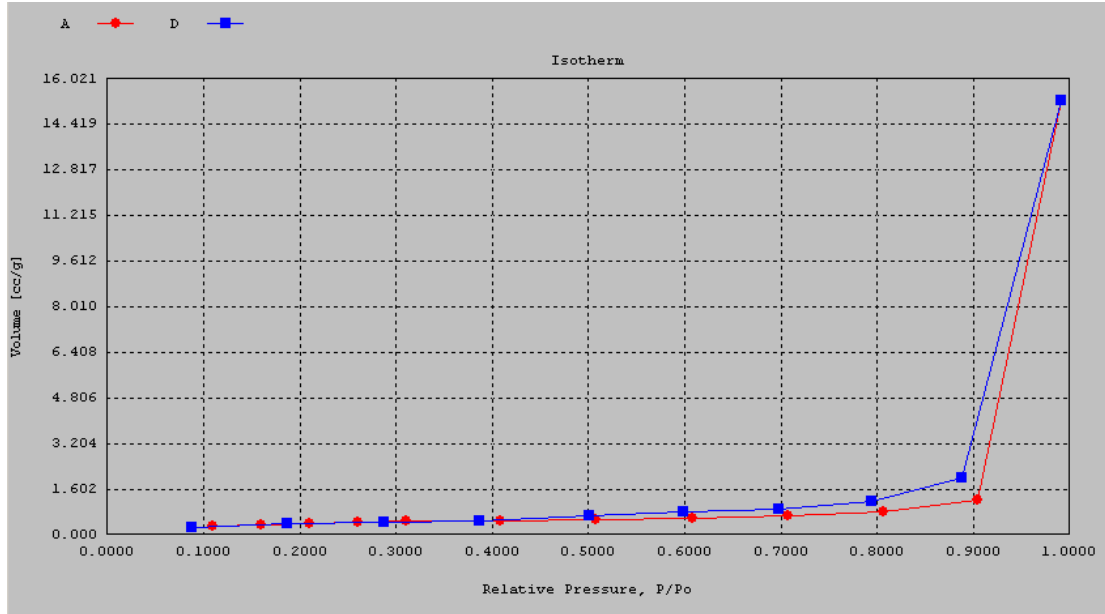


Figure 3.3 Typical N₂ adsorption-desorption isotherms of large macroporous materials.

The volume of nitrogen adsorbed (V_{ads}) can be converted to the volume of liquid N₂ (V_{liq}) contained in the pores using the following equation:

$$V_{liq} = \frac{P_a V_{ads} V_m}{RT} \quad (3.5)$$

where P_a and T are ambient pressure and temperature, and V_m is the molar volume of the liquid N₂ ($34.7 \text{ cm}^3 \cdot \text{mol}^{-1}$) respectively.

Since pores which would not be filled below a P/P_o of unity have a negligible contribution to the total pore volume, the average pore size can be estimated from the pore volume.

The distribution of pore volume with respect to pore size is known as a pore size distribution. It is generally accepted that the desorption isotherm is more appropriate than the adsorption isotherm for evaluating the pore size distribution of a solid material. The desorption branch of the isotherm exhibits a lower relative pressure (P/P_o) resulting in a lower free energy state, and therefore the desorption isotherm is closer to the true thermodynamic stability (Gregg & Sing, 1982). The Autosorb software (AS1 WIN) offers the capability of using either branch of the isotherm for

the pore size distribution calculation. Mesopore size calculations are executed by assuming cylindrical pore geometry using the Kelvin equation (Gregg & Sing, 1982):

$$r_k = \frac{-2\gamma V_m}{RT \ln\left(\frac{P}{P_o}\right)} \quad (3.6)$$

where γ = the surface tension of N₂ at its boiling point (8.85 ergs.cm² at 77 K)

V_m = the molar volume of liquid N₂ (34.7 cm³.mol⁻¹)

R = gas constant (8.314 E7 ergs.K⁻¹.mol⁻¹)

T = N₂ boiling point (77 K)

P/P_o = relative pressure of N₂

r_k = the Kelvin radius of the pore

Using the appropriate constants for N₂, above equation reduces to:

$$r_k \left(\overset{\circ}{\text{A}} \right) = \frac{4.15}{\lg\left(\frac{P}{P_o}\right)} \quad (3.7)$$

The Kelvin radius is the radius of the pore in which condensation happens at P/P_o . However, r_k does not represent the actual pore radius because some adsorption has taken place prior to condensation on the walls of the pore. In addition, during desorption, an adsorbed layer remains on the walls when evaporation occurs.

Therefore, the actual pore radius (r_p) is given by:

$$r_p = r_k + t \quad (3.8)$$

where t is the thickness of the adsorbed layer. The t -value can be estimated by a method proposed by de Boer et al., (1966) as:

$$t(\text{\AA}) = \left[\frac{13.99}{\log\left(\frac{P}{P_0}\right) + 0.034} \right]^{1/2} \quad (3.9)$$

AS1 WIN computes the pore size distribution using the methods proposed by Barrett, Joyner and Halenda (BJH) (Barrette et al., 1951) and by Dollimore and Heal (DH) (Dollimore & Heal, 1964). However, the BJH method is the most widely used for the computation of the pore size distribution (Sing & Rouquerol, 1997). The BJH procedures are based on the emptying of the pores by a step-wise reduction of P/P_0 , and the derived pore size distribution is normally expressed in the graphical form $(\delta V_p / \delta r_p)$ versus r_p or d_p .

3.4.5 Thermogravimetric Analysis (TGA)

Generally, Thermogravimetric analysis (TGA) is an analytical technique used to determine a material's thermal stability and its fraction of volatile components by monitoring the weight change that occurs as a specimen is heated at the constant ramping rate. Normally, the heating process will be carried out in air or in an inert atmosphere such as N_2 , and the weight is recorded as a function of increasing temperature. In addition to weight changes, some instruments also record the temperature difference between the specimen and one or more reference pans (differential thermal analysis, or DTA) or the heat flow into the specimen pan compared to that of the reference pan (differential scanning calorimetry, or DSC). The latter can be used to monitor the energy released or absorbed via chemical reactions during the heating process. In the particular case of carbon nanotubes, the weight change in an air atmosphere is typically a superposition of the weight loss due to oxidation of carbon into gaseous carbon dioxide and the weight gain due to oxidation of residual metal catalyst into solid oxides.

TGA instruments can be divided into two general types: vertical and horizontal balance. Vertical balance instruments have a specimen pan hanging from the balance (TA Instruments, etc) or located above the balance on a sample stem (Netzsch). It is

necessary to calibrate these instruments in order to compensate for buoyancy effects due to the variation in the density of the purge gas with temperature, as well as the type of gas. Vertical balance instruments generally do not have reference pan and are incapable of true DTA or DSC measurements (Netzsch being an exception). Horizontal balance instruments (TA, Perkin Elmer, etc.) normally have two pans (sample and reference) and can perform DTA and DSC measurements. They are considered free from buoyancy effects, but require calibration to compensate for differential thermal expansion of balance arms. One common instrument for general purpose use, the Q500-model thermogravimetry analyzer (TGA), is used as the instruments for current project.

For the current work, TGA runs were performed in an oxidative atmosphere (air) with the ramping rate of 5 K min^{-1} for all the catalysts prepared using Q500-model thermogravimetry analyzer (TGA). The maximum temperature selected was 1173 K. High temperature was employed so that the thermal stability of catalysts can be determined at the end of the analysis by observing the weight change of the catalysts.

3.5 Photoreaction

3.5.1 The Procedures of Photoreaction

Figure 3.4 shows the set up of photoreaction. Photoreaction of POME was carried out in a 500-mL pyrex quartz reactor. Transient photodegradation of POME samples was determined via COD analysis. The chemical oxygen demand (COD) of the original POME sample was analyzed using *Hach DRB-200 COD reactor* before each reaction (refers to Section 3.5.2). Thereafter, 300 mL of POME and 0.25 g of 2wt% Cu/TiO₂ catalyst were mixed in-situ and rigorously stirred for 2 h for adsorption equilibrium. Subsequently, UV lamp (1000 W) was switched on to initiate the reaction. An aliquot (3 mL) of POME sample was withdrawn from the reactor every 15 min interval for COD measurements. The COD reduction achieved was recorded. The experiments with catalyst of other metal loadings, viz. 5wt%, 10wt%, 15wt%, 20wt% and 25wt% of copper metal followed the same outlined procedures.

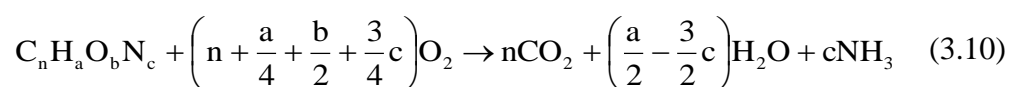


Figure 3.4 The setup of photoreaction.

3.5.2 Chemical Oxygen Demand (COD) Measurements

Chemical oxygen demand (COD) is used as a measure of oxygen requirement of a sample that is susceptible to oxidation by strong chemical oxidant (Clair et al., 2003). It is always used to measure the amount of organic compounds in water. Most applications of COD is to determine the amount of organic pollutants found in water or wastewater (Lenore et al., 1999). Indirectly, COD has become a useful tool to measure the water quality.

The basis for the COD test is to fully oxidized all organic compounds to carbon dioxide with a strong oxidizing agent under acidic conditions. The amount of oxygen required to oxidize an organic compound to carbon dioxide, ammonia, and water is given by Equation (3.10).



For current study, the model of COD reactor used was Hach DRB-200 COD *Reactor*. Before the COD test, the withdrawn POME samples underwent centrifugal separation process to separate the catalyst from the sample. Other than sample, an oxidation vial was also prepared. Oxidation vial is a light-sensitive liquid and must be closed in box if it is unused.

A volume of 2.0 ml of the prepared POME samples was pipetted into the oxidation vial. Concurrently, a blank vial was prepared by pipetting clean water into the vial. The purpose of blank vial was as the datum. These vials were inverted several times before and post-mixing to ensure the bottom sediment transformed into suspension; hence well mixing of sample and vial. The vials with the content would become very hot upon mixing due to oxidation. The mixture in the vials was in brownish yellow colour. COD concentration far exceeding the stated range (0-1500 ppm) showed an adversely affect color formation (green colour), resulting in a false reading that appeared within the range of the method. The vial was then placed in the DRB200 reactor followed by heating to 423 K and maintained at the stipulated temperature for 2 h to ensure complete oxidation of the organics in the sample. Subsequently, the vial was gently transferred into a rack for convective cooling to room temperature. During the transfer, any shaking of the vial was avoided as the resuspension of sediment in the vial would disturb the COD reading. After cooling, the exterior wall of the vials was thoroughly cleaned and the samples were ready to be analysed.

Place the blank vial into the cell holder, close the lid and set the instrument zero. The instrument displays L1 when the zeroing is completed. Now, the sample vials can be analysed through the same steps. The instrument reads the barcode and reads the sample. Results are in mg/L COD and measurements can be repeated for several times to ensure accuracy.

CHAPTER 4

RESULTS AND DISCUSSION

4.1 Introduction

In this chapter, physicochemical properties of the prepared catalysts were determined via several well-established techniques viz. XRD, XRF, BET and TGA. Subsequently, photoactivity of the catalysts was firstly tested with methylene blue solution followed by photodegradation of POME wastewater collected from the Felda Lepar Hilir 3. Finally, correlations between the photocatalytic activity and the physicochemical properties were thoroughly discussed.

4.2 Characterization of catalysts

4.2.1 XRF Analysis

Table 4.1 shows that the actual compositions of the catalysts are considerably consistent with the desired compositions.

Table 4.1 Results obtained from XRF test.

Catalyst	Actual wt% of TiO ₂	Actual wt% of Cu
2wt% Cu/TiO ₂	92.79	2.45
5wt% Cu/TiO ₂	88.78	5.65
10wt% Cu/TiO ₂	83.02	11.29
15wt% Cu/TiO ₂	76.77	17.97
20wt% Cu/TiO ₂	70.23	22.88
25wt% Cu/TiO ₂	62.86	27.77

The deviations of the composition for the catalysts prepared ranged from 11% to 22%. The catalyst formulation that has highest deviation is 2wt% Cu/TiO₂ which recorded 22% deviation from the desired wt% while 25wt% Cu/TiO₂ exhibited least deviation from the desired wt% which is only 11%.

4.2.2 XRD Diffraction Pattern

Figure 4.1 shows the XRD diffraction pattern for all the catalysts prepared ranged from $2\theta = 3^\circ$ to 80° . It can be inferred from Figure 4.1 that the crystalline phase of the TiO₂ invariant with Cu loading as the shapes and relative intensity of the characteristic TiO₂ peaks remained unchanged. A new finding is discovered by comparing the XRD patterns in Figure 4.1. There is an obvious difference occurred near $2\theta = 12.9^\circ$. A distinguishable peak appeared near $2\theta = 12.9^\circ$ for all the catalysts except for 2wt% Cu/TiO₂. The peak intensities increased with copper loading; hence this peak should be copper's peak. The possible reason for the disappearance of the Cu peaks in the 2wt% Cu/TiO₂ samples is due to the low dopant content in the catalyst.

In particular, Figure 4.2 shows the amplified region of interest for the diffraction patterns at $2\theta = 35^\circ$ to 45° . Interestingly, there were peaks at $2\theta = 36.7^\circ$ for 20wt% and 25wt% Cu/TiO₂ specimens. These peaks can be assigned to CuO species. For other samples, it is believed that the low content of CuO species in the catalyst formulations contributes to its disappearance from the diffractogram.

According to the research by Yoong et al.(2009), the peaks at $2\theta = 25.34^\circ$ and $2\theta = 27.42^\circ$ correspond to the main peak of anatase and rutile, respectively, while CuO (*tenorite*) diffraction peaks can be observed near $2\theta = 35.6^\circ$ and 38.73° . Besides, Slamet et al. (2005) also concurred that the CuO diffraction peaks appeared at $2\theta = 35.6^\circ$ and 38.73° . In addition, Slamet et al. (2005) also discovered that, CuO diffraction peak near $2\theta = 35.6^\circ$ will not appear if the Cu contain is lower than 3 wt%. From Figure 4.1 and Figure 4.2, the peak for CuO can barely be seen for 2wt% and 5 wt% of Cu/TiO₂. However, for the remaining catalysts, small peaks were observed at near $2\theta = 36.7^\circ$ which believed is the peak for CuO.

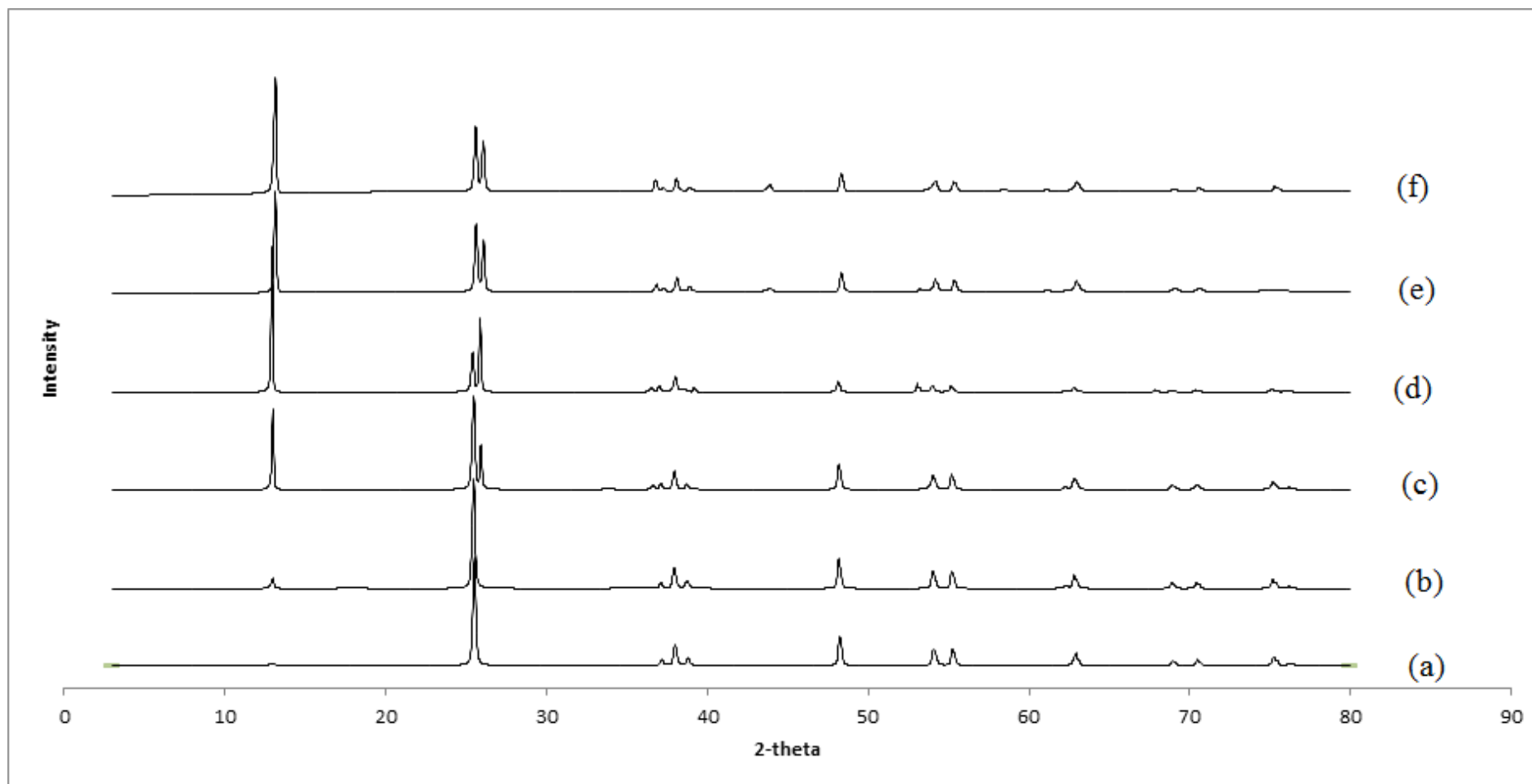


Figure 4.1 Complete XRD patterns for (a) 2wt% Cu/ TiO₂ (b) 5wt% Cu/ TiO₂ (c) 10wt% Cu/ TiO₂ (d) 15wt% Cu/ TiO₂ (e) 20wt% Cu/ TiO₂ (f) 25wt% Cu/TiO₂.

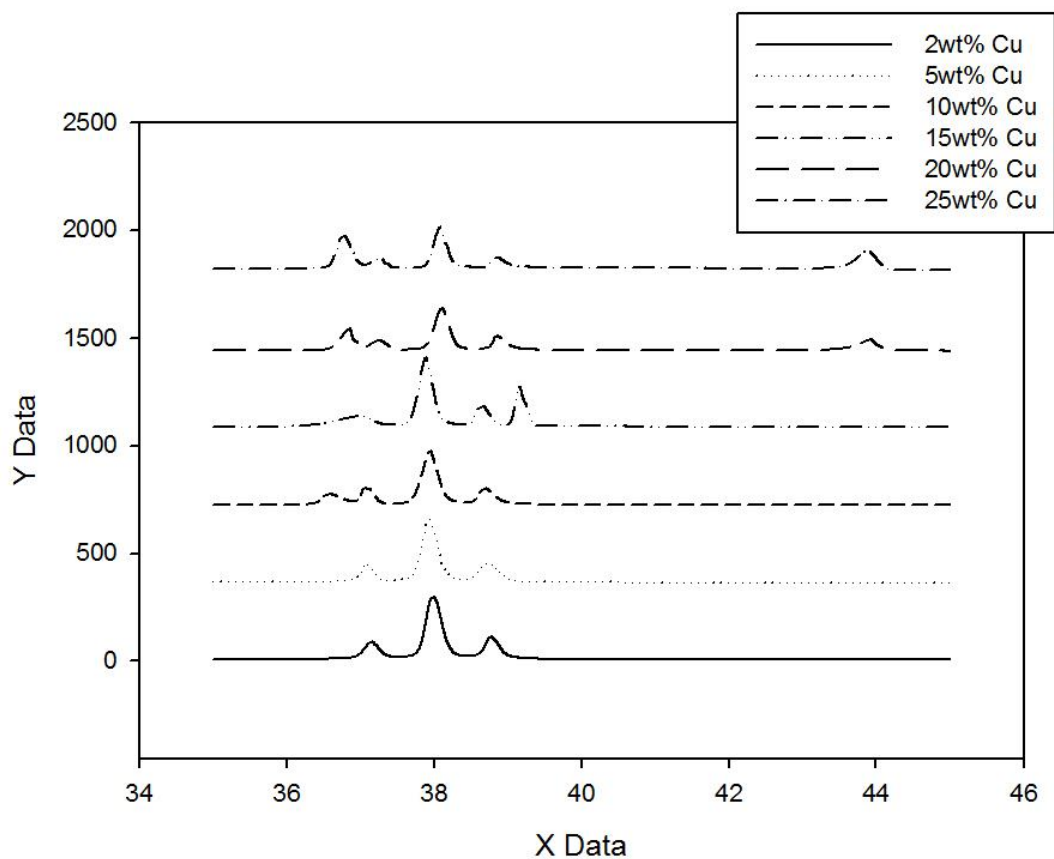


Figure 4.2 XRD patterns for catalyst prepared from $2\theta = 35$ to 45° .

On the other hand, the crystalline size of CuO for each of the catalysts prepared was calculated using Scherrer equation (Equation 3.3) and tabulated in the Table 4.2.

Table 4.2 Crystalline size of CuO for each catalyst.

Wt% of Cu	Crystalline size (nm)
2	44.8
5	43.1
10	41.8
15	49.1
20	44.3
25	44.9

From Table 4.2, it can be observed that the crystalline size of CuO for the catalysts is considerably consistent, ranging from 41.8 to 49.1 nm. The difference between the largest and smallest CuO crystal observed is about 7.3 nm, which is about 14%.

4.2.3 Density of Catalysts

Table 4.3 and Figure 4.3 show the density measurements for 2wt% Cu/ TiO₂ as a representative sample. For accuracy, the results were repeated for five cycles for each catalysts and then averaged.

Table 4.3 The density of 2wt% Cu/ TiO₂.

Cycle	Volume (cm ³)	Density (gcm ⁻³)
1	0.6390	2.7816
2	0.6412	2.7718
3	0.6436	2.7617
4	0.6454	2.7541
5	0.6454	2.7538

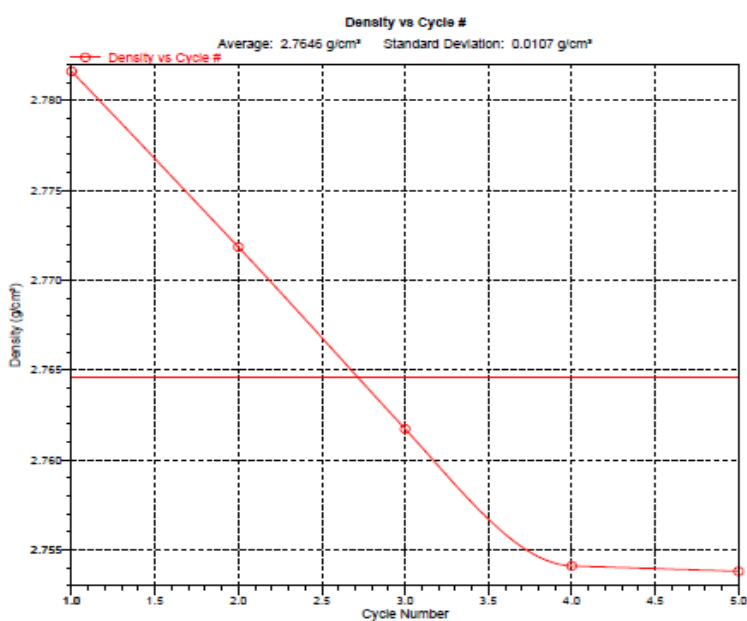


Figure 4.3 The density of 2wt% Cu/ TiO₂.

From Table 4.3, the density of 2wt% Cu/ TiO₂ was 2.76 g cm⁻³ from the averaged five measurements. For 5wt%, 10wt%, 15wt%, 20wt% and 25wt% Cu/ TiO₂, the results are summarized in Table 4.4.

Table 4.4 The results obtained from gas pycnometer.

Wt% of Cu/ TiO ₂	Sample mass (g)	Volume (cm ³)	Density (g cm ⁻³)
2	1.7774	0.6429	2.76
5	4.0565	1.2330	3.29
10	4.1365	1.2884	3.21
15	4.7736	1.4709	3.24
20	4.8631	1.5339	3.17
25	5.2581	1.6891	3.11

It can be seen that the density of the composites increased with the incorporation of Cu-metal into the TiO₂ lattice. Indeed, Geankoplis (2003) has mentioned that the theoretical density of a composite compound, in the current study, Cu/TiO₂ can be estimated using Equation (4.1):

$$\rho_{\text{Cu/TiO}_2} = \varepsilon \rho_{\text{TiO}_2} + (1 - \varepsilon) \rho_{\text{Cu}} \quad (4.1)$$

where ρ is the density (g/cm³) and ε is the volume fraction of TiO₂ which can be calculated by using Equation (4.2):

$$\varepsilon = (\text{wt\% of TiO}_2 / \rho_{\text{TiO}_2}) / [(\text{wt\% of TiO}_2 / \rho_{\text{TiO}_2}) + (\text{wt\% of TiO}_2 / \rho_{\text{Cu}})] \quad (4.2)$$

The theoretical density of the catalysts was duly estimated using Equations (4.1) and (4.2) and the calculated values illustrated in Figure 4.4. From Figure 4.4, the theoretical density of catalysts increased with the Cu content.

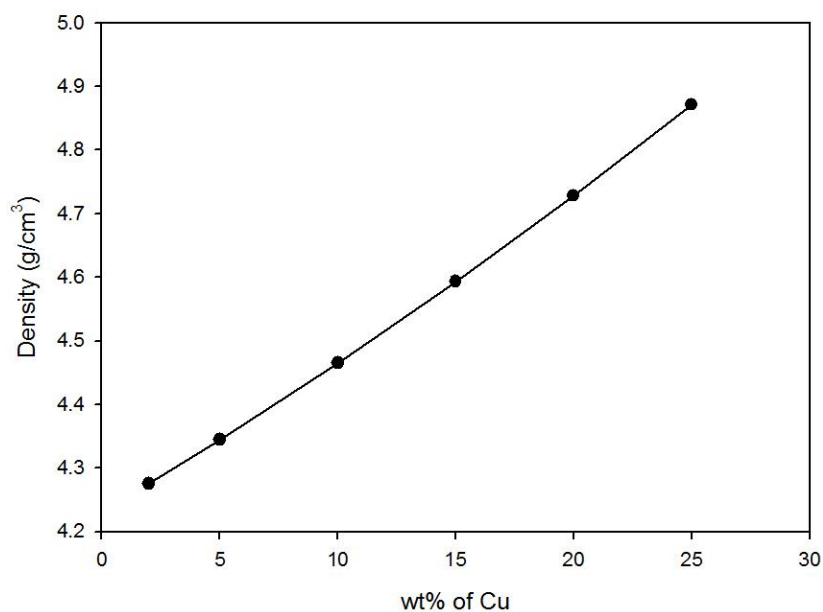


Figure 4.4 The density value obtained from Equations (4.1) and (4.2).

For comparison purpose, density results from both the Tables 4.4 and Figure 4.4 are plotted in Figure 4.5. Apparently, the results obtained from gas pycnometer are much lower than the calculated theoretical values. Theoretically, the density of the catalyst should increase gradually with the increment of Cu content. Nevertheless, based on Figure 4.5, the measured density has exhibited contrasting trend. This might due to the porous structure of catalysts after calcination process. During calcination process, the volatile contents in the catalysts such as nitrous oxide and water were heated and spontaneously removed from the catalysts, leaving cavities inside the catalysts and eventually causing the deviations in measured and theoretical densities. This phenomenon is confirmed by the liquid N₂ physisorption analysis which will be discussed in section 4.2.4.

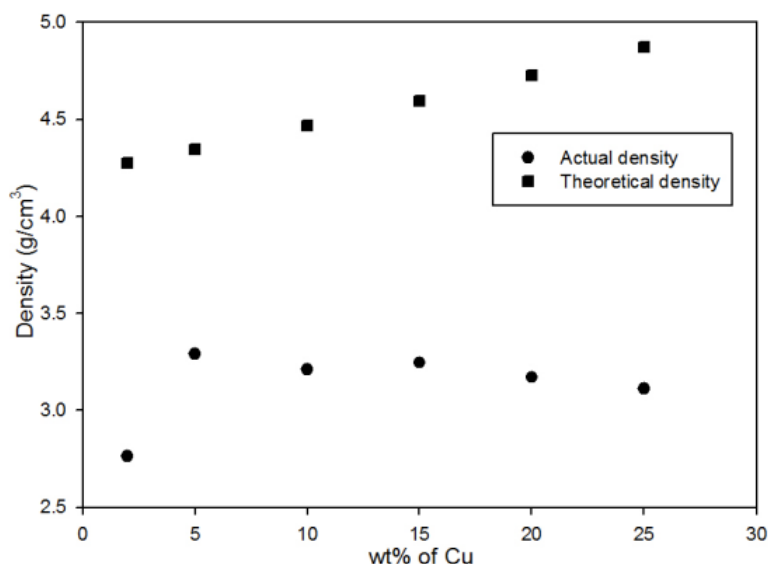


Figure 4.5 Comparisons of densities obtained from gas pycnometer and Equations (4.1) and (4.2).

4.2.4 Liquid N₂ Physisorption

In Figure 4.6, the isotherms are concave to the P/P^0 axis, almost linear and finally convex to the P/P^0 axis. The characteristic of this type of isotherm is symptomatic of type II isotherm (Rouquorel et al., 2013). During the adsorption process, the adsorbed N₂ layer condensed when the equilibrium pressure reaching the saturation vapour pressure. The uptakes at the knee of isotherms at high relative pressures represent the completion of the monomolecular layer and beginning of the formation of the multimolecular layer of N₂. Besides, narrow hysteresis loops were observed for all the isotherms obtained between the adsorption and desorption isotherms. These trends can be explained by inter-particle capillary condensation of N₂ in the catalyst particles during adsorption-desorption process.

The BET specific surface area of the catalysts obtained from liquid N₂ physisorption is shown in Table 4.5. It can be seen that the measured surface area decreased with Cu loadings. The highest measured surface area was 11.42 m²/g for 2 wt% Cu/TiO₂, followed by 10.23 m²/g for 5 wt%, 9.98 m²/g for 10 wt%, 9.17 m²/g for 15 wt%, 7.49 m²/g for 20 wt% and finally 6.20 m²/g for 25 wt% of Cu/TiO₂. This can be explained

by the crystallite formed upon the impregnation of Cu metal that has blocked the pores of TiO₂ support; hence a decrease in BET specific surface area.

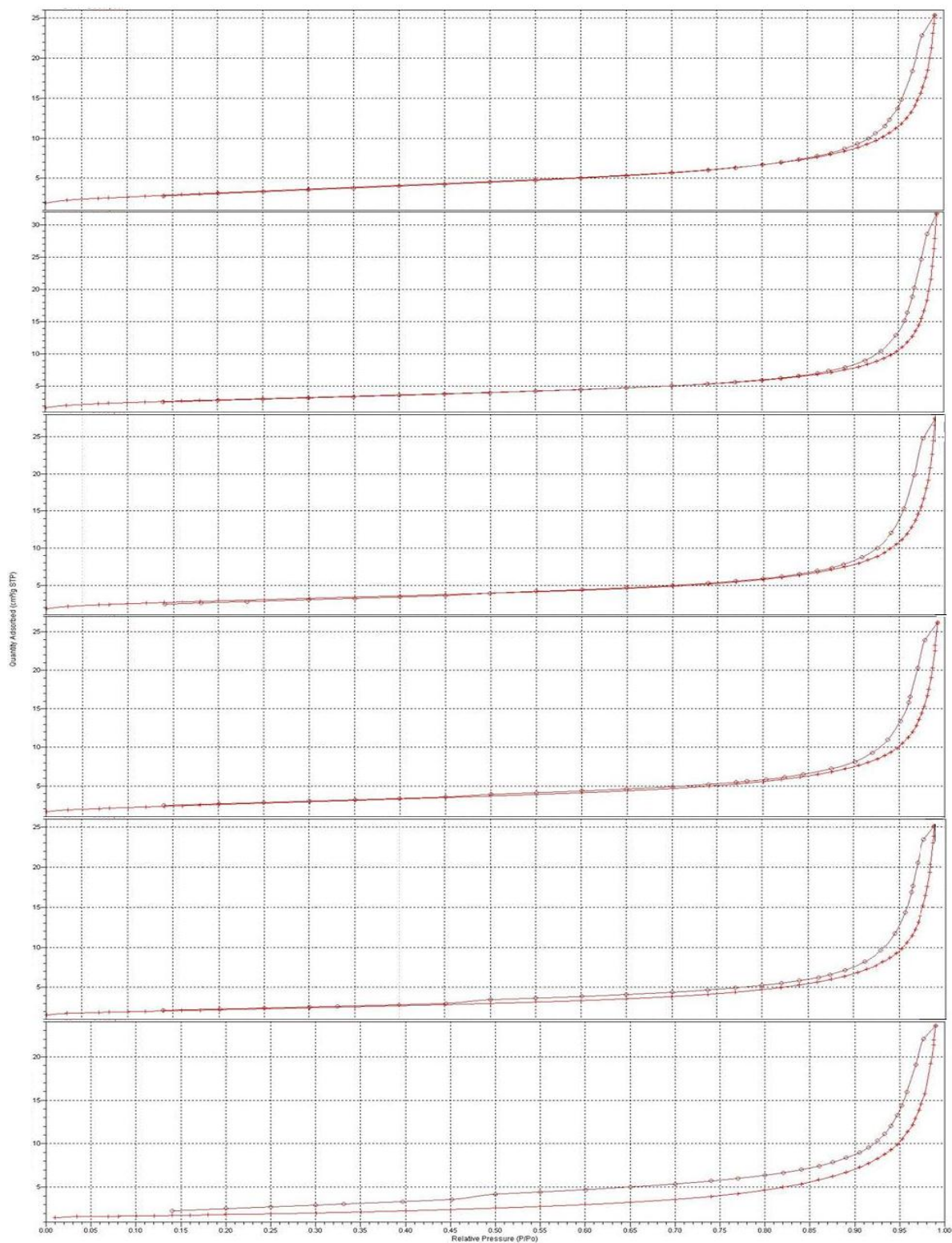


Figure 4.6 The isotherms for 2wt%, 5wt%, 10wt%, 15wt%, 20wt%, and 25wt% of Cu/TiO₂ (from top top to bottom).

Table 4.5 The BET specific surface area for different catalysts

Wt% of Cu/TiO ₂	BET specific surface area (m ² /g)
0	12.92
2	11.42
5	10.23
10	9.98
15	9.17
20	7.49
25	6.20

As aforementioned, the volume of the pores can be determined by using Equation (3.5). Table 4.6 shows both adsorption and desorption volume for the catalysts prepared. From Table 4.6, it can be concluded that there is not much difference between the adsorption and desorption volume for each of the catalysts. In terms of specific volume, 5wt% of Cu/TiO₂ seems to have largest adsorption and desorption volume, which are 0.049 and 0.0496 cm³/g respectively. Significantly, the pore volume for both adsorption and desorption decreased in the order of 10wt% > 15wt% > 2wt% > 20 wt% > 25 wt%.

Table 4.6 The pore volume for different catalysts.

Wt% of Cu/TiO ₂	Pore volume (cm ³ /g)	
	Adsorption	Desorption
2	0.040005	0.039855
5	0.049071	0.049593
10	0.042037	0.042894
15	0.041079	0.040976
20	0.038661	0.039213
25	0.036669	0.036841

Besides, the pore diameter can also be determined. Table 4.7 shows the pore diameter for both adsorption and desorption process of the prepared catalysts. Unlike pore volume, the difference between adsorption pore diameter and desorption pore diameter is quite significant. Generally, the adsorption pore diameter is larger than

desorption pore diameter. According to Table 4.7, 20wt% Cu/TiO₂ seems to have the largest pore diameter at 23.38 nm. On the other hand, the catalyst with smallest pore diameter was 2wt% Cu/TiO₂ (13.91 nm). In terms of desorption pore diameter, the largest pore diameter was 19.83 nm for 5wt% Cu/TiO₂, whilst the smallest measured pore diameter was 13.79 nm for 25wt% Cu/TiO₂. These measured pore volume and pore size proved that the catalysts possessed porous structure, consistent with the findings from the prior density measurements.

Table 4.7 The pore diameters for different catalysts.

Wt% of Cu/TiO ₂	Pore diameter (nm)	
	Adsorption	Desorption
2	13.91	13.85
5	20.69	19.83
10	19.67	17.47
15	17.93	17.63
20	23.39	19.76
25	23.38	13.79

Based on the results obtained, the catalysts can be considered as mesoporous catalysts as the pore diameters were all fallen into the range of mesoporous material (2 to 50 nm).

4.2.5 TGA

Figure 4.7 presents the derivative weight profile of the prepared catalysts as a function of temperature for ramping rate of 5 K/min under air-blanket calcination. The derivative weight profiles show that only one peak representing the rate of weight loss, which occurred from 450 to 550 K was obtained. Hence, this peak is an indicative of thermal decomposition of copper nitrate to CuO.

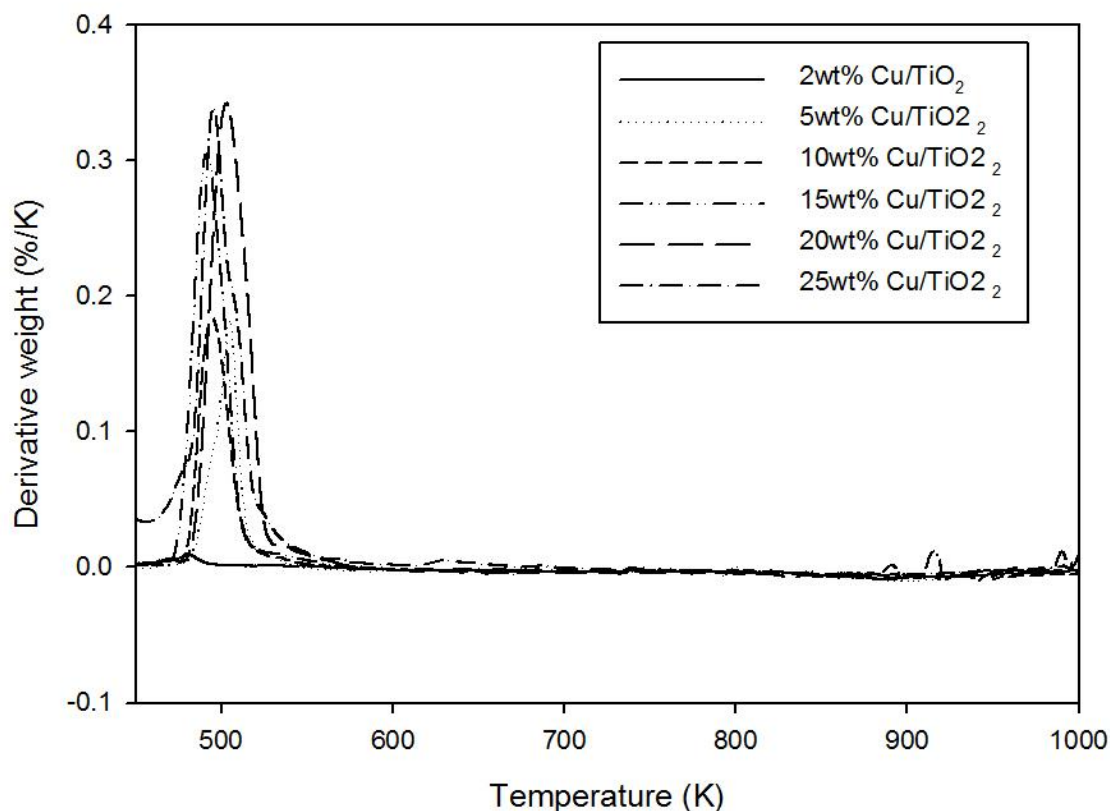


Figure 4.7 Derivative weight profile of catalysts prepared

The derivative weight profile for mass reduction from $T = 450$ to 550 K were amplified and plotted in Figure 4.8. The peak for 2wt% Cu/TiO₂ was undetectable. This might be due to low content of Cu in the particular catalyst and eventually low content of copper oxide which leads to insignificant decomposition. This was also confirmed by the findings of XRD as discussed in Section 4.2.2. Other than that, the peak for all the other prepared catalysts occurred within this temperature range.. Significantly, the maximum peak temperatures seem to be invariant with the Cu loading. However, it can be observed that the intensity of the peaks increased with the wt% of Cu, which indicating higher content of copper nitrate present in the particular catalyst.

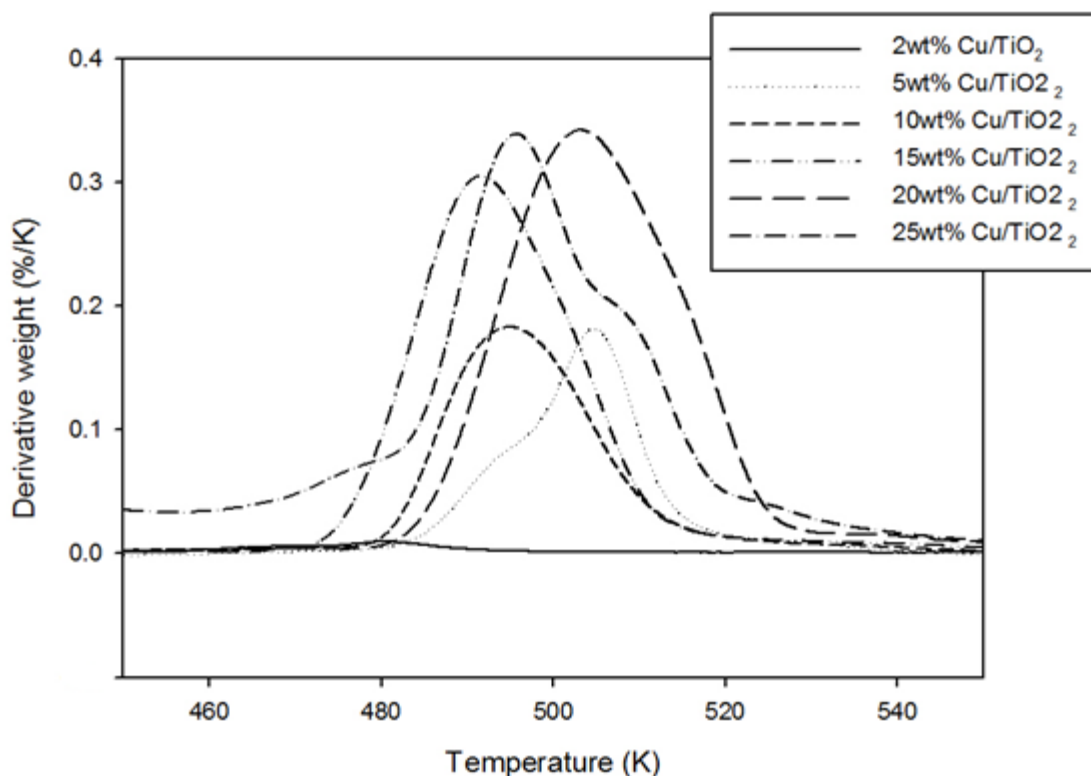


Figure 4.8 Derivative weight profile of catalysts prepared from T=450 to 550 K.

4.3 Photoreaction Studies

4.3.1 Photoreaction of Methylene Blue

Before conducting photoreaction with POME solution, the photoreactivity of catalysts prepared were tested with photoreaction over methylene blue. Methylene blue is a heterocyclic aromatic organic compound with the molecular formula $C_{16}H_{18}N_3SCl$. Besides, it is also a well-studied compound and widely employed for photocatalysis benchmarking. It yields a dark blue colour solution when dissolved in water and decrease in colour intensity upon decomposition. The concentration of methylene blue solution can be obtained accurately by using UV-Vis. These aforelisted reasons made methylene blue solution suitable to use as a tester for the catalysts.

Before the concentration of samples was measured using UV-Vis instrument, calibration curve for methylene blue was. After that, all photoreaction runs were

conducted for 1 h. An aliquot (3 ml) of methylene blue was withdrawn from the reactor every 15 min intervals. These samples were analysed and the actual concentration was obtained by referring back to the calibration curve. Figure 4.9 shows a typical calibration curve obtained during the measurement. From Figure 4.9, the intensity of the absorbance peak decreased with the concentration of methylene blue.

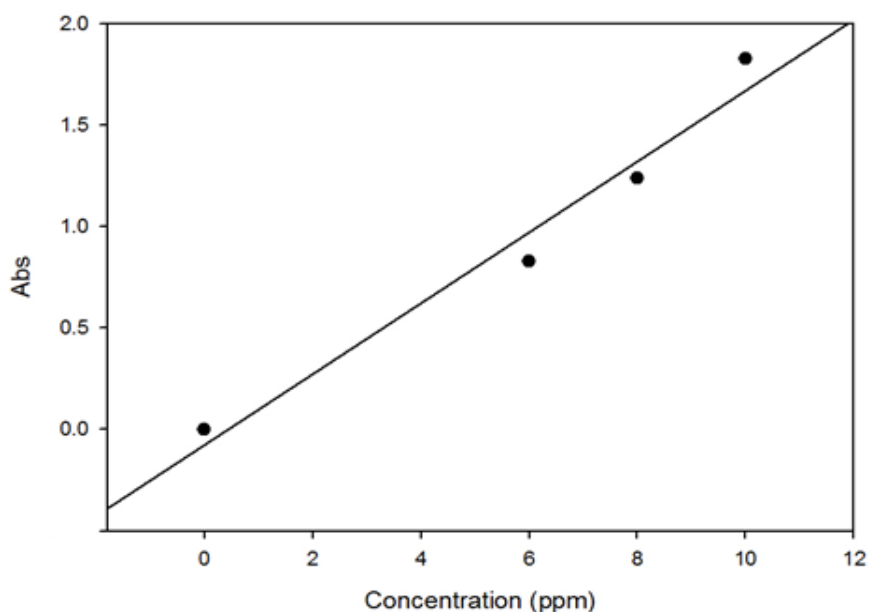


Figure 4.9 The calibration curve for methylene blue.

The results obtained from photoreaction of methylene blue with different catalysts are presented in Table 4.8. From the results, the reactivities of the all the catalysts prepared are confirmed as an obvious reduction in concentrations of methylene blue were observed after photoreactions.

Table 4.8 The results obtained from photoreaction of methylene blue.

Time	Conc (ppm)					
	2wt%	5wt%	10wt%	15wt%	20wt%	25wt%
0	10.87	11.42	11.43	10.43	10.16	9.90
15	9.13	10.97	10.83	9.55	8.42	9.13
30	8.87	9.75	9.14	8.73	7.35	9.00
45	8.33	8.61	8.55	7.48	6.58	7.81
60	6.57	8.48	6.39	8.80	5.76	6.49

4.3.2 Decomposition of POME

After confirming the photo-reactivity of the prepared catalyst, photoreactions of POME were conducted. For every reaction, the catalyst was magnetic stirred with diluted POME sample for 2 h to attain equilibrated adsorption. The COD of the POME samples were analysed and the results obtained were tabulated into Table 4.9. From Table 4.9, the lowest COD value obtained after was 173 ppm, which was achieved by photoreaction with 20wt% of CO/TiO₂ catalyst. However, no conclusion can be made as the experiments having the different starting COD value.

Table 4.9 The results of photoreaction on POME for various catalysts.

t (min)	COD					
	2wt%	5wt%	10wt%	15wt%	20wt%	25wt%
0	232	220	214	256	237	229
15	228	188	208	204	210	215
30	226	192	196	212	178	214
45	199	186	194	209	179	187
60	199	182	174	205	173	181

Figure 4.10 shows the normalized COD versus time graph for comparison purposes. Based on the results, 20wt% of Cu/TiO₂ seems to be the best catalyst as it shows the highest catalytic reactivity by decomposing most organics in POME among the catalysts prepared. The normalized COD obtained for 20 wt% Cu/TiO₂ is 0.73. The normalized COD for the other catalysts increased in the order of 20wt%, 25wt%, 15wt% 10wt%, 5wt% and 2wt% of Cu/TiO₂. The 2wt%Cu/TiO₂ shows the least catalytic reactivity as the normalized COD obtained after 1 h photoreaction was 0.85, which was apparently higher.

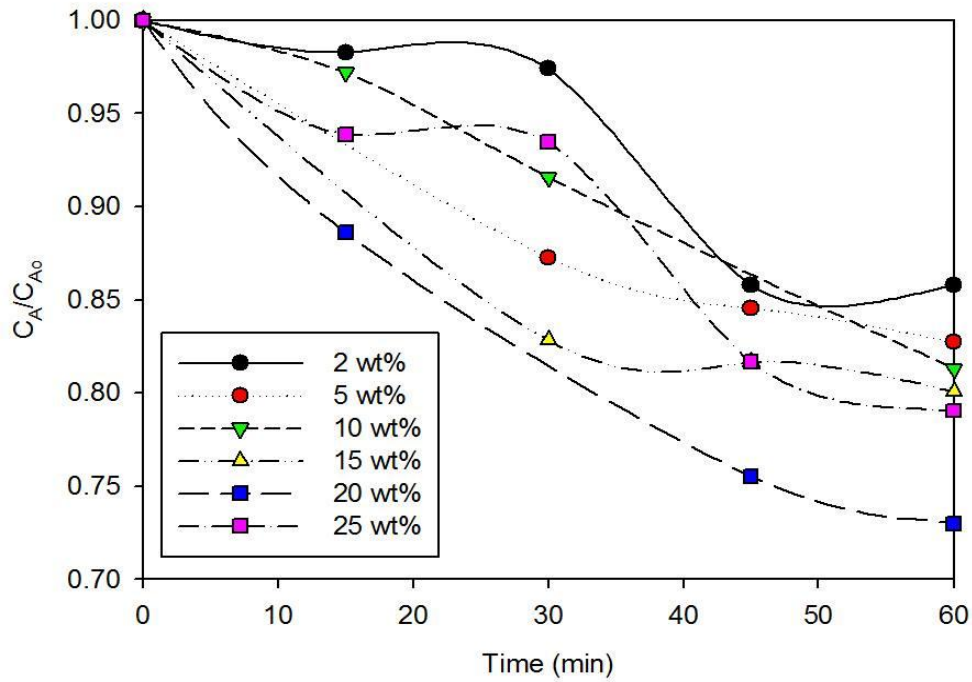


Figure 4.10 Normalized COD for photoreaction of various wt% of catalysts.

Besides, the conversion of organics in the POME was obtained by using Equation (4.3) and tabulated into Table 4.10:

$$\text{Organics conversion, } X = \frac{\text{COD}_i - \text{COD}_f}{\text{COD}_i} \quad (4.3)$$

whereby COD_i represents COD value before photoreaction begins and COD_f is the COD value after 1 h of photoreaction.

Based on Table 4.10, 20wt% Cu/TiO₂ yielded the highest conversion with 27% of the initial organics was decomposed within 1 h. According to the conversion trend, for the Cu content lower than 20%, the conversion was increasing with the Cu content. Figure 4.11 is plotted to show the conversion of sample after 1 h of photoreaction and the XRF results for 2wt% to 20wt% of Cu/TiO₂.

This can be explained by the higher composition of Cu widen the energy band gap of the catalysts for electron excitation. In other words, with the presence of higher Cu

content, the catalysts are easily to be excited, eventually enhancing the reactivity of the catalysts and as well as the conversion of the POME samples.

Table 4.10 The conversions of POME for various catalysts after 1 h of photoreaction.

Wt% of catalyst	Conversion, X
2	0.1422
5	0.1727
10	0.1869
15	0.1992
20	0.2700
25	0.2096

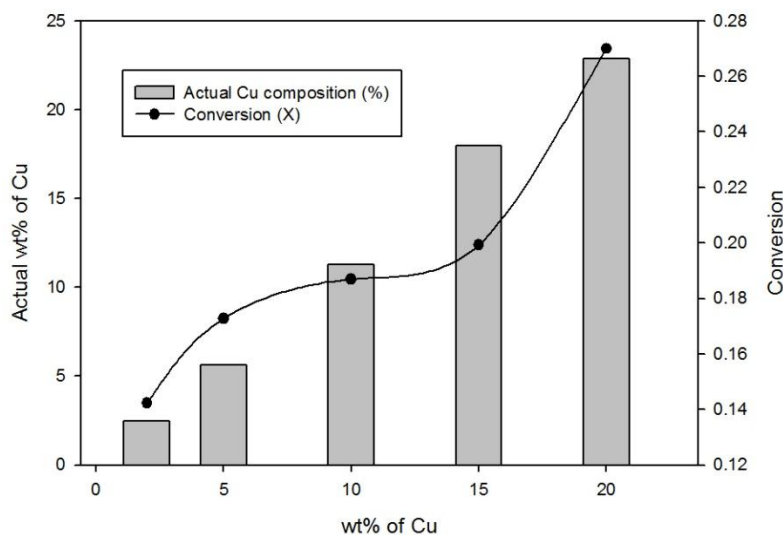


Figure 4.11 The actual wt% of Cu and conversion of sample for 2wt% to 20wt% of Cu/TiO₂.

However, beyond 20 wt%Cu/TiO₂, higher wt% of Cu seems to be non-effective towards reactivity of catalysts. Figure 4.12 is plotted to show the conversion of sample after 1 h of photoreaction and the pore size for 20wt% and 25wt% of Cu/TiO₂. Based on the results obtained, the conversion profile dropped gradually after 20wt% of Cu/TiO₂. This can be explained by size of the pore diameter discussed in section 4.2.4. Traditionally catalysts with larger pore diameters (both adsorption and desorption diameter) were believed to have high reactivity as no spatial restrictions

upon substrate entering such large pores. This is further confirmed by the past researchers (Bayne et al., 2013; Pellin et al., 2005) .

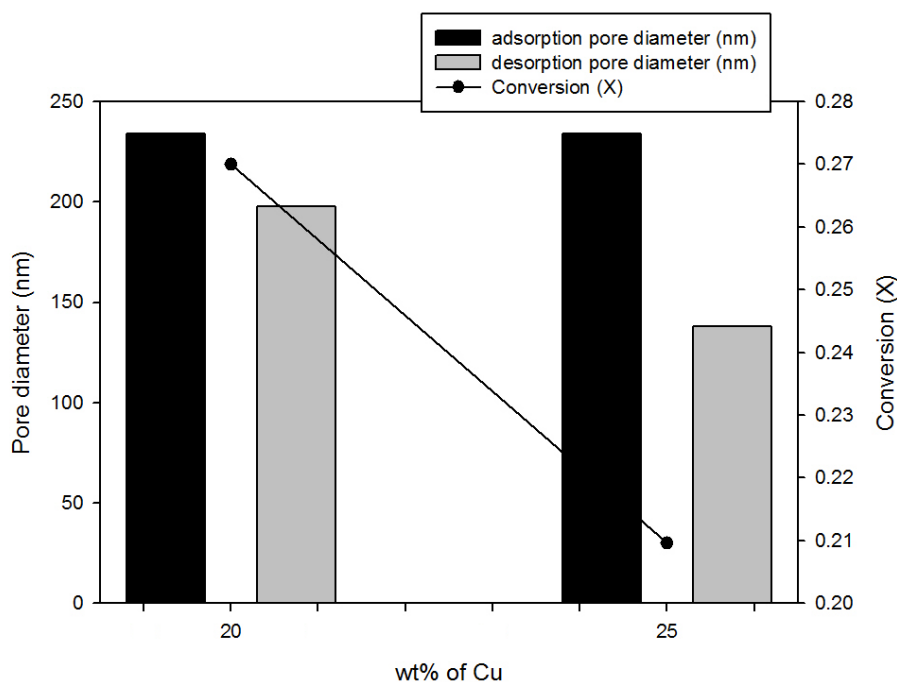


Figure 4.12 The conversion and the pore diameter for 20wt% and 25wt% of Cu/TiO₂.

Based on Figure 4.12, the adsorption pore diameter for both of the catalysts is almost similar while the desorption pore diameter of 20wt% Cu/TiO₂ is apparently bigger than the other. The large size of both adsorption and desorption pores allow the accessibility of the substrate, which enhanced the reactivity as well as the organics degradability.

4.3.3 Power-Law Modelling

Judging by the the trend of decomposition rate of organics in POME, the kinetics should be able to be described by the power-law model as given in Equation (4.4):

$$-r_o = kC_A^\alpha \quad (4.4)$$

where $-r_o$ = rate of organics decompose (ppm min^{-1})

k = specific reaction rate (ppm min g^{-1})

C_A = concentration of organics in POME (ppm)

α = order of the reaction

The method used to determine the order and specific reaction rate constant is integral method. According to Fogler (2006), if the assumption of the reaction order is correct, a appropriate plot of the concentration-time should be linear.

A few orders of reaction such as 1st, 2nd and 3rd were tested during the data fitting exercise. Upon comparison, 2nd order models seem to be the best fitted with the decomposition rate data.

According to Fogler (2006), Equation (4.4) was further derived and linearized into Equations (4.5) and (4.6).

$$-r_o = -\frac{dC_A}{dt} = kC_A^\alpha \quad (4.5)$$

$$\frac{1}{C_A} - \frac{1}{C_{A0}} = kt \quad (4.6)$$

where C_{A0} is denoted for initial concentration of organics in POME in ppm. Based on Equation (4.6), if the reaction fits second order decomposition, a straight line graph of concentration versus time would be obtained, with the slope of k and y-intercept of $(1/C_{A0})$. Figure 4.13 is plotted to show the relationship between $(1/C_{A0})$ and time. Straight line graph were obtained for all sets of the data from Table 4.9 with $R^2 > 0.90$. Therefore, second-order power law can adequately describe the POME photo degradation kinetics.

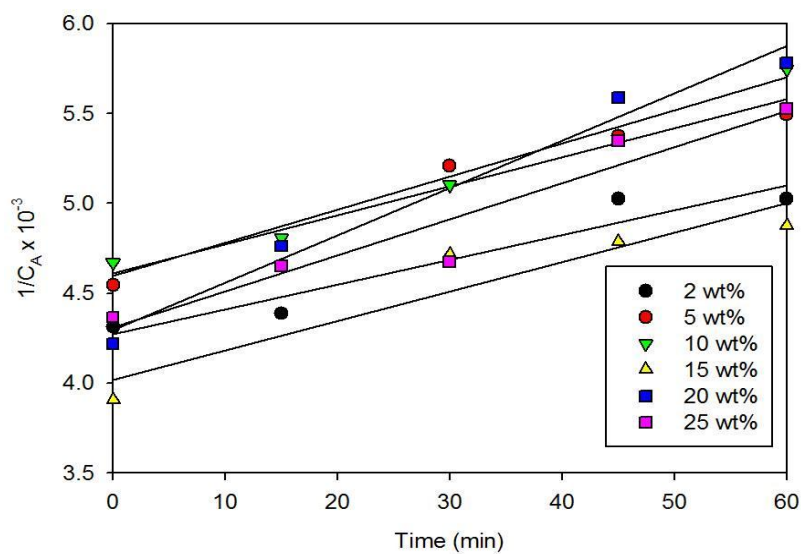


Figure 4.13 Graph for second-order reactions.

The adequacy of power-law model for extracting essential information from organics decomposition data was appraised by a rigorous error analysis. Figure 4.14 shows a parity plot suggesting a fairly good agreement between predicted ($1/C_A$) value and observed ($1/C_A$) value with R^2 -value of 0.909.

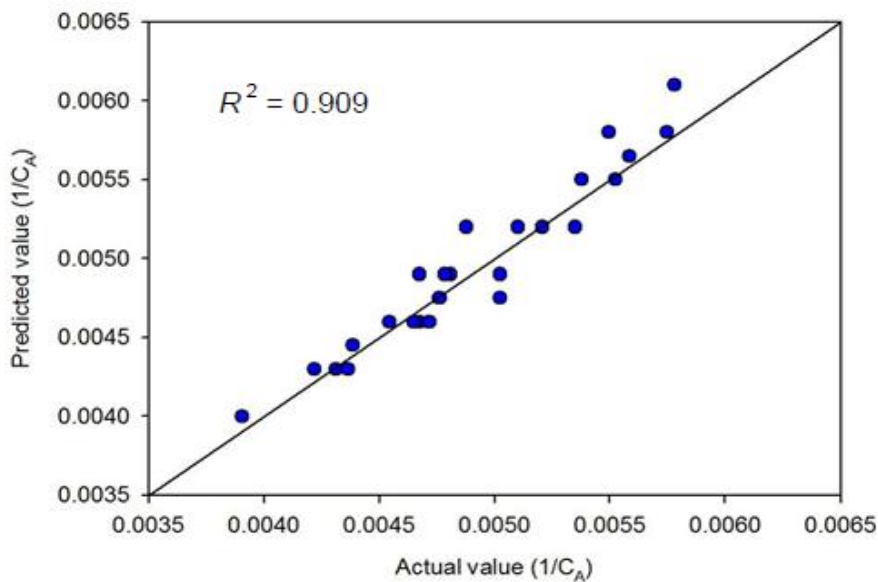


Figure 4.14 Comparison between predicted ($1/C_A$) value and actual ($1/C_A$) value.

Additionally, as the residual plot depicted in Figure 4.15 evinces no obvious pattern, hence it can be assumed that power-law model is sufficient (Montgomery, 1997).

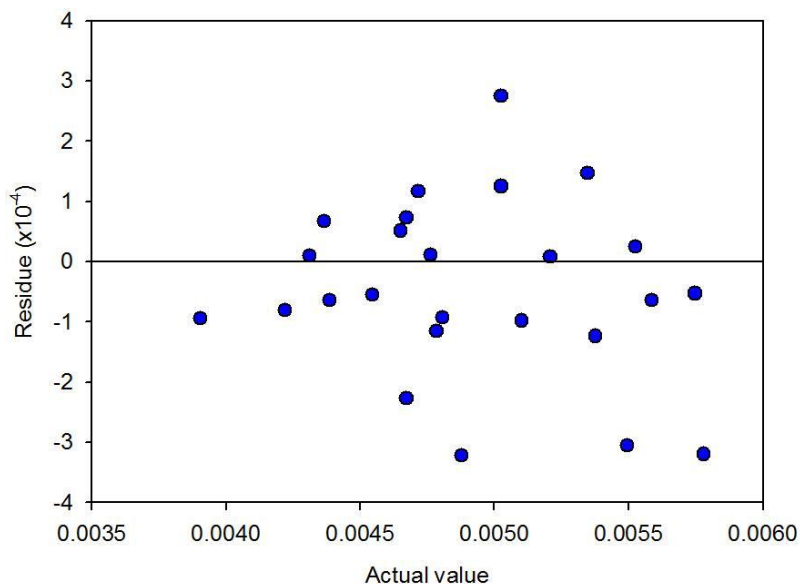


Figure 4.15 Residual plot for decomposition rate of organics in POME.

However, the specific reaction constant k values obtained were different from one another. Table 4.11 shows the k -values obtained for each of the catalysts prepared.

Table 4.11 The specific reaction constants obtained from photoreactions on POME.

Wt% of Cu	Specific reaction constant (k) $\times 10^5$ (ppm min) ⁻¹
2	1.19
5	1.58
10	1.79
15	1.62
20	2.60
25	1.93

Based on Table 4.11, these obtained k -values are reasonably shows a trend with optimum at 20wt% of Cu, which is consistent with the pore diameter discussed earlier that lead to higher conversion. The k value for 20 wt% Cu/TiO₂ is apparently higher

compared to the others, which is 2.60, followed by 25wt%, 10wt%, 15wt%, 5wt% and lastly 2wt%.

In conclusion, the organics in POME decomposed by following second-order reaction, with different k -values.

4.3.4 Optimum Catalyst Loading

Three sets of photoreaction were conducted with catalyst loadings of 0.5 g/L, 0.83 g/L and 1.0 g/L to determine the optimum catalyst loading for POME photo-degradation. The catalyst chosen for catalyst loading investigation was 20wt% of Cu/TiO₂ as it was previously proven as the optimum performer. The methodology was similar to the procedures that were described in Section 3.5.1. The reaction time was fixed at 1 h. The COD readings of each set of reaction were taken before and post reaction. The outcomes of the experiments are presented in Figure 4.16.

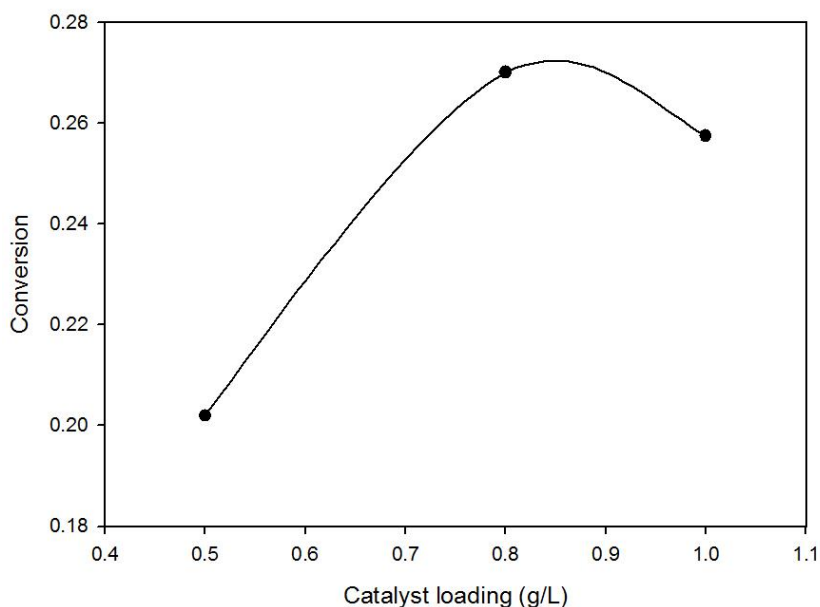


Figure 4.16 Graph of conversion versus catalyst loading.

Based on the results plotted in Figure 4.16, the optimum catalyst loading is 0.83 g/L. About 27% of the organics is converted within 1 h. Generally, higher catalyst loading

indicates higher conversion of organics in POME. Thus, before catalyst loading of 0.83 g/L, the conversion of organics is increasing with the catalyst loading. However, after 0.83 g/L, reduction of organics conversion was observed. This can be explained by the catalyst loading which is high enough to decompose more substrate (compared to 0.5 g/L) but did not inhibit the penetration of UV light as opposed to 1.0 g/L.

Thus, as a conclusion, the catalyst loading will also affects the performance of the catalyst. For 20wt% of Cu/TiO₂, the optimum catalyst loading is 0.83 g/L.

4.3.5 Longevity Study

Previously, the catalyst with highest reactivity (20wt% Cu/TiO₂) and optimum catalyst loading (0.83g/L) were determined. A reaction was conducted with these findings to determine the capability of organics decomposition within 7 h. The POME samples were taken for every hour for COD analysis.

Figure 4.17 shows the comparisons of colour of the samples taken for t=0 and 7 h. Based on optical observation, the colour of POME is getting lighter as the UV radiation time increased.

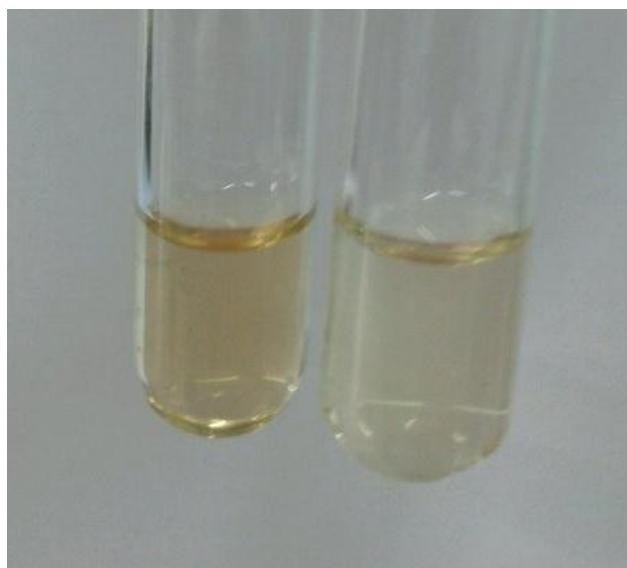


Figure 4.17 The POME samples for t=0 h (left) and t=7 h (right).

The results obtained from the experiment are shown in Table 4.12 and conversion profile is plotted in Figure 4.18. Based on COD analysis, after 7 h of UV radiation, more than 40% of organics in POME has been converted. Based on Figure 4.18, most of the organics conversion occurred during the 1st hour reaction. After that, the reaction progressively slowed down and finally 40% of conversion achieved after 7 h of UV radiation. This could be explained by the deactivation of catalyst due to solid organic deposition on the catalyst surface after the organics decomposition.

Table 4.12 Results obtained for longevity photoreaction.

t (h)	COD (ppm)
0	247
1	177
2	165
3	156
4	152
5	144
6	141
7	139

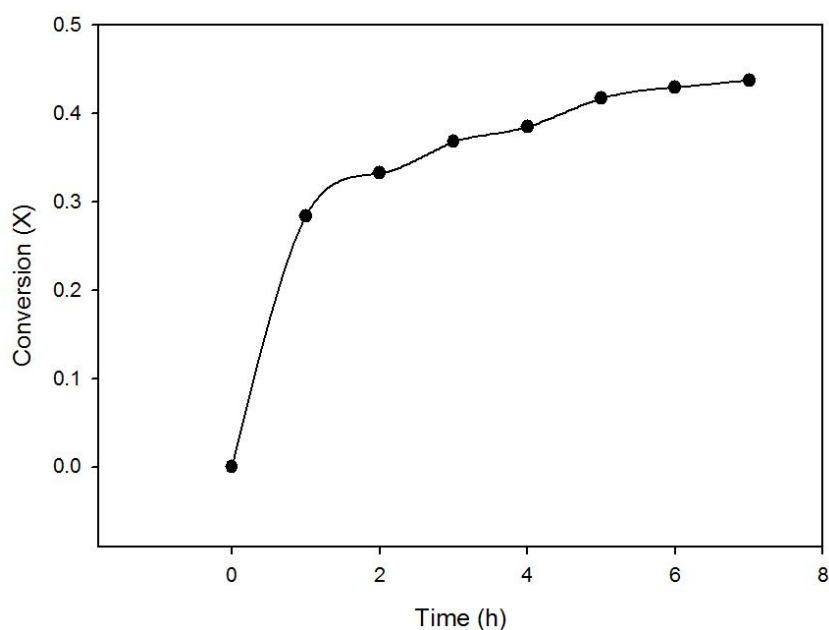


Figure 4.18 The conversion profile of organics in POME.

4.4 Gases Products

Another run of photoreaction was conducted in order to collect and analyse the gas products produced from the reaction. The reactor setting is shown in Figure 4.19.



Figure 4.19 Photoreaction setup to collect gases products.

Before the reaction, N_2 gas was flushed into the reactor from the left manifold (red-circled, left) for 30 min to fully remove residue air trapped initially in the reactor. Subsequently, during the reaction, N_2 -flow was stopped and sampling bag was immediately attached to the right opening of the reactor (red-circled, right) to collect the gaseous products. After 1 h of reaction time, the N_2 -flow was metered again to flush the produced gaseous products into the sampling bag. This gas was then analysed by gas chromatography (GC) equipped with TCD and Haysep DB packed-bed column.

The results obtained shows in Figure 4.20. From Figure 4.20, it can be seen that CO and CO_2 were detected as the primary gaseous products. The areas obtained were 3.8 and 214.1 for CO and CO_2 respectively. The ratio of CO_2/CO produced was 56.0, which indicates that the organics in POME have higher tendency to decompose into a more stable CO_2 species rather than the more reactive CO.

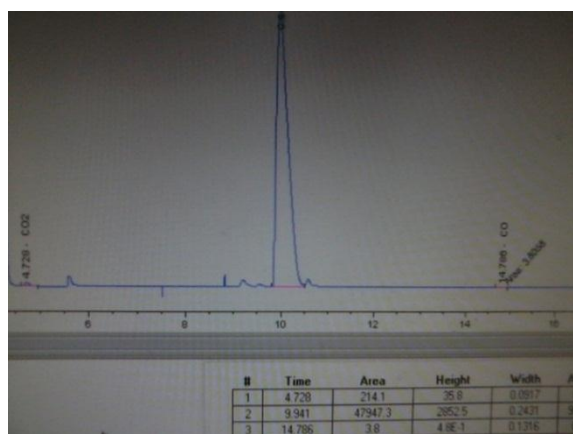


Figure 4.20 The gas chromatogram of gases produced.

4.5 Mechanisms of POME Decomposition

Based on the results obtained in Section 4.4, the mechanisms of POME decomposition is expected to occur according to the steps shown in Table 4.13. $C_aH_bO_c$ represents the organics in the POME while $C_dH_eO_f$ is fragment of organics formed after big organics decomposed.

Table 4.13 Mechanisms of POME decomposition.

Excitation	Cu/TiO_2	\rightarrow	$e^- + h^+$	
Adsorption	$O^{2-} + Ti^{IV} + H_2O$	\leftrightarrow	$OH^- + Ti^{IV}-OH^-$	
	$Ti^{IV} + H_2O$	\leftrightarrow	$Ti^{IV}-H_2O$	
	Site + $C_aH_bO_c$	\leftrightarrow	$C_aH_bO_{c, ads}$	
	$OH^\bullet + Ti^{IV}$	\leftrightarrow	$Ti^{IV} \setminus OH$	
Trapping	$Ti^{IV}-OH^- + h^+$	\leftrightarrow	$Ti^{IV} \setminus OH$	
	$Ti^{IV}-H_2O + h^+$	\leftrightarrow	$Ti^{IV} \setminus OH + H^+$	
	$C_aH_bO_{c, ads} + h^+$	\leftrightarrow	$R_{1, ads}^+$	
	$Ti^{IV} + e^-$	\leftrightarrow	Ti^{III}	
	$Ti^{III} + O_2$	\leftrightarrow	$Ti^{IV}-O_2^-$	
Hydroxyl Attack	Case I	$Ti^{IV} \setminus OH + C_aH_bO_{c, ads}$	\leftrightarrow	$Ti^{IV} + CO + CO_2 + H_2O$
	Case II	$OH^\bullet + C_aH_bO_{c, ads}$	\leftrightarrow	$C_dH_eO_{f, ads}$
	Case III	$Ti^{IV} \setminus OH + C_aH_bO_c$	\leftrightarrow	$Ti^{IV} + C_dH_eO_f$
	Case IV	$OH^\bullet + C_aH_bO_c$	\leftrightarrow	$C_dH_eO_f$
Reactions of other radicals		$e^- + Ti^{IV}-O_2^- + 2(H^+)$	\leftrightarrow	$Ti^{IV}(H_2O_2)$
		$Ti^{IV}-O_2^- + (H^+)$	\leftrightarrow	$Ti^{IV}(HO_2^\bullet)$
		$(H_2O_2) + (OH^\bullet)$	\leftrightarrow	$(HO_2^\bullet) + (H_2O)$

CHAPTER 5

CONCLUSIONS AND RECOMMENDATIONS

5.1 Conclusions

In this thesis, a new treating method for POME via photocatalysis was introduced employing Cu/TiO₂ with various formulations. Gas pycnometer measurements gave actual density of synthesized catalysts ranged from 2.76 to 3.29 g/cm³, which were much lower than theoretical density calculations, 4.20 to 4.80 g/cm³. This can be attributed to the porous structure of the catalyst. In terms of crystallography study, peaks synonymous with CuO species were recorded at $2\theta = 36.7^\circ$ for both 20wt% and 25wt% Cu/TiO₂ specimens respectively. For other catalysts, the same peak was undetected probably due to the machine's detection threshold. In addition, with exception to the 2wt% Cu/TiO₂, Cu species was discovered at $2\theta = 12.9^\circ$. The intensity of these Cu peaks increased with the Cu content in the catalysts. Following the XRF analysis, it can be concluded that the actual compositions of catalysts were considerably consistent with the intended recipes. From the liquid N₂ physisorption analysis, the catalysts were found to be porous, which is consistent with the discrepancy in the density comparison. Significantly, the BET specific surface area of these catalysts decreased with the wt% of Cu present in the catalysts due to formation of crystallite that has blocked the existing tunnels. Moreover, the pore volume and pore diameter of the catalysts were also determined from the same analysis. Based on the results, all of the catalysts can be categorized under mesoporous material as the measured pore size were ranged from 13.80 to 23.40 nm. In addition, 5wt% Cu/TiO₂ has the largest volume (both adsorption and desorption volume) at 0.050 cm³/g whilst 20wt% Cu/TiO₂ catalyst has largest adsorption pore and second largest desorption pore, viz. 23.39 nm and 19.76 nm respectively. From TGA analysis obtained from temperature-programmed calcination, a peak was observed at around 500 K for all the catalysts except 2wt% of Cu/TiO₂. The observed peak represents the thermal

decomposition of copper nitrate to CuO. Significantly, for 2wt% Cu/TiO₂, the aforementioned decomposition may not be visible from the non-isothermal heating probably due to the low copper nitrate composition. This was also consistent with XRD's findings.

The prepared catalysts were mixed in the pre-treated POME samples and were allowed to undergo photoreaction under radiation of 1000 W UV-light. Based on the screening results, 20wt% Cu/TiO₂ seems to give the highest conversion. Overall, a 27% conversion was achieved within 1 h. Employing the integral method, the decomposition of organic in the POME sample was found to adhere to the second-order for all the tested catalysts. Moreover, 20wt% Cu/TiO₂ also possessed the highest specific reaction constant at 2.6×10^{-5} , which indicates the highest reactivity among the catalysts. Significantly, the obtained results can be explained by the large size of adsorption and desorption pores of 20wt% Cu/TiO₂ which has allowed generous accessibility of organic reactant in POME to the active sites, consequently has enhanced the reactivity and the organics degradability. Therefore, compared to catalyst surface area and pore volume, pore size seems to have higher effects on the reactivity of catalysts.

Besides that, the catalyst loading in the sample were also determined by running photoreaction with different loading of 20 wt% Cu/TiO₂. An optimum point was discovered at 0.83 g of catalyst/L of POME. Generally, high catalyst loading yielded to higher conversion. However, catalyst loading that higher than 0.83 inhibits the penetration of UV light into the slurry mixture and reduce the organics conversion. After that, longevity photoreaction was conducted for 7 h. Based on the results, most organics decomposed at the 1st hour of reaction while comparative small organics decompositions were observed for the remaining hours. This indicates the deactivation of catalyst occurred due to solid organic deposition on the catalyst surface after the organics decomposition.. However, a conversion more than 40% was achieved after 7 h of photoreaction. Moreover, gaseous products were collected for analysis purpose by using GC. CO and CO₂ were detected in the gas products. High CO₂/CO ratio indicates high tendency of organics in POME decompose into CO₂ compared to CO.

As a conclusion, the current research has shown that POME waste can be treated via photoreaction in the presence of Cu/TiO₂ catalyst. By using this new proposed method, the retention time for POME treatment can be significantly decreased from 20 days of hydraulic retention time to within hours. Moreover, the large land area requirement for the traditional treatment method can also be reduced by replacing the traditional treatment method with this new developed phototreatment method. Finally, phototreatment process can be accomplished with very low expenses as solar energy from the sun is a continuous and readily available power supply for photocatalysis as the activator needed for this process is visible light or UV radiation.

5.2 Recommendations

Based on the findings and observations of this research projects, the following suggestions are proposed for future studies. Firstly, during photocatalysts preparation, suitable methods and parameters must be employed to improve the reactivity of catalysts. For current study, the catalysts were prepared by using wet impregnation method and air-calcined at 673 K for 30 min. Further study may be required to find the suitable methods and parameters for better catalysts. During conducting reaction, proper personal protective equipments are necessary as UV light is employed. UV light is hazardous and long term health effects will be occurred towards human if overexposed. Besides, the operating temperature has to be maintained throughout the experiment for more accurate results. UV light will emit high amount of heat energy causing the operating temperature increasing along the experiment. Proper cooling steps must be taken to maintain the temperature. Finally, during COD analysis, the digested vial must not be shaken as the resuspension of sediment will interrupt the COD readings.

REFERENCES

- Abdurahman, N. H., Rosli, Y.M., Azhari, N. H., & Tam, S. F. (2011). Biomethanation of Palm Oil Mill Effluent (POME) by Membrane Anaerobic System (MAS) using POME as a Substrate. *World Academy of Science, Engineering and Technology*, 51, 419-424.
- Abdurahman, N. H., Rosli, Y. M., & Azhari, N. H. (2011). Development of a membrane anaerobic system (MAS) for palm oil mill effluent (POME) treatment. *Desalination*, 266(1-3), 208-212.
- Abdurahman, N. H., Rosli, Y. M., & Azhari, N. H. (2013). The performanc evaluation of anaerobic methods for palm oil mill effluent (POME) treatment: A review. *International Perspectives on Water Quality Management and Pollutant Control*, 88-104.
- Ahmad A.L., Ismail, S., & Bhatia, S. (2003). Water recycling from palm oil mill effluent (POME) using membrane technology. *Desalination*, 157, 87-95.
- Ahmad A.L., Ismail, S., & Bhatia, S. (2005). Membrane treatment for palm oil mill effluent: effect of transmembrane pressure and crossflow velocity. *Desalination*, 179, 245-255.
- Ahmad A.L., Ismail, S., & Bhatia, S. (2005). Ultrafiltration behavior in the treatment of agro-industry effluent: pilot scale studies. *Chem Eng Sci*, 60, 5385-5394.
- Ahmad A.L., Chong, M.F., Ismail, S., & Bhatia, S. (2006). Drinking water reclamation from palm oil mill effluent (POME) using membrane technology. *Desalination* , 191, 35-44.
- Al-Rasheed, R. A. (2005). Water treatment by heterogeneous photocatalysis an overview. Saudi Arabia: Saline Water Desalination Research Institute.
- Amadelli, R., Molinari, A., Vitali, I., Samiolo, L., Mura, G. M., & Maldotti, A. (2005). Photoelectro-chemical properties of TiO₂ mediated by the enzyme glucose oxidase. *Catal. Today*, 101(3-4), 397-405.
- America Palm Oil Council. (2003). Sustainable Palm Oil Practices: Palm oil mill effluent (POME) and empty fruit bunch application as a nutrient source in oil palm. Retrieved from <http://www.americanpalmoil.com/sustainable-nutrient.html> on 5th March 2013.
- Anderson, J.R. & Pratt, K.C.(1985). *Introduction to characterization and testing of catalyst*. Sydney: Academic Press.
- Anon. (1995). Biogas plants treating palm oil mill effluent in Malaysia. Rapa: Rural Energy.

- Atif, A. A. Y., Fakhru'l-Razi, A., Ngan, M. A., Morimoto, M., Iyuke, S. E., & Veziroglud, N. T. (2005). Fed batch production of hydrogen from palm oil mill effluent using anaerobic microflora. *Int. J. Hydrogen Energ.*, 30, 1393-1397.
- Azaroff, L.V. (1968). *Elements of x-Ray crystallography*. New York: McGraw Hill Book Company.
- Bahnemann D. (2004). Photocatalytic Water Treatment: Solar Energy Applications. *Sol Energy*, 77, 445-459.
- Banerjee, D. & Nesbitt, H. W. (1999). XPS study of reductive dissolution of birnessite by oxalate: rates and mechanistic aspects of dissolution and redox processes. *Geochim Cosmochim Acta*, 63(19-20), 3025–3038.
- Barrett, E.P., Joyner, L.G., & Halenda, P.P. (1951). The determination of pore volume and area distributions in porous substances. I. Computations from nitrogen isotherms. *J Amer Chem Soc*, 73, 373-380.
- Bayne, L., Ulijn, R. V., & Halling, P. J. (2013). Effect of pore size on the performance of immobilised enzymes. *Chem Soc Rev*(23), 42, 9000-9010.
- Bennett, S. W. & Keller, A. A. (2011). Comparative photoactivity of CeO₂, γ-Fe₂O₃, TiO₂ and ZnO in various aqueous systems. *Appl Catal B-Environ*, 102(3-4), 600-607.
- Bergeret, G. & Gallezot, P. (1997). Particle size and dispersion measurements, In: Ertl, G., Nözinger, H. & Weitkamp, J (Eds.). *Handbook of Heterogeneous Catalysis*. Weinheim.
- Bergeret, G. & Gallezot, P. (1973). *Particle size and dispersion measurements*, in *Handbook of heterogeneous catalysis*. VCH Verlagsgesellschaft mbH: Weinheim.
- Borja, R., Banks, C. J., Martin, A., & Khalfoui, B. (1995). Anaerobic digestion of palm oil mill effluent and condensation water waste: an overall kinetic model for methane production and substrate utilization. *Bioprocess Eng*, 13, 87-95.
- Borkris, J. O. M. (1973). A hydrogen economy. *Science*, 178, 1323.
- Brunauer, S., Emmett, P.H., & Teller E. (1938). Adsorption of gases in multimolecular layers. *J Amer Chem Soc*, 60, 309-319.
- Cail, R. G. & Barford, J. P. (1985). Mesophilic semi-continuous anaerobic digestion of palm oil mill effluent. *Biomass*, 7, 287-295.
- Carey, J. H., Lawrence, J., & Tosine, H. M. (1976). Photodechlorination of PCB's in the presence of titanium dioxide in aqueous suspensions. *Bull Environ Contam Toxicol*, 16; 697-701.

- Carvalho, H. W. P., Batista, A. P. L., Hammer, P., & Ramalho, T. (2010). Photocatalytic degradation of methylene blue by TiO₂-Cu thin films: Theoretical and experimental study. *J Hazard Mater*, 184(1-3), 273-280.
- Ceram Research Limited. (2000). Titanium Dioxide - Titania (TiO₂). Retrieved from <http://www.azom.com/properties.aspx?ArticleID=1179> on 5th March 2013.
- Chan, Y. J., Chong, M. F., Law, C. L., & Hassell, D. G. (2009). A review on anaerobic-aerobic treatment of industrial and municipal wastewater. *Chem. Eng. J.*, 155, 1-18.
- Chen, H., Ku, Y., & Kou, Y. (2007). Effect of Pt/TiO₂ characteristics on temporal behavior of *o*-cresol decomposition by visible light-induced photocatalysis. *Water Res*, 41(10), 2069-2078.
- Chin, K. K., Lee, S. W., & H.H. Mohammad, H. H. (1996). A study of palm oil mill effluent treatment using a pond system. *Water. S.C.I. Technol.*, 34(11), 119-123.
- Chin, K. K. & Wong, K. K. (1983). Thermophilic anaerobic digestion of palm oil mill effluent. *Water Res*, 17, 993-995.
- Chong, M. L., Rahim, R. A., Shirai, Y., & Hassan, M. A. (2009). Biohydrogen production by *Clostridium butyricum* EB6 from palm oil mill effluent. *Int J Hydrogen Energ*, 34(2), 764-771.
- Clescerl, S. L., Greenberg, A. E., & Eaton, A. D. (1999). *Standard Methods for Examination of Water & Wastewater* (20th ed.). Washington, DC: American Public Health Association.
- Cui, L., Wang, Y., Niu, M., Chen, G., & Cheng, Y. (2009). Synthesis and visible light photocatalysis of Fe-doped TiO₂mesoporous layers deposited on hollow glass microbeads. *J Solid State Chem*, 182(10), 2785-2790.
- Cullity, B.D. (2001). *Elements of x-ray diffraction*. London: Prentice-Hall International.
- De_Boer, J.H., Lippens, B. C., Linsen, B. G., Broekhoff, J. C. P., van den Heuvel, A., & Osinga, Th J. (1966). Thet-curve of multimolecular N₂-adsorption. *J Colloid Interf Sci*, 21(4), 405-414.
- de_Richter, R. & Caillol, S. (2011). Fighting global warming: The potential of photocatalysis against CO₂, CH₄, N₂O, CFCs, tropospheric O₃, BC and other major contributors to climate change. *J. Photoch. Photobio.C.*, 12(1), 1-19.

- Doble, M., & Kumar, A. (2005). Biotreatment of industrial effluents. United Kingdom, UK: Butterworth – Heinemann.
- Dollimore, D., & Heal, G.R. (1964). An improved method for the calculation of pore-size distribution from adsorption data. *J Appl Chem*, 14, 109-114.
- Edewor, J.O. (1986). A comparison of treatment methods for palm oil mill effluent (POME) wastes. *J Chem Technol Biotechnol*, 36, 212-218.
- Fakhru'l-Razi, A. & Noor, M.J.M.M. (1999). Treatment of palm oil mill effluent (POME) with the membrane anaerobic system (MAS). *Water Sci. Technol*, 39, 159-163.
- Faisal, M. & Unno, H. (2001). Kinetic analysis of palm oil mill wastewater treatment by a modified anaerobic baffled reactor. *Biochem Eng J*, 9, 25-31.
- Farbod, M. & Kajbafvala, M. (2013). Effect of nanoparticles surface modification on the adsorption-enhanced photocatalysis of Gd/TiO₂ nanocomposite. *Powder Technol*, 239, 434-440.
- Fenoll, J., Hellin, P., Martinez, C. M., Flores, P., & Navarro, S. (2012). Semiconductor-sensitized photodegradation of *s*-triazine and chloroacetanilide herbicides in leaching water using TiO₂ and ZnO as catalyst under natural sunlight. *J Photoch Photobio A*, 238, 81-87.
- Fitton, G. (1997). Modern Analytical Geochemistry: An Introduction to Quantitative Chemical Analysis for Earth, Environmental and Material Scientists. UK: Addison Wesley Longman.
- Fox ,M.A. & Dulay, M.T. (1993), Heterogeneous photocatalysis. *Chem Rev*, 93, 341-357.
- Fujishima, A., Ohko, Y., Nakashima, T., & Kubota, Y. (n.d.). TiO₂ photocatalysis for water treatment.
- Fujishima, A., Rao, T. N., & Tryk, D. A. (2000). Titanium dioxide photocatalysis. *J.Photoch. Photobio. A.*, 1, 1-21.
- Gregg, S.J., and Sing, K. S. W. (1982). *Adsorption, Surface Area, and Porosity*. 2 nd ed. London: Academic Press.
- Hernández-Alonso, M. D., Hungría, A. B., Martínez-Arias, A., Fernández-García, M., Coronado, J.M., Conesa, J. C., & Soria, J. (2004). EPR study of the photoassisted formation of radicals on CeO₂ nanoparticles employed for toluene photooxidation. *Appl Catal B-Environ*, 50(3), 167-175.
- Ho, C. C. & Tan, Y. K. (1988). The treatment of anaerobically digested palm oil mill effluent by pressurized activated sludge. *J Chem Technol Biotechnol*, 41, 75-84.

- Kamal, S. A., Jahim, J. M., Anuar, N., Hassan, O., Daud, W. R. W., Mansor, M. F., & Rashid, S. S. (2012). Pre-Treatment Effect of Palm Oil Mill Effluent (POME) during Hydrogen Production by a Local Isolate *Clostridium butyricum*. *Int J Adv Science, Engineering and Information Technology*, 2, 54-60.
- Karim, M. I. A. & Kamil, A. Q. A. (1989). Biological treatment of palm oil mill effluent using *Trichoderma viride*. *Biol Wastes*, 27, 143-152.
- Karunakaran, C. & Senthilvelan, S. (2006). Fe₂O₃-photocatalysis with sunlight and UV light: Oxidation of aniline. *Electrochem Commun*, 8(1), 95-101.
- Klug, H.P. & Alexander, L.E. (1974). X-ray Diffraction Procedures for Polycrystalline and Amorphous Materials. New York: Wiley.
- Kondarides, D. I. (n.d.). Photocatalysis. *Catalysis*.
- Kwon, K. D., Refson, K., & Sposito, G. (2009). On the role of Mn(IV) vacancies in the photoreductive dissolution of hexagonal birnessite. *Geochim Cosmochim Acta*, 73(14), 4142–4150.
- Lam, M. K. & Lee, K.T. (2011). Renewable and sustainable bioenergies production from palm oil mill effluent (POME): Win–win strategies toward better environmental protection. *Biotechnol Adv*, 29, 124-141.
- Langmuir, I. (1916). The constitution and fundamental properties of solids and liquids. *J Amer Chem Soc*, 38, 2221-2267.
- Lake, B.G. (1999). Coumarin Metabolism, Toxicity and Carcinogenicity: Relevance for Human Risk Assessment. *Food Chem Toxicol*, 37(4), 423-453.
- Lasa, D. H., Serrano, B., & Salaices, M. (2005). Photocatalytic Reaction Engineering. United States, US: Library of Congress.
- Lee, D. (2012). Toward the clean production of hydrogen: Competition among renewable energy sources and nuclear power. *Int J Hydrogen Energ*, 34(10), 1652-1661.
- Liao, S., Donggen, H., Yu, D., Su., & Yuan, G. (2004). Preparation and characterization of ZnO/TiO₂, SO₄²⁻/ZnO/TiO₂ photocatalyst and their photocatalysis. *J Photoch Photobio A*, 168(1-2), 7-13.
- Liebhaufsky, H.A., Peiffer, H.G., Winslow, E.H., & Zeman, P.D. (1972). *X-ray electrons and analytical chemistry*. New York: Wiley-Interscience, John Wiley & Sons Inc.
- Lim, T. K., Gan, L. T., Ooi, L. H., & Tandinata, H. (2012). Establishing biogas plants

to process palm oil mill effluent. Retrieved from <http://www.sustainablepalmoil.org/growers-millers/millers/case-studies/musim-mas-2/> on 5th February 2013.

Linsebigler, Amy, L., Lu, G., & Yates, J. T. (1995). Photocatalysis on TiO₂ surfaces: Principles, mechanisms, and selected results. *Chem. Rev.*, 95, 735-758.

Lin, Y. & Lee H. (2010). Effects of TiO₂ coating dosage and operational parameters on a TiO₂/Ag photocatalysis system for decolorizing Procion red MX-5B. *J Hazard Mater*, 179(1-3), 462-470.

Liu, S., Lou, S., Kuang, C., Huang, W., Chen, W., Zhang, J., & Zhong, G. (2011). Water quality assessment by pollution-index method in the coastal waters of Hebei Province in western Bohai Sea, China. *Mar. Pollut. Bull.*, 62, 2220-2229.

Liu, W., Zeng, F., Jiang, H., Zhang, X., & Li, W. (2012). Composite Fe₂O₃ and ZrO₂/Al₂O₃ photocatalyst: Preparation, characterization, and studies on the photocatalytic activity and chemical stability. *Chem Eng J*, 180, 9-18.

Ma, A. N., Cheah, S. C., & Chow, M. C. (1993). Current status of palm oil mill processing wastes management. *Waste Management in Malaysia: Current status and prospects for bioremediation*. 111-136.

Ma, A. N. & Ong, A. S. H. (1986). Palm oil processing e new development in effluent treatment. *Water Sci Technol*, 18, 35-40.

Meng, Z. & Juan, Z. (2008). Wastewater treatment by photocatalytic oxidation of Nano-ZnO. *Global Environmental Policy in Japan*, 12, 1-9.

Montgomery, D. C. (1997). *Design and Analysis of Experiment*. New York: John Wiley & Sons Inc.

Michler, G.H. (2004). *Electron microscopy of polymers*. Berlin Heidelberg: Springer.

Oswal, N., Sarma, P. M., Zinjarde, S. S., & Pant, A. (2002). Palm oil mill effluent treatment by a tropical marine yeast. *Bioresour Technol*, 85, 35-37.

Palanisamy, B., Babu, C. N., Sundaravel, B., Anandan, S., & Murugesan, V. (2013). Sol-gel synthesis of mesoporous mixed Fe₂O₃/TiO₂ photocatalyst: Application for degradation of 4-chlorophenol. *J Hazard Mater*, 252-253, 233-242.

Pellin, M. J., Stair, P. C., Xiong, G., Elam, J. W., Birrell, J., Curtiss, L., George, S. M., Han, C. Y., Iton, L., Kung, H., Kung, M., & Wang, H. H. (2005). Mesoporous catalytic membranes: Synthetic control of pore size and wall composition. *Catalysis Letters*, 102, 127-130.

Puzyn, T., & Mostrag-Szlichtyng, A. (2012). Organic pollutants ten years after the stockholm convention - Environmental and analytical update. Croatia: Intech.

Qian, J., Chen, F., Wang, F., Zhao, X., & Chen, Z. (2012). Daylight photocatalysis performance of biomorphic CeO₂ hollow fibers prepared with lens cleaning paper as biotemplate. *Mater Res Bull*, 47(8), 1845-1848.

Raiz, N., Chong, F. K., Dutta, B. K., Man, Z. B., Khan, M. S., & Nurlaela, E. (2012). Photodegradation of Orange II under visible light using Cu–Ni/TiO₂: Effect of calcination temperature. *Chem Eng J*, 185-186, 108-119.

Ruoyu, H., Liping, X., Zhiqiang R. (2005). Nanosized Zinc Oxide Prepared by Homogenous of Precipitation and Its Photocatalytic Property. *Environmental Protection of Chemical Industry*, 25(3), 231-234.

Rouquerol, J., Rouquerol, F., Llewellyn, P., Maurin, G., & Sing, K. S. W. (2013). Adsorption by Powders and Porous Solids: Principles, Methodology and Applications. UK: Academic Press.

Sato, S. & White, J. M. (1980). Photodecomposition of water over Pt/TiO₂ catalysts. *Chem Phys Lett*, 72(1), 83-86.

Sawyer, C. N., McCarty, P. L., & Gene F. Parkin (2003). *Chemistry for Environmental Engineering and Science*(5th ed.). New York: McGraw-Hill.

Sclafani, A., Mozzanega, M. N., & Pichat, P. (1991). Effect of silver deposits on the photocatalytic activity of titanium dioxide samples for the dehydrogenation or oxidation of 2-propanol. *J Photochem Photobiol A: Chem*, 59, 181.

Shea, J. E. (1954). *U.S. Patent No. 2,667,782*. Washington, DC: U.S. Patent and Trademark Office.

Sime Darby Plantation. (2011). Palm oil mill effluent treatment system. Retrieved from [http://www.simedarbyplantation.com/Palm Oil Mill Effluent Treatment System.aspx](http://www.simedarbyplantation.com/Palm_Oil_Mill_Effluent_Treatment_System.aspx) on 5th February 2013.

Sing, K S. W., Everett, D. H., Haul, R. A. W., Moscou, L., Pierotti, R. A., Rouquerol, J., and Siemieniewska, T. (1985). Reporting Physisorption Data for Gas Solid Systems with Special Reference to the Determination of Surface-Area and Porosity (Recommendations 1984). *Pure Appl Chem*, 57(4), 603-619.

Sing, K. S. W. & Rouquerol, J. (1997). *Surface Area and Porosity*, in *Handbook of heterogeneous catalysis*, VCH Verlagsgesellschaft mbH: Weinheim.

Slamet, Nasution, H. W., Purnama, E., Kosela, S., & Gunlazuardi, J. (2006). Photocatalytic reduction of CO₂ on copper-doped Titania catalysts prepared by improved-impregnation method. *Catalysis Communications*, 6, 313-319.

Suib, S. L. (2008). Porous manganese oxide octahedral molecular sieves and octahedral layered materials. *Accounts Chem Res*, 41(4), 479–487.

- Tay, J. H. (1991). Complete reclamation of palm oil wastes. *Resour Conserv Recy* 5, 383-392.
- Tian, L., Zhao, Y., He, S., Wei, M., & Duan, X. (2012). Immobilized Cu–Cr layered double hydroxide films with visible-light responsive photocatalysis for organic pollutants. *Chem Eng J*, 184, 261-267.
- Turchi, C. S., & Ollis, D. F. (1990). Photocatalytic degradation of organic water contaminants: Mechanisms involving hydroxyl radical attack. *J Catal*, 122, 178-192.
- Ugoji, E.O. (1997). Anaerobic digestion of palm oil mill effluent and its utilization as fertilizer for environmental protection. *Renew Energy*, 10, 291-294.
- Vijayaraghavan, K., Ahmad, D., & Abdul Aziz, M. E. (2007). Aerobic treatment of palm oilmill effluent. *J Environ Manage*, 82, 24-31.
- Wang, X., He, Z., Zhong, S., & Xiao, X. (2007). Photocatalytic Synthesis of Hydrocarbon Oxygenates from C₂H₆ and CO₂ over Pd-MoO₃/SiO₂ Catalyst. *J Nat Gas Chem*, 16(2), 173-178.
- Warren, B. E. (1969). *X-ray Diffraction*. Reading: Addison-Wesley.
- Wu, N. & Lee, M. (2004). Enhanced TiO₂ photocatalysis by Cu in hydrogen production from aqueous methanol solution. *Int J Hydrogen Energ*, 29(15), 1601-1605.
- Wu, T. Y., Mohammad, A. W., Jahim, J. M., & Anuar, N. (2010). Pollution control technologies for the treatment of palm oil mill effluent (POME) through end-of-pipe processes. *J. Environ. Manage.*, 91, 1467-1490.
- Xia, H., Zhuang, H., Zhang, T., & Xiao, D. (2008). Visible-light-activated nanocomposite photocatalyst of Fe₂O₃/SnO₂. *Mater Lett*, 62(6-7), 1126-1128.
- Yacob, S., Hassan, M. A., Shirai, Y., Wakisaka, M., & Subash, S. (2006). Baseline study of methane emission from anaerobic ponds of palm oil mill effluent treatment. *Sci Total Environ*, 366, 187-196.
- Yoong, L. S., Chong, F. K., Dutta, B. K. (2009). Development of copper-doped TiO₂ photocatalyst for hydrogen production under visible light. *Energy*, 34(10), 1652-1661.
- Zafar, S. (2013). Properties and Uses of POME. Retrieved from: <http://www.bioenergyconsult.com/tag/properties-of-pome/> on 7th May 2013.
- Zhang, Q., Cheng, X., Zheng, C., Feng, X., Qiu, G., Tan, W., & Liu, F. (2011). Roles of manganese oxides in degradation of phenol under UV-Vis irradiation: Adsorption, oxidation, and photocatalysis. *J. Environ. Sci.*, 23(11), 1904-1910.

Zhang, X. & Lei, L. (2008). Preparation of photocatalytic Fe₂O₃-TiO₂ coatings in one step by metal organic chemical vapor deposition. *Appl Surf Sci*, 254(8), 2406-2412.

APPENDICES

Appendix A Calculations for Catalyst Preparation

40g of each sample will be prepared. The calculations below will be used to obtain mass of TiO_2 and $\text{Cu}(\text{NO}_3)_2 \cdot 3\text{H}_2\text{O}$ needed for the particular composition for the catalysts.

- 1) Determine the mass of TiO_2 and Cu contained in the particular catalyst.

$$M_{\text{TiO}_2} = (1-Y) \cdot 40$$

$$M_{\text{Cu}} = (Y) \cdot 40$$

Where Y is the wt% of Cu composition.

- 2) Determine the mass of $\text{Cu}(\text{NO}_3)_2 \cdot 3\text{H}_2\text{O}$ needed.

$$\begin{aligned} M_{\text{Cu}(\text{NO}_3)_2 \cdot 3\text{H}_2\text{O}} &= M_{\text{Cu}} * (\text{Mr}_{\text{Cu}(\text{NO}_3)_2 \cdot 3\text{H}_2\text{O}} / \text{Mr}_{\text{Cu}}) \\ &= M_{\text{Cu}} * (241.6 / 63.5) \end{aligned}$$

Where Mr is molar mass and M_{Cu} is the answer obtained from step (1).

Thus, to obtain the desired composition catalyst, mass of TiO_2 obtained from step (1) is needed to mix with the mass of $\text{Cu}(\text{NO}_3)_2 \cdot 3\text{H}_2\text{O}$ from step (2).

Example: 2wt% Cu/ TiO_2

- 1) Determine the mass of TiO_2 and Cu contained in the particular catalyst.

$$M_{\text{TiO}_2} = (1-Y) \cdot 40$$

$$= (1-0.02) \cdot 40$$

$$= 39.2\text{g}$$

$$\begin{aligned}M_{\text{Cu}} &= (Y)*40 \\ &= 0.02*40 \\ &= 0.8\text{g}\end{aligned}$$

2) Determine the mass of $\text{Cu}(\text{NO}_3)_2 \cdot 3\text{H}_2\text{O}$ needed.

$$\begin{aligned}M_{\text{Cu}(\text{NO}_3)_2 \cdot 3\text{H}_2\text{O}} &= M_{\text{Cu}} * (M_{\text{rCu}(\text{NO}_3)_2 \cdot 3\text{H}_2\text{O}} / M_{\text{rCu}}) \\ &= 0.8*(241.6/63.5) \\ &= 3.0438\text{g}\end{aligned}$$

Thus, in order to obtain 2wt% of Cu/TiO_2 , the TiO_2 and $\text{Cu}(\text{NO}_3)_2 \cdot 3\text{H}_2\text{O}$ needed are 39.2g and 3.0438g respectively.

Appendix B XRF Results

CENLAB/F/007



CENTRAL LABORATORY
Universiti Malaysia Pahang, Lebuhraya Tun Razak,
26300 Kuantan, Pahang Darul Makmur.
Tel: 09-5493344/8097 Fax: 09-5493353
E-mail: ucl@ump.edu.my

CERTIFICATE OF ANALYSIS (COA)

To :	NG KIM HOONG	Attn :	
Address :	FKKSA, UMP		
c.c. :		Page :	5 pages
Fax No :	Tel No : 016-5901865	Sample Lab No: 2013/228	

Sample description : Six samples in powdered form

Sample marking : Cu/TiO₂

Date of sample received : 09/05/2013

Date reported : 13/05/2013

RESULTS:

Sample 1: 2wt %

No	Parameter	Results	Unit	Test Method
1.	Titanium Oxide (TiO ₂)	92.79	%	Quantexpress (Best Detection)
2.	Copper Oxide (CuO)	2.45	%	Quantexpress (Best Detection)
3.	Phosphorus Pentoxide (P ₂ O ₅)	0.43	%	Quantexpress (Best Detection)
4.	Silicon Dioxide (SiO ₂)	0.25	%	Quantexpress (Best Detection)
5.	Aluminium Oxide (Al ₂ O ₃)	0.20	%	Quantexpress (Best Detection)
6.	Potassium Oxide (K ₂ O)	0.06	%	Quantexpress (Best Detection)
7.	Neobium Oxide (Nb ₂ O ₅)	0.03	%	Quantexpress (Best Detection)
8.	Sulphur Trioxide (SO ₃)	0.03	%	Quantexpress (Best Detection)
9.	Zirconium Oxide (ZrO ₂)	0.02	%	Quantexpress (Best Detection)
10.	Iron Oxide (Fe ₂ O ₃)	0.01	%	Quantexpress (Best Detection)

11.	Calcium Oxide (CaO)	95	ppm	Quantexpress (Best Detection)
12.	Nickel Oxide (NiO)	35	ppm	Quantexpress (Best Detection)

Sample 2: 5wt %

No	Parameter	Results	Unit	Test Method
1.	Titanium Oxide (TiO ₂)	88.78	%	Quantexpress (Best Detection)
2.	Copper Oxide (CuO)	5.65	%	Quantexpress (Best Detection)
3.	Phosphorus Pentoxide (P ₂ O ₅)	0.44	%	Quantexpress (Best Detection)
4.	Silicon Dioxide (SiO ₂)	0.24	%	Quantexpress (Best Detection)
5.	Aluminium Oxide (Al ₂ O ₃)	0.21	%	Quantexpress (Best Detection)
6.	Potassium Oxide (K ₂ O)	0.05	%	Quantexpress (Best Detection)
7.	Neobium Oxide (Nb ₂ O ₅)	0.03	%	Quantexpress (Best Detection)
8.	Sulphur Trioxide (SO ₃)	0.02	%	Quantexpress (Best Detection)
9.	Zirconium Oxide (ZrO ₂)	0.02	%	Quantexpress (Best Detection)
10.	Chlorine (Cl)	0.01	%	Quantexpress (Best Detection)
11.	Calcium Oxide (CaO)	93	ppm	Quantexpress (Best Detection)
12.	Iron Oxide (Fe ₂ O ₃)	77	ppm	Quantexpress (Best Detection)
13.	Zinc Oxide (ZnO)	72	ppm	Quantexpress (Best Detection)
14.	Nickel Oxide (NiO)	38	ppm	Quantexpress (Best Detection)

Sample 3: 10wt %

No	Parameter	Results	Unit	Test Method
1.	Titanium Oxide (TiO ₂)	83.02	%	Quantexpress (Best Detection)
2.	Copper Oxide (CuO)	11.29	%	Quantexpress (Best Detection)
3.	Phosphorus Pentoxide (P ₂ O ₅)	0.39	%	Quantexpress (Best Detection)

4.	Silicon Dioxide (SiO ₂)	0.21	%	Quantexpress (Best Detection)
5.	Aluminium Oxide (Al ₂ O ₃)	0.20	%	Quantexpress (Best Detection)
6.	Potassium Oxide (K ₂ O)	0.05	%	Quantexpress (Best Detection)
7.	Neobium Oxide (Nb ₂ O ₅)	0.03	%	Quantexpress (Best Detection)
8.	Sulphur Trioxide (SO ₃)	0.02	%	Quantexpress (Best Detection)
9.	Zirconium Oxide (ZrO ₂)	0.01	%	Quantexpress (Best Detection)
10.	Chlorine (Cl)	0.01	%	Quantexpress (Best Detection)
11.	Iron Oxide (Fe ₂ O ₃)	0.01	%	Quantexpress (Best Detection)
12.	Calcium Oxide (CaO)	85	ppm	Quantexpress (Best Detection)
13.	Nickel Oxide (NiO)	45	ppm	Quantexpress (Best Detection)
14.	Molibdenum Trioxide (MoO ₃)	33	ppm	Quantexpress (Best Detection)
15.	Hafnium Oxide (HfO ₂)	14	ppm	Quantexpress (Best Detection)

Sample 4: 15wt %

No	Parameter	Results	Unit	Test Method
1.	Titanium Oxide (TiO ₂)	76.77	%	Quantexpress (Best Detection)
2.	Copper Oxide (CuO)	17.97	%	Quantexpress (Best Detection)
3.	Phosphorus Pentoxide (P ₂ O ₅)	0.35	%	Quantexpress (Best Detection)
4.	Silicon Dioxide (SiO ₂)	0.21	%	Quantexpress (Best Detection)
5.	Aluminium Oxide (Al ₂ O ₃)	0.17	%	Quantexpress (Best Detection)
6.	Potassium Oxide (K ₂ O)	0.05	%	Quantexpress (Best Detection)
7.	Neobium Oxide (Nb ₂ O ₅)	0.03	%	Quantexpress (Best Detection)
8.	Zinc Oxide (ZnO)	0.02	%	Quantexpress (Best Detection)
9.	Zirconium Oxide (ZrO ₂)	0.02	%	Quantexpress (Best Detection)
10.	Sulphur Trioxide (SO ₃)	0.02	%	Quantexpress (Best Detection)

11.	Calcium Oxide (CaO)	0.01	%	Quantexpress (Best Detection)
12.	Chlorine (Cl)	0.01	%	Quantexpress (Best Detection)
13.	Iron Oxide (Fe ₂ O ₃)	87	ppm	Quantexpress (Best Detection)

Sample 5: 20wt %

No	Parameter	Results	Unit	Test Method
1.	Titanium Oxide (TiO ₂)	70.23	%	Quantexpress (Best Detection)
2.	Copper Oxide (CuO)	22.88	%	Quantexpress (Best Detection)
3.	Phosphorus Pentoxide (P ₂ O ₅)	0.31	%	Quantexpress (Best Detection)
4.	Silicon Dioxide (SiO ₂)	0.20	%	Quantexpress (Best Detection)
5.	Aluminium Oxide (Al ₂ O ₃)	0.17	%	Quantexpress (Best Detection)
6.	Potassium Oxide (K ₂ O)	0.04	%	Quantexpress (Best Detection)
7.	Neobium Oxide (Nb ₂ O ₅)	0.03	%	Quantexpress (Best Detection)
8.	Chlorine (Cl)	0.02	%	Quantexpress (Best Detection)
9.	Sulphur Trioxide (SO ₃)	0.02	%	Quantexpress (Best Detection)
10.	Zirconium Oxide (ZrO ₂)	0.01	%	Quantexpress (Best Detection)
11.	Iron Oxide (Fe ₂ O ₃)	88	ppm	Quantexpress (Best Detection)
12.	Nickel Oxide (NiO)	60	ppm	Quantexpress (Best Detection)
13.	Calcium Oxide (CaO)	55	ppm	Quantexpress (Best Detection)

Sample 6: 25wt %

No	Parameter	Results	Unit	Test Method
1.	Titanium Oxide (TiO ₂)	62.86	%	Quantexpress (Best Detection)
2.	Copper Oxide (CuO)	27.77	%	Quantexpress (Best Detection)
3.	Phosphorus Pentoxide (P ₂ O ₅)	0.27	%	Quantexpress (Best Detection)

4.	Silicon Dioxide (SiO ₂)	0.15	%	Quantexpress (Best Detection)
5.	Aluminium Oxide (Al ₂ O ₃)	0.14	%	Quantexpress (Best Detection)
6.	Potassium Oxide (K ₂ O)	0.04	%	Quantexpress (Best Detection)
7.	Iron Oxide (Fe ₂ O ₃)	0.03	%	Quantexpress (Best Detection)
8.	Neobium Oxide (Nb ₂ O ₅)	0.02	%	Quantexpress (Best Detection)
9.	Sulphur Trioxide (SO ₃)	0.02	%	Quantexpress (Best Detection)
10.	Calcium Oxide (CaO)	0.02	%	Quantexpress (Best Detection)
11.	Chlorine (Cl)	0.01	%	Quantexpress (Best Detection)
12.	Zirconium Oxide (ZrO ₂)	0.01	%	Quantexpress (Best Detection)
13.	Chromium Oxide (Cr ₂ O ₃)	0.01	%	Quantexpress (Best Detection)
14.	Nickel Oxide (NiO)	80	ppm	Quantexpress (Best Detection)

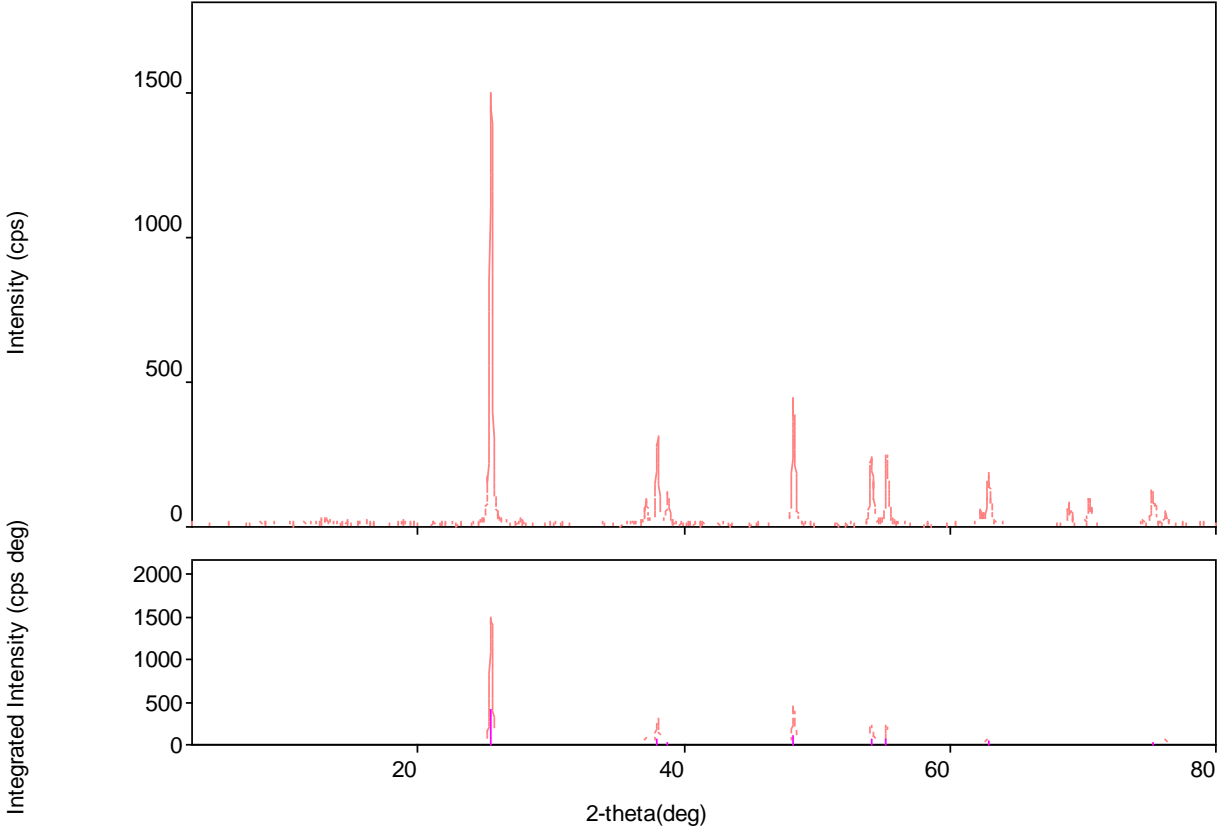
The certificate shall not be reproduced except in full without the written approval of the laboratory.

The above analysis is based on the sample submitted by the customer.


 SYAHIDAH ALWI
 LAB ANALYST
 MATERIAL DEPARTMENT
 CENTRAL LABORATORY

Appendix C XRD Results

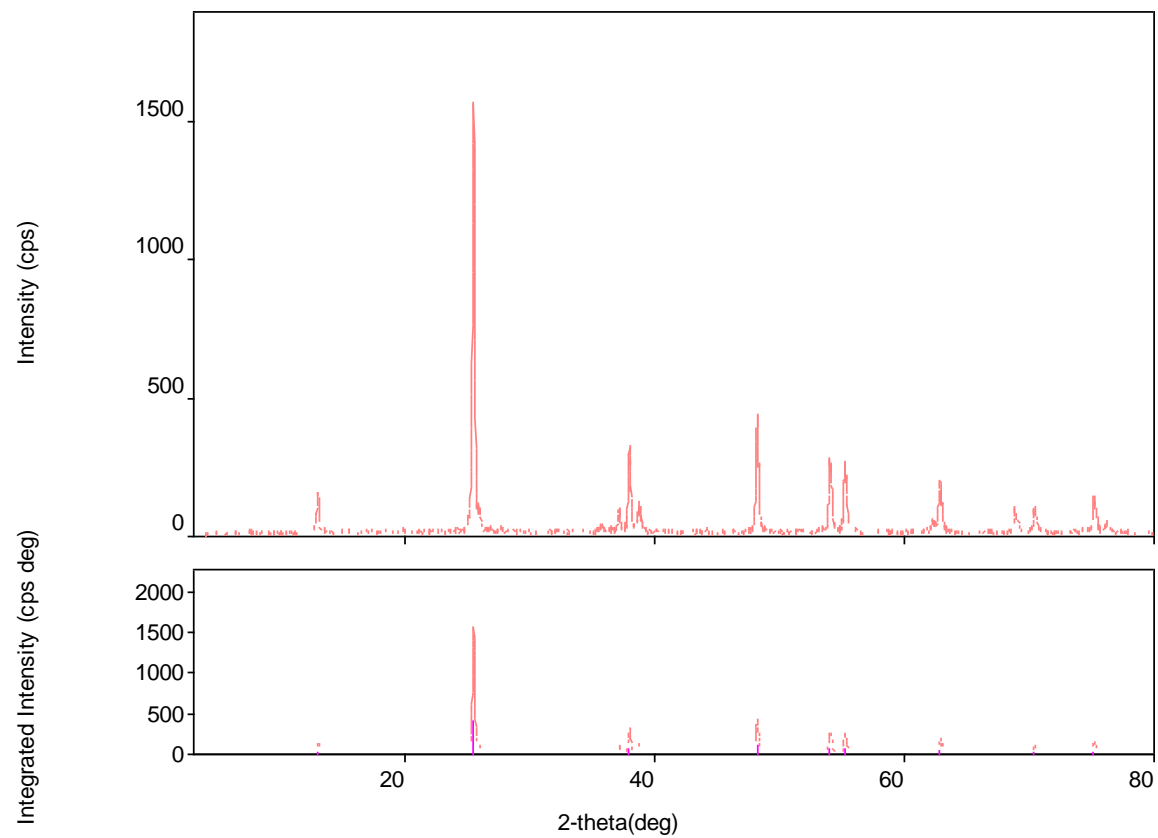
1) 2wt% Cu/TiO₂



Peak list

2-theta (deg)	d (ang.)	Height (cps)	Int. I(cps×deg)	FWHM(deg)	Size	Phase name
12.80(6)	6.91(3)	9(3)	6.6(6)	0.59(7)	140(16)	Unknown,
25.490(5)	3.4915(6)	1079(33)	290(2)	0.208(3)	410(6)	Unknown,
37.14(3)	2.4189(16)	60(8)	15.9(7)	0.20(3)	448(58)	Unknown,
37.955(10)	2.3687(6)	226(15)	59.6(11)	0.206(7)	426(15)	Unknown,
38.762(14)	2.3212(8)	85(9)	20.9(7)	0.16(2)	556(78)	Unknown,
48.214(7)	1.8859(2)	351(19)	87.9(11)	0.184(7)	494(19)	Unknown,
54.049(10)	1.6953(3)	200(14)	58.0(10)	0.206(12)	451(26)	Unknown,
55.230(9)	1.6618(2)	211(15)	52.9(11)	0.185(10)	505(28)	Unknown,
62.93(2)	1.4756(4)	137(12)	44(2)	0.24(2)	406(36)	Unknown,
68.931(15)	1.3611(3)	65(8)	19.3(7)	0.205(18)	490(42)	Unknown,
70.469(12)	1.3352(2)	82(9)	20.2(6)	0.174(12)	583(40)	Unknown,
75.217(11)	1.26221(16)	114(11)	31.6(8)	0.197(11)	533(31)	Unknown,
76.21(3)	1.2483(3)	26(5)	7.4(6)	0.23(3)	449(55)	Unknown,

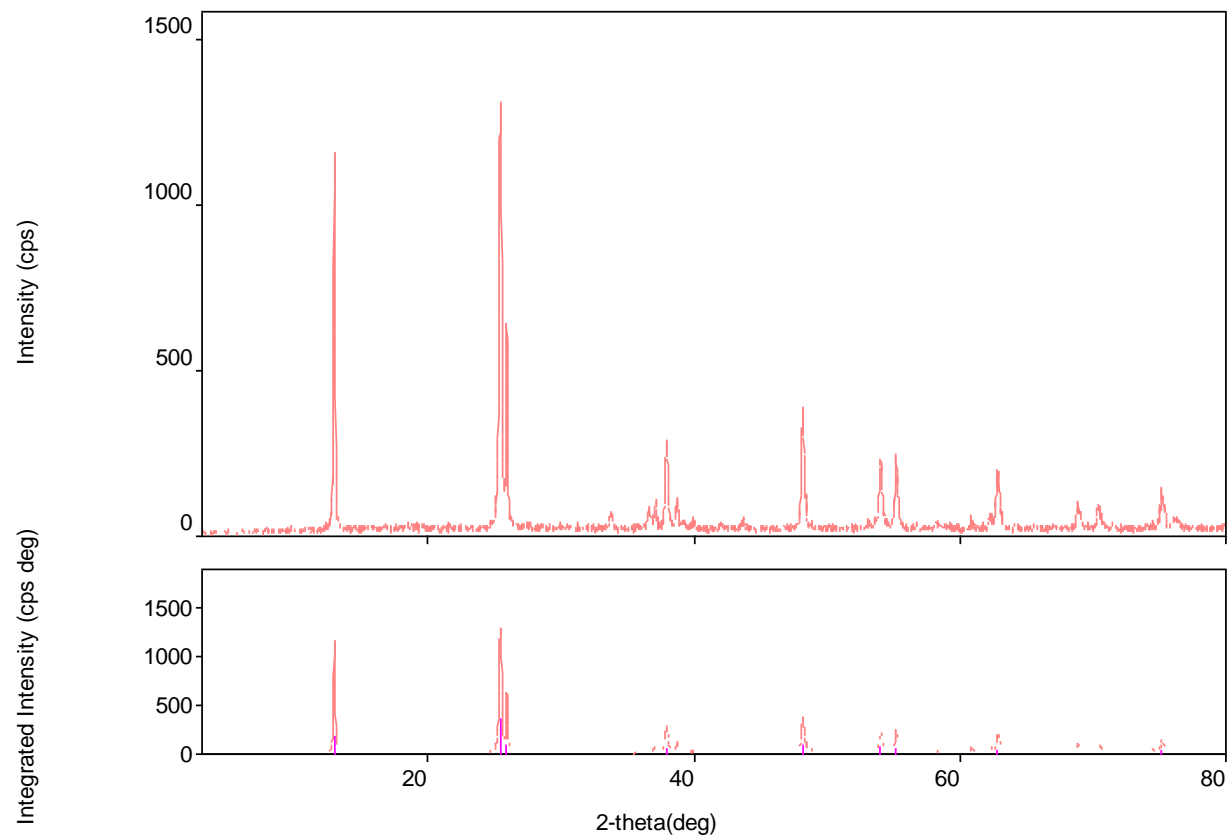
2) 5wt% Cu/TiO₂



Peak list

2-theta (deg)	d (ang.)	Height (cps)	Int. I(cps¥deg)	FWHM(deg)	Size	Phase name
12.968(7)	6.821(4)	96(10)	27.8(8)	0.199(11)	419(24)	Unknown,
25.441(8)	3.4982(11)	1089(33)	290(4)	0.197(7)	431(15)	Unknown,
37.070(16)	2.4231(10)	72(8)	13.5(8)	0.13(2)	678(118)	Unknown,
37.913(11)	2.3712(7)	221(15)	57.5(11)	0.203(9)	431(18)	Unknown,
38.66(2)	2.3270(14)	65(8)	20.6(10)	0.26(2)	342(30)	Unknown,
48.168(8)	1.8876(3)	344(19)	86.6(14)	0.183(9)	496(24)	Unknown,
54.011(10)	1.6964(3)	218(15)	58.3(13)	0.188(13)	496(34)	Unknown,
55.186(8)	1.6630(2)	211(15)	53.1(10)	0.189(10)	495(26)	Unknown,
62.226(18)	1.4907(4)	35(6)	8.5(8)	0.17(3)	576(98)	Unknown,
62.800(10)	1.4784(2)	170(13)	45.4(12)	0.185(12)	525(33)	Unknown,
68.852(17)	1.3625(3)	68(8)	20.7(8)	0.23(2)	445(40)	Unknown,
70.398(16)	1.3363(3)	83(9)	21.6(9)	0.197(17)	516(45)	Unknown,
75.160(12)	1.26302(17)	117(11)	35.6(9)	0.209(14)	501(33)	Unknown,
76.18(3)	1.2486(4)	29(5)	7.6(7)	0.20(3)	535(82)	Unknown,

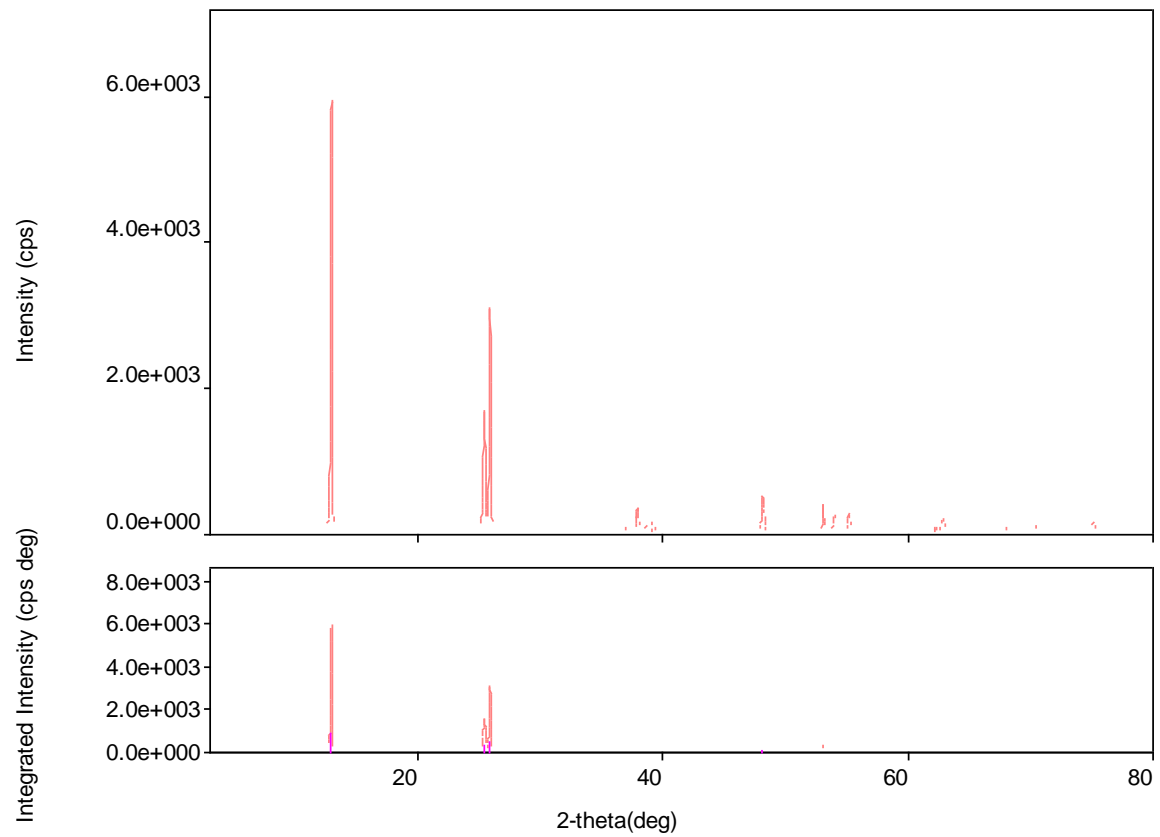
3) 10wt% Cu/TiO₂



Peak list

2-theta (deg)	d (ang.)	Height (cps)	Int. I(cps×deg)	FWHM(deg)	Size	Phase name
12.954(5)	6.828(2)	820(29)	129.6(18)	0.112(4)	745(28)	Unknown,
25.445(5)	3.4976(7)	926(30)	246(3)	0.201(4)	423(9)	Unknown,
25.897(4)	3.4375(6)	491(22)	70.1(16)	0.107(5)	797(39)	Unknown,
33.74(12)	2.654(9)	11(3)	7.5(15)	0.59(10)	147(26)	Unknown,
36.51(2)	2.4590(16)	36(6)	12.1(10)	0.28(3)	312(39)	Unknown,
37.049(14)	2.4245(9)	67(8)	11.6(8)	0.140(16)	624(72)	Unknown,
37.942(12)	2.3695(7)	186(14)	50.3(11)	0.210(12)	418(24)	Unknown,
38.67(3)	2.3262(18)	57(8)	15.4(10)	0.20(3)	450(78)	Unknown,
48.162(10)	1.8878(4)	286(17)	73.2(13)	0.198(9)	460(20)	Unknown,
54.011(13)	1.6964(4)	167(13)	55.4(12)	0.220(18)	423(34)	Unknown,
55.180(9)	1.6632(3)	186(14)	46.3(11)	0.184(11)	510(31)	Unknown,
62.24(3)	1.4903(7)	32(6)	7.9(9)	0.22(4)	446(83)	Unknown,
62.812(18)	1.4782(4)	124(11)	38.9(16)	0.274(16)	355(21)	Unknown,
68.81(3)	1.3632(5)	49(7)	15.0(11)	0.28(3)	365(35)	Unknown,
70.39(2)	1.3365(4)	61(8)	17.5(10)	0.23(2)	445(48)	Unknown,
75.162(15)	1.2630(2)	98(10)	33.1(11)	0.229(19)	457(38)	Unknown,
76.12(3)	1.2494(4)	28(5)	9.6(8)	0.24(4)	448(78)	Unknown,

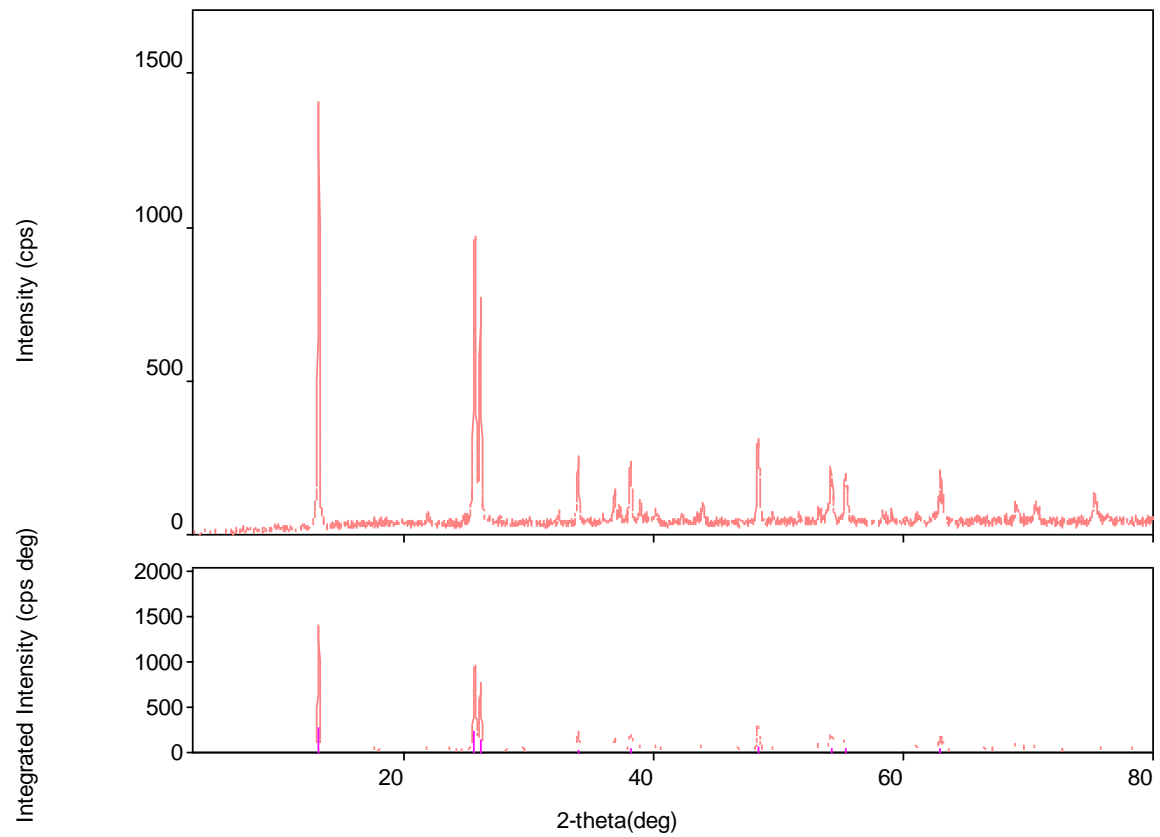
4) 15wt% Cu/TiO₂



Peak list

2-theta (deg)	d (ang.)	Height (cps)	Int. I(cps×deg)	FWHM(deg)	Size	Phase name
12.909(5)	6.852(2)	4352(66)	627(10)	0.110(3)	758(23)	Unknown,
25.373(4)	3.5074(6)	1168(34)	280(3)	0.183(3)	464(9)	Unknown,
25.856(3)	3.4429(4)	2457(50)	365(3)	0.114(2)	750(15)	Unknown,
33.60(3)	2.665(2)	43(7)	10.2(9)	0.20(3)	437(58)	Unknown,
37.06(7)	2.424(5)	33(6)	20(2)	0.54(6)	163(19)	Unknown,
37.882(17)	2.3730(10)	245(16)	55(2)	0.179(16)	491(44)	Unknown,
38.591(14)	2.3311(8)	75(9)	14.0(9)	0.170(14)	516(43)	Unknown,
39.154(7)	2.2989(4)	173(13)	20.9(9)	0.109(7)	805(52)	Unknown,
48.122(6)	1.8893(2)	374(19)	84.5(14)	0.174(7)	521(21)	Unknown,
53.034(3)	1.72530(11)	360(19)	45.6(10)	0.095(3)	975(33)	Unknown,
53.561(16)	1.7096(5)	41(6)	7.3(9)	0.13(2)	698(117)	Unknown,
53.959(8)	1.6979(2)	219(15)	54.9(13)	0.188(9)	494(24)	Unknown,
55.124(8)	1.6647(2)	223(15)	52.2(11)	0.175(9)	534(28)	Unknown,
62.112(16)	1.4932(3)	37(6)	11.0(19)	0.19(5)	500(126)	Unknown,
62.759(12)	1.4793(3)	173(13)	48(2)	0.177(14)	550(45)	Unknown,
67.841(8)	1.38033(14)	123(11)	16.7(8)	0.107(7)	933(60)	Unknown,
68.809(17)	1.3633(3)	68(8)	17.6(10)	0.210(19)	479(45)	Unknown,
70.350(14)	1.3371(2)	81(9)	19.2(9)	0.176(14)	578(47)	Unknown,
75.108(10)	1.26378(15)	120(11)	29.4(10)	0.194(12)	540(33)	Unknown,
76.28(4)	1.2472(5)	13(4)	13.2(13)	0.8(3)	133(47)	Unknown,

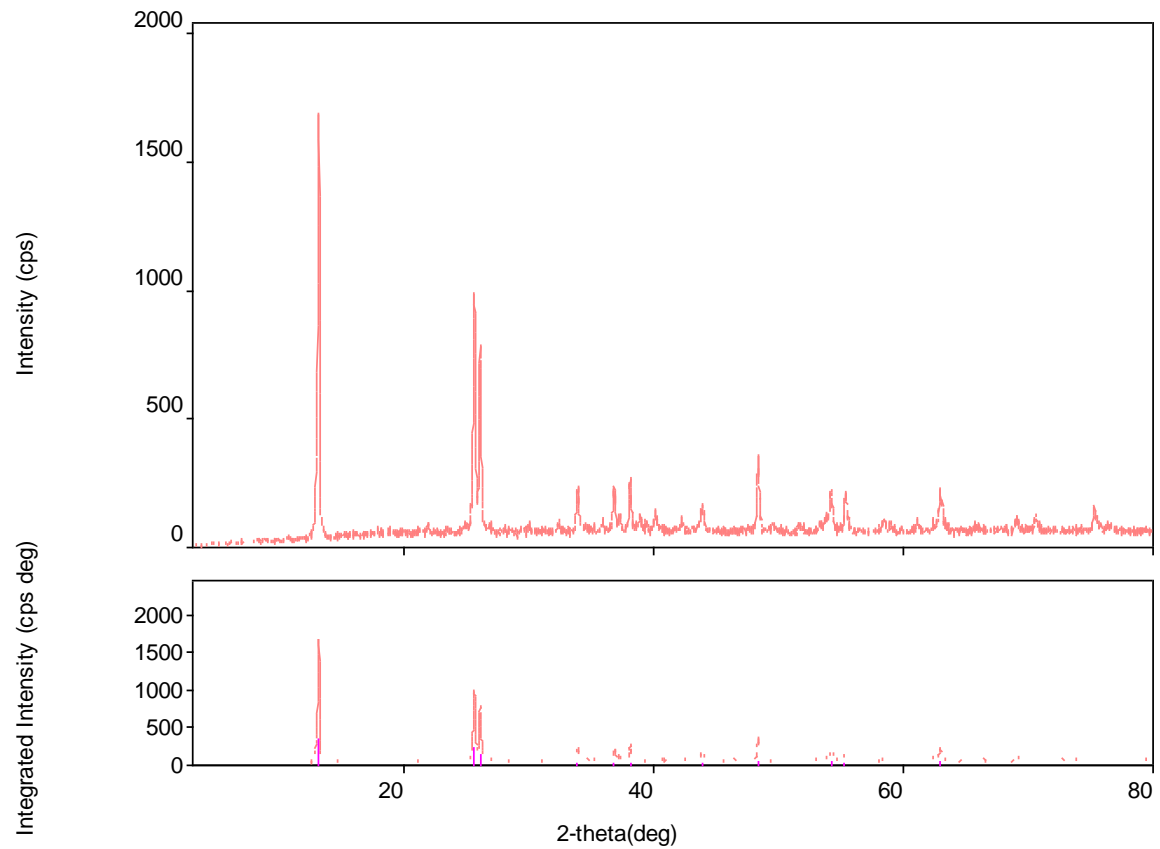
5) 20wt% Cu/TiO₂



Peak list

2-theta (deg)	d (ang.)	Height (cps)	Int. I(cps×deg)	FWHM(deg)	Size	Phase name
13.102(4)	6.752(2)	982(31)	189(2)	0.147(3)	568(13)	Unknown,
25.603(6)	3.4764(8)	666(26)	173(2)	0.199(5)	427(10)	Unknown,
26.068(5)	3.4154(7)	532(23)	104(2)	0.150(6)	566(21)	Unknown,
33.913(10)	2.6412(8)	151(12)	26.1(11)	0.144(11)	600(45)	Unknown,
36.854(13)	2.4369(8)	71(8)	15.0(9)	0.198(14)	443(32)	Unknown,
37.24(4)	2.413(3)	32(6)	8.2(7)	0.24(4)	363(57)	Unknown,
38.093(14)	2.3604(8)	152(12)	35.0(11)	0.188(11)	468(27)	Unknown,
38.84(2)	2.3165(13)	58(8)	12.1(10)	0.13(4)	663(175)	Unknown,
43.92(5)	2.060(2)	37(6)	14.0(15)	0.27(7)	334(83)	Unknown,
48.315(8)	1.8822(3)	232(15)	51.8(12)	0.173(9)	526(28)	Unknown,
53.16(6)	1.7216(19)	36(6)	5.3(10)	0.12(4)	771(241)	Unknown,
54.171(11)	1.6917(3)	138(12)	43.7(14)	0.203(19)	458(42)	Unknown,
55.316(10)	1.6594(3)	148(12)	33.5(11)	0.166(12)	563(41)	Unknown,
61.01(4)	1.5174(9)	16(4)	4.3(9)	0.17(7)	564(233)	Unknown,
62.968(15)	1.4749(3)	130(11)	42.4(14)	0.21(2)	468(48)	Unknown,
69.01(4)	1.3597(6)	43(7)	13.8(13)	0.26(4)	391(67)	Unknown,
70.54(3)	1.3340(6)	46(7)	14.6(13)	0.26(4)	397(64)	Unknown,
75.0(2)	1.265(3)	14(4)	13.9(18)	0.82(13)	127(21)	Unknown,

6) 25wt% Cu/TiO₂

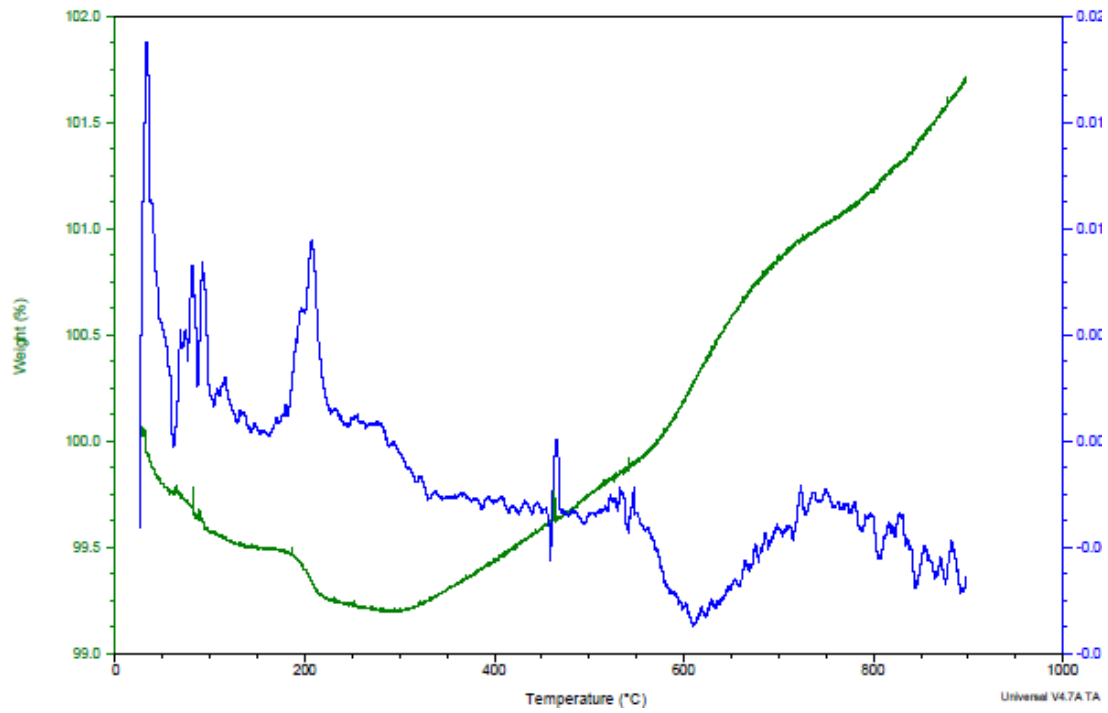


Peak list

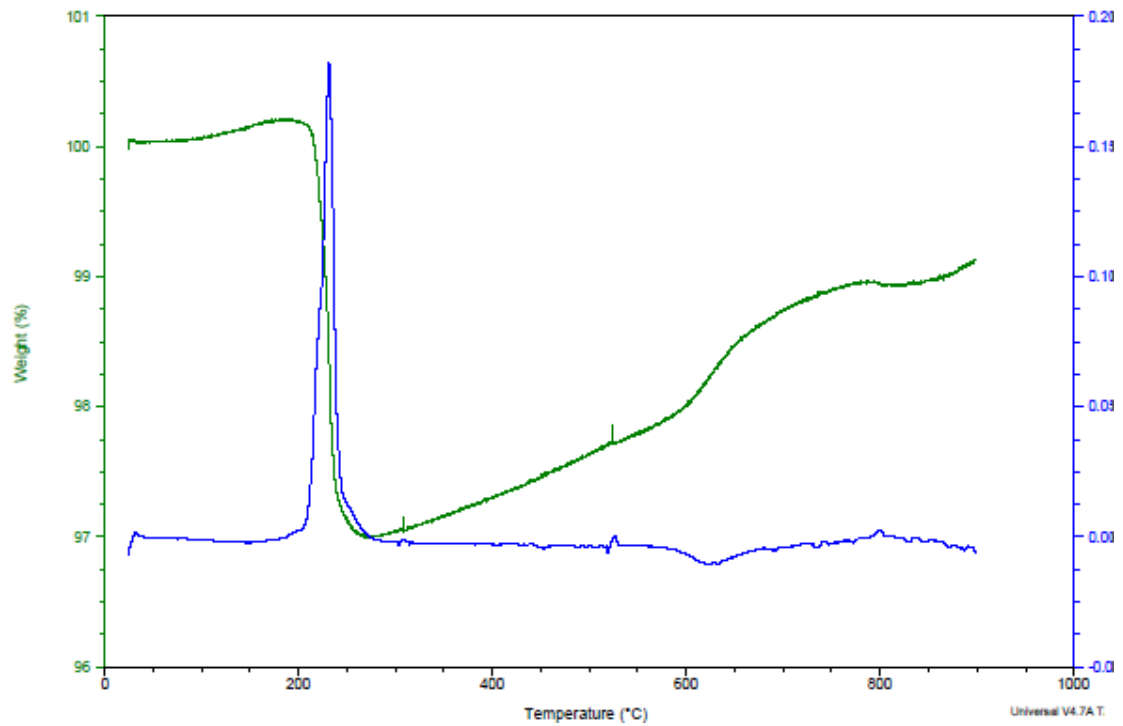
2-theta (deg)	d (ang.)	Height (cps)	Int. I(cps*deg)	FWHM(deg)	Size	Phase name
13.133(6)	6.736(3)	1096(33)	243(3)	0.172(5)	485(13)	Unknown,
25.585(6)	3.4788(8)	630(25)	167(2)	0.206(5)	414(9)	Unknown,
26.046(6)	3.4182(7)	514(23)	111.6(19)	0.168(5)	507(17)	Unknown,
33.834(17)	2.6471(13)	118(11)	29.4(12)	0.209(14)	415(28)	Unknown,
36.73(2)	2.4446(14)	117(11)	26(3)	0.195(18)	449(42)	Unknown,
37.27(3)	2.411(2)	36(6)	8(2)	0.20(6)	447(137)	Unknown,
38.074(11)	2.3616(7)	150(12)	29.0(12)	0.152(13)	579(50)	Unknown,
38.79(6)	2.319(3)	42(7)	9(2)	0.15(9)	587(338)	Unknown,
43.88(2)	2.0618(10)	69(8)	26.0(17)	0.26(4)	339(48)	Unknown,
48.316(12)	1.8822(4)	207(14)	48.6(15)	0.194(11)	470(27)	Unknown,
54.21(2)	1.6907(7)	108(10)	54(2)	0.32(4)	295(36)	Unknown,
55.289(14)	1.6601(4)	120(11)	32.2(13)	0.208(16)	450(35)	Unknown,
58.31(5)	1.5811(11)	31(6)	13.4(14)	0.29(8)	324(89)	Unknown,
61.10(4)	1.5154(8)	29(5)	6.5(12)	0.19(5)	504(127)	Unknown,
62.94(2)	1.4755(4)	101(10)	44.1(19)	0.32(2)	304(23)	Unknown,
68.99(4)	1.3602(7)	33(6)	9.3(13)	0.23(5)	447(99)	Unknown,
70.54(3)	1.3340(4)	53(7)	12.3(13)	0.17(3)	595(94)	Unknown,
75.253(19)	1.2617(3)	73(9)	22.1(13)	0.21(2)	504(58)	Unknown,

Appendix D Thermogravimetric Analysis

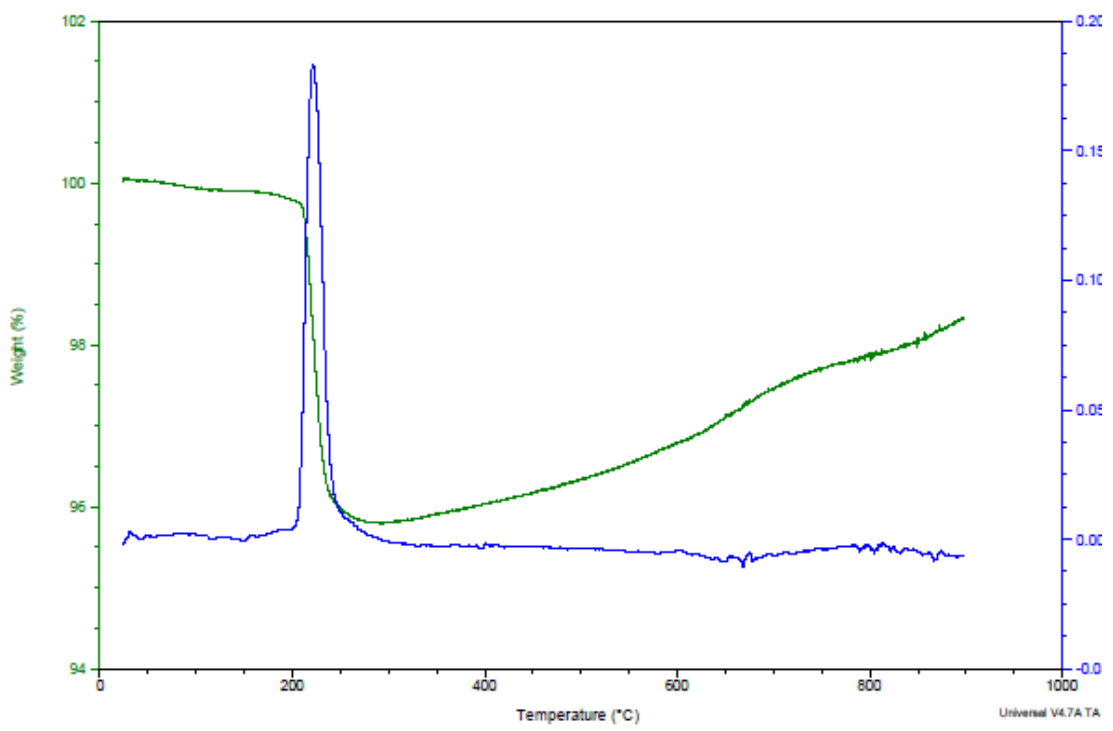
1. 2wt% Cu/TiO₂



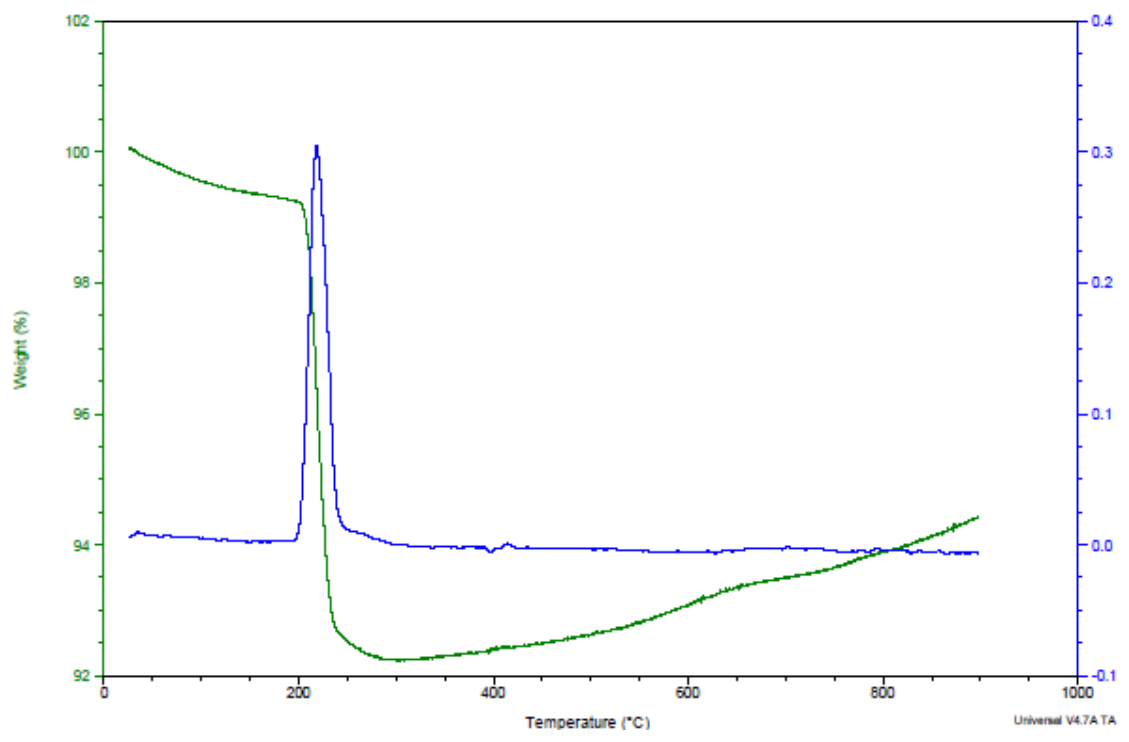
2. 5wt% Cu/TiO₂



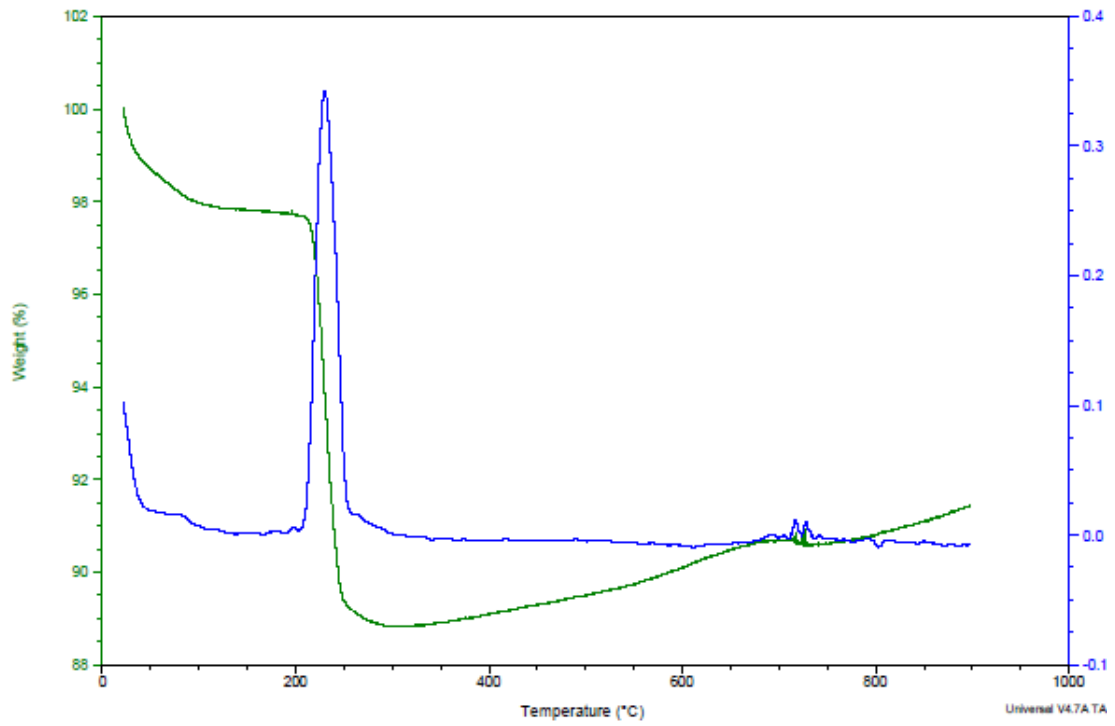
3. 10wt% Cu/TiO₂



4. 15wt% Cu/TiO₂



5. 20wt% Cu/TiO₂



6. 25wt% Cu/TiO₂

